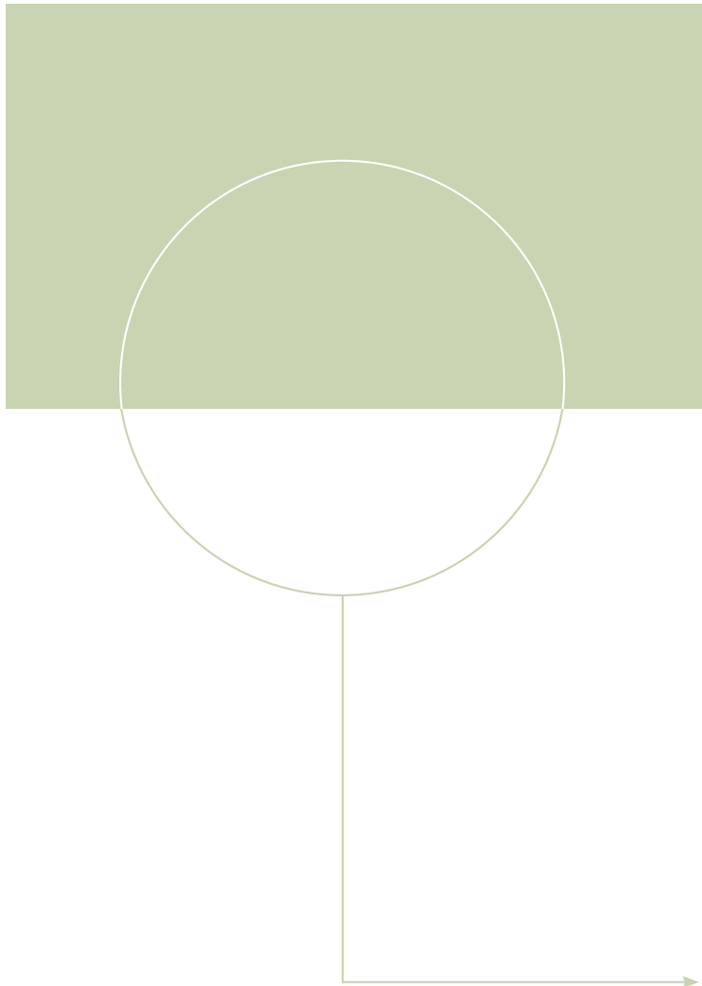

Master's thesis

2020

Hooman Rostami

**NTNU**
Norwegian University of
Science and Technology
Faculty of Engineering
Department of Civil and Environmental Engineering

Hooman Rostami

# Finite Element Limit Analysis of Bearing Capacity Problem

## Application of Optum

June 2020

NTNU
Norwegian University of
Science and Technology

NTNU
Norwegian University of
Science and Technology

NTNU
Norwegian University of
Science and Technology

# Finite Element Limit Analysis of Bearing Capacity Problem

Application of Optum

Hooman Rostami

Geotechnics and Geohazards
Submission date: June 2020
Supervisor: Arnfinn Emdal

Norwegian University of Science and Technology
Department of Civil and Environmental Engineering

# Preface

This thesis is written as a one-semester Master's thesis in the course TBA4900 as part of the MSc degree in *"Geotechnics and Geohazards"* at Norwegian University of Science and Technology (NTNU). This work was carried out in the Spring of 2020.

The topic was proposed by Arnfinn Emdal and Steinar Nordal at the Civil and Environmental Engineering group at NTNU. This work is focused more on the bearing capacity problem, especially the shallow foundation.

Arnfinn Emdal was the main supervisor throughout this research work. I would like to help the Geotechnical department of NTNU for the help, guidance, and feedback throughout this work.

Trondheim, June 2020

Hooman Rostami

# Abstract

Foundations are designed to take loads from the superstructure and convey it to the soil underneath. The foundation system has to be designed with a certain safety factor, so the foundation can withstand the applied load(s) without failure in the ground. Various solutions for the bearing capacity problem have been developed using statics. The main goal of these methods is to find the maximum magnitude of external loads that soil mass can take without failure. This type of analysis is called limit equilibrium methods and is comprised of two bounds, upper bound which tries to reach the exact solution from above and the other one is called lower bound which tries to reach the answer from below.

Using limit analysis solutions and statics, solutions have been developed for solving problems in geotechnical engineering. These solutions are used in standard geotechnical engineering practice. The solution for undrained analysis and weightless soil for a shallow, strip footing without embedment, is derived and it is well known to be the exact solution. When it comes to the effect of weight of soil, the effect of footing shape and embedment on the bearing capacity, the hand-derived formulas assume *a priori* statements in solving the problems, and then derive a solution which is not necessarily correct.

A new type of numerical analysis, namely numerical limit analysis has been developed, which uses finite element discretization to approximate the problem and solve it to obtain the upper and lower limit to the exerted load(s). In this work, this tool will be used to run simulations to check the validity of the current methods, and develop factors and expressions for the effect of soil weight, as well as developing depth, inclination, and shape factors.

This thesis is proposing a new expression for bearing capacity factor $N_\gamma$ under inclined loading. This new expression is compared to some of the experimental works by some other researchers. Furthermore, it proposes a new shape factor, depth factor, and strength anisotropy factor for bearing capacity of undrained soils. Moreover, a macro model is proposed for a special case of a shallow foundation with suction beneath the footing.

# Contents

# List of Tables

# List of Figures

Chapter 1

# Introduction

## 1.1 Background

Foundations are structures that the superstructure is designed to rest on. A foundation has to be designed to withstand the loading of the superstructure and it has to settle in an acceptable range, so the superstructure can maintain its serviceability. These two limit designs are usually called ultimate limit state and serviceability limit state, respectively. The first limit state will ensure that failure of foundation will be avoided, with a certain safety factor, and the second limit ensures that a tolerable settlement will occur.

The first set of problems can be called *stability problem* and the second one can be called *elasticity problem*. These two sets of problems are treated differently and somewhat unrelated. *Stability problems* includes problems such as earth pressure, slope stability, and bearing capacity.

Various solutions for these types of problems have been developed using statics and assuming a predetermined failure surface and assuming soil mass to be in the state of failure. This type of analysis is called limit equilibrium method. The main goal of this method is to find the maximum magnitude of external loads that a body of material can take without the ground beneath the footing going to failure.

The plasticity theorem lays the foundation to find bounds of exact collapse load without constructing an incremental load-deformation analysis. For this purpose, there are two types of analyses, namely lower bound analysis, or static approach, and upper bound analysis, or dynamic approach. Lower bound limit analysis tries to approach the “real answer” from below, by increasing the admissible load and the upper bound limit analysis is trying to approach it from above by decreasing the admissible load. If these two answers converge, the real answer will be obtained.

There are solutions developed by plasticity theorem for effect of cohesion and surcharge on bearing capacity. There are no rigorous lower and upper bound solutions available for effect of soil density, shape and inclination factor. This thesis is trying to address these issues.

## 1.2 Motivation

Bearing capacity equation is partly developed by using limit state solutions and statics. Using the superposition method, bearing capacity is assumed to be the sum of three components affecting it, namely cohesion, overburden and weight component, which are a function of friction angle and foundation base roughness.

The solution for undrained analysis and weightless drained soil for a shallow, strip footing without embedment has a rigorous solution. This is not the case for effect of weight of soil, effect of footing shape and embedment on the bearing capacity. Hand-derived formulas assume *a priori* statements in solving the problems, where the failure mode and failure line is assumed beforehand and the mathematical foundations builds upon a set of assumptions. This means that the derived solutions are not necessarily exact.

A new type of numerical analysis, namely numerical limit analysis has been developed (Lyamin and Sloan [2002a], Lyamin and Sloan [2002b] and Krabbenhøft and Damkilde [2003]) which uses finite element discretization to approximate the problem and solve it to obtain the upper and lower limit to the exerted load(s). These methods find an upper and lower limit to an external load without running the whole load-deformation curve. This type of analysis gives the chance to develop rigorous lower/upper bound solutions for some of the problems which are hard to derive in closed form solutions.

In this thesis, the main motivation is to use this finite element limit analysis tool to derive rigorous solutions for the effect of soil weight, shape and inclination factors.

## 1.3 Objectives

1. Presenting the current methods for calculating bearing capacity of shallow foundations.
2. Running simulations to check the validity and precision of the program.
3. Constructing a bearing factor for effect of soil weight
4. Running simulations to construct shape, depth and inclination factors for undrained analysis
5. Running simulations to construct shape and inclination factors for drained analysis
6. Comparison of the results with current methods

7. Comparison of the results with experimental data

## 1.4 Limitations

In this work, associated flow rule is assumed for a considerable part of the work. Every classical solution (Terzaghi et al. [1996], Meyerhof [1951], Janbu [1976], and many others) assume associated flow for solving bearing capacity, even though it is not mentioned explicitly. In addition, footings have been assumed to be rough throughout this thesis.

## 1.5 Approach

Throughout this thesis, it has been a goal to compartmentalize each of the contributing factors in bearing capacity in a way that they would not affect each other and would not contribute at the same time. This was done, for instance, by not giving any weight or cohesion to the soil when the surcharge effect was being investigated. It can then be assured that each contributing factor is depicted correctly in bearing capacity equations.

## 1.6 Structure of the thesis

The main body of this thesis is structured as follows:

- **Chapter 1** - Introduction
  - In this chapter, a background to the general scheme of work is presented. Motivation, objective, and limitation of the work have also been presented.
- **Chapter 2** - Bearing Capacity in Classical Soil Mechanics
  - In this chapter, a literature study of available methods for calculating bearing capacity of a shallow foundation will be given.
- **Chapter 3** - Bearing Capacity in Ponderable Soils
  - In this chapter, a literature study of available equations available for calculating bearing capacity factor, $N_\gamma$ will be given.
- **Chapter 4** - Methods
  - Here, an introduction to the theoretical foundation of limit analysis, FELA and the program used in this thesis will be given.
- **Chapter 5** - Numerical Limit Analysis in Tresca soil are presented.

- Here, 8 cases of analysis which were run on Tresca soil are presented.

- **Chapter 6** - Numerical Limit Analysis in MC Soil
  - Here, 5 cases of analysis which were run on Mohr-Coulomb soil.
- **Chapter 7** - Comparison of Numerical and Experimental Results
  - Here, some experimental results are compared to the proposed equation for $N_\gamma$.
- **Chapter 8** - Summary and Discussion
  - Here, a summary and discussion of the results will be presented. Some recommendations for further work is given as well.

There are four attachments to this thesis, which are the following:

- **Appendix A** - Acronyms
  - In this appendix, a list of acronyms are summarized.
- **Appendix B** - Introduction to OptumG2
  - In this appendix, an introduction to OptumG2 will be given.
- **Appendix C** Matlab Codes
  - In this appendix, the Matlab codes used to run Optum via Matlab API are given.
- **Appendix D** Results
  - A series of Excel worksheets with the results of simulations are given.

Chapter 2

# Bearing Capacity in Classical Soil Mechanics

## 2.1 Introduction

One of the important tasks of a geotechnical engineer is designing foundations that a superstructure can stand on. This foundation has to be designed to withstand the loading of the superstructure and it has to give serviceability. This means that the design of the foundation has to avoid failure of foundation with a certain safety factor and it should result in a tolerable settlement. Finding the maximum load which causes failure in soil mass is the goal of the first type of analysis.

Studying a simple case of a footing with a centric vertical load on a homogeneous soil, Vesić [1973] stated that the failure of a foundation is a shear failure of the soil which the foundation rests on. The work categorized three principal modes of failure which happens under a shallow foundation, which are:

- general shear failure
- local shear failure
- punching shear failure

According to Vesić [1973], the general shear failure has a well-defined failure line from edges of the footing down to the soil mass and up to the surface with a spiral (see Figure 2.1a). "Curve 1" shows the load-displacement curve of the soil as loads increases to an ultimate load. This mode of failure shows a clear collapse point. Ultimate bearing capacity of a foundation is the maximum load the ground under a foundation can sustain without failing.

Local shear failure is a failure pattern similar to general shear failure except failure zones just beneath the foundation are developed (see 2.1b).

The punching failure shows a reaction which does not cause movement of soil on the sides of foundation. Failure involves both compression and failure of soil mass beneath the foundation (see Figure 2.1c).

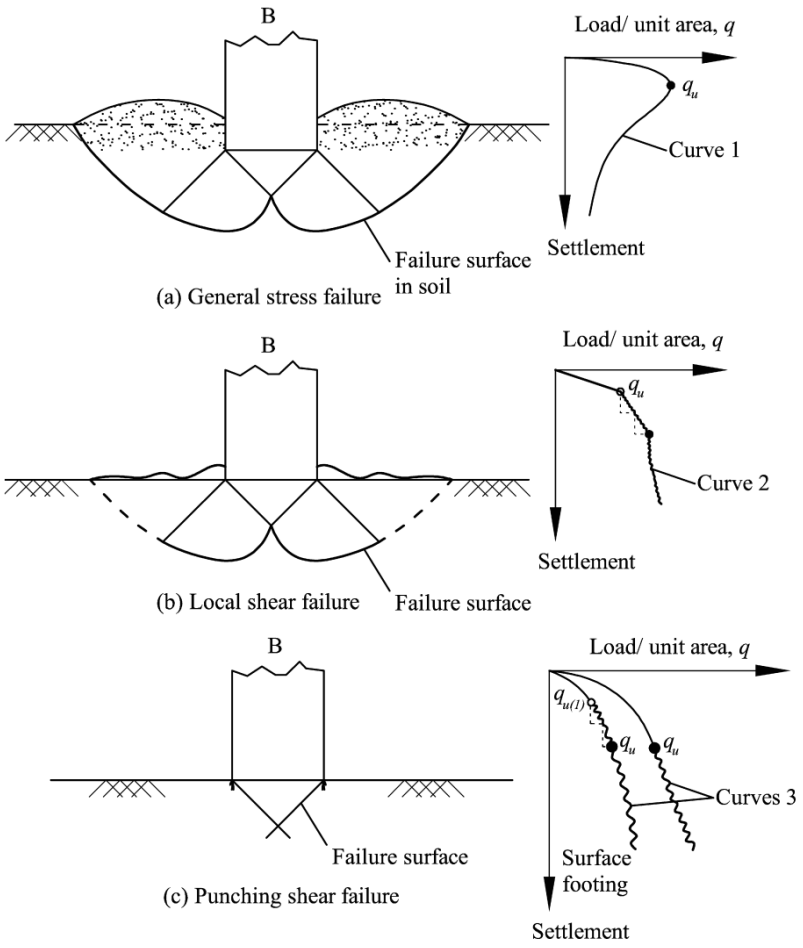


Figure 2.1: Principal modes of bearing capacity failure (from Rao [2010])

The failure point, generally, is defined as a point where the load-displacement curve first reaches a steady, maximum value (Vesić [1973]). This can be seen for general stress failure where there is a clear maximum point. For the other failure modes, the failure point can be defined as the point where the deformations are unacceptable ($q_u$ in the figure).

## 2.2 Bearing capacity theories

There have been several works published which have tried to solve the problem of bearing capacity. Laboratory experiments that have tried to find the ultimate bearing capacity suffer from the shortcoming of difficulty of selecting a representative friction angle for comparison between laboratory experiments and theoretical models (especially for friction angles greater than 30°). Discussions associated with selecting a representative friction angles will come later. In this chapter, a couple of these will be mentioned and their assumption and the results will be shown.

### 2.2.1 Plasticity bearing capacity theory by Prandtl and Reissner

Classical plasticity theory assumes that a bearing capacity problem is comprised of rigid-plastic soil which shows no deformation before failure and a plastic flow with constant stress after failure point (Prandtl [1921]). This theory predicts the general stress failure (failure mode a in Figure 2.1). Prandtl [1921] develops the theory for a rectangular foundation with width B and length L resting, with an overburden of D (see Figure 2.2a), on a soil which is perfectly plastic with the Mohr-Coulomb failure criterion (see Figure 2.2b). The method tries to find the maximum allowed vertical stress (see Figure 2.2c).

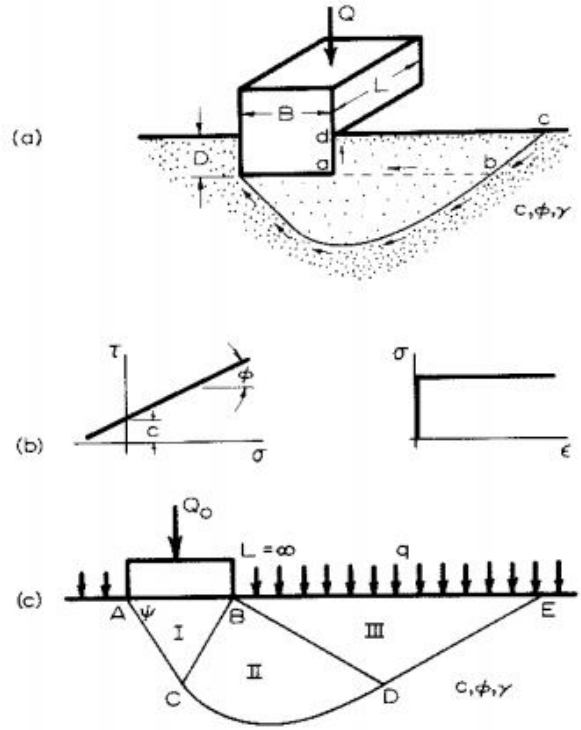


Figure 2.2: Bearing capacity failure and relevant zones (from Prandtl [1921])

Prandtl [1921] made the following simplifications to the solve the bearing capacity problem:

- Effect of failure line which goes through overburden is neglected (along bc in Figure 2.2a).
- Shear resistance along the soil and foundation is neglected (shear resistance along ad in Figure 2.2a)
- Shear resistance between the overburden and the soil beneath the foundation (along ab in Figure 2.2a) is neglected.
- The length of the foundation, L, is assumed to be large in comparison to the width of foundation, B, or B/L<0.2 in more mathematical terms. For B/L>0.2 and different shapes, some factors have to be introduced.

Prandtl [1921] and Reissner [1924] then solves the problem seen in Figure 2.2c by theory of plasticity. He categorized the failure zones into three failure zones (see 2.2c). Zone I is commonly known as active Rankine zone, zone II as radial Prandtl zone and Zone III as passive Rankine zone. The active Rankine zone pushes the radial Prandtl zone sideways and that zone pushes the passive Rankine zone upward. The AC line is inclined at $45° + {}^{\varphi}/_{2}$ and the DE line is inclined at $45° - {}^{\varphi}/_{2}$ . The shape of the zone II depends on the friction angle, $\varphi$ and the following ratio: $\frac{\gamma B}{q}$. For $\frac{\gamma B}{q} = 0$ (weightless soil) the curve becomes a logarithmic spiral. The curve becomes circular for total stress soil model where $\varphi = 0°$. Prandtl [1921] and Reissner [1924] formulate the bearing capacity for a weightless soil as follows:

$$q_{ult} = c \cdot N_c + q \cdot N_q \tag{2.1}$$

Where $N_c$ and $N_q$ are dimensionless bearing capacity factors. They are defined as:

$$\begin{aligned} N_q &= \tan^2(\frac{\pi}{2} + \frac{\varphi}{2}) \cdot e^{\pi \cdot \tan\varphi} \\ N_c &= (N_q - 1) \cdot cot\varphi \end{aligned} \tag{2.2}$$

Figure 2.3 shows the variation of these two factors with change of friction angle, $\varphi$.

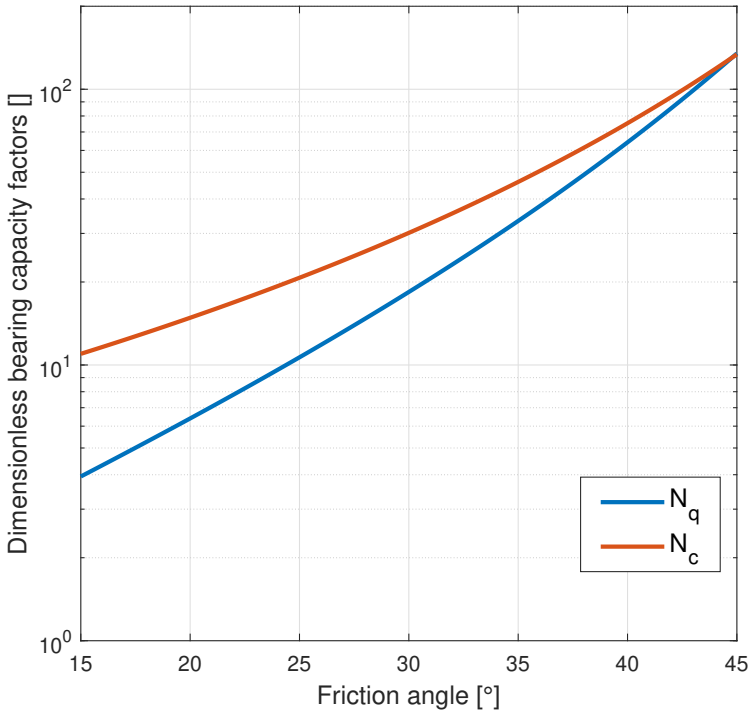


Figure 2.3: Variation of dimensionless bearing capacity factor, $N_c$ and $N_q$ with friction angle

The solution proposed by Prandtl [1921] and later by Reissner [1924] is based on the slip-line method where the basic differential equation of the slip-line network is applied to the problem (Manoharan and Dasgupta [1995]).

### 2.2.2 Terzaghi's bearing capacity theory

Terzaghi used the superposition method to solve the bearing capacity problem for a rigid, strip footing on a homogeneous soil. The main idea of this method is to find the contribution of each of the parameters which can affect the bearing capacity (cohesion, overburden and soil weight, and friction angle) by expressing them in form of dimensionless bearing capacity factors, namely $N_c$, $N_q$, and $N_\gamma$, with which he used the limit equilibrium method to calculate them. Davis and Booker [1971] have investigated the theoretical justification of the superposition method suggested by Terzaghi and their work concludes that even though this method is not rigorous, it leads to a conservative design, i.e. a design on the safe side.

The proposed failure mechanism by Terzaghi is shown in Figure 2.4. It is based on the limit equilibrium method where a critical surface is found from different shapes.

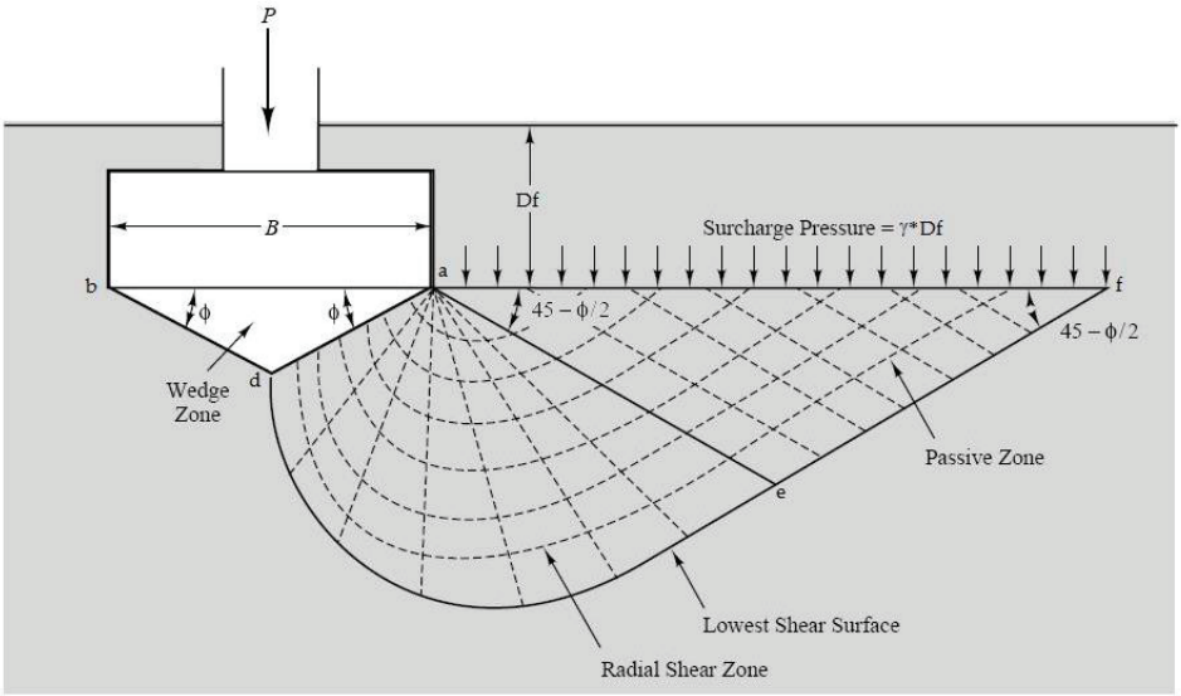


Figure 2.4: Geometry used in Terzaghi method (from Coduto [2001]).

Terzaghi's solution divides the problem into three zones:

- Wedge zone (abd): This an elastic zone beneath the foundation, inclination of lines bc and ad is equal to the friction angle, $\varphi$.
- Lower Shear Surface (ade): this is the same as Prandtl radial shear zone.
- Passive zone (aef): this is the passive Rankine zone where the slip lines comes out of the soils surface with $45° + \frac{\varphi}{2}$

These geometrical shapes are chosen on physical grounds (Hjiaj et al. [2005]) and the equilib-

rium is enforced at the global level and the stress distribution outside the failure surface is not considered.

The ultimate bearing capacity can be obtained by finding the passive force required to cause failure along line bdef (see Figure 2.4). The ultimate bearing capacity is a function of overburden pressure, p'=$\gamma \cdot D$, cohesion, c, unit weight of soil, $\gamma$, and friction angle, $\varphi$.The complete derivation of the formulas can be found in Coduto [2001] and Terzaghi et al. [1996]. Terzaghi gives the following equation for ultimate bearing capacity:

$$q_{ult} = N_c \cdot c + N_q \cdot p' + \frac{1}{2} \cdot N_\gamma \cdot \gamma \cdot B \tag{2.3}$$

Where the $N_q$, $N_c$ and $N_\gamma$ are defined as:

$$\begin{aligned} N_q &= \frac{e^{2\cdot(\frac{3\pi}{4}-\frac{\varphi}{2})\cdot\tan\varphi}}{2\cdot cos^2(45+\frac{\varphi}{2})} \\ N_c &= (N_q - 1)\cdot cot\varphi \\ N_\gamma &= \frac{1}{2}\cdot K_{p\gamma}\tan^2\varphi - \frac{\tan\varphi}{2} \end{aligned} \tag{2.4}$$

Terzaghi never gave the formula used to calculate $K_{p\gamma}$; hence the only way to calculate $N_\gamma$ is by using the figures. In addition, Kumbhojkar [1993] tried to repeat Terzaghi's work and he got similar results for friction angles upwards to 39 ° but not for friction angles larger than that. Figure 2.5 shows how values of dimensionless bearing capacity factors change depending on friction angle.

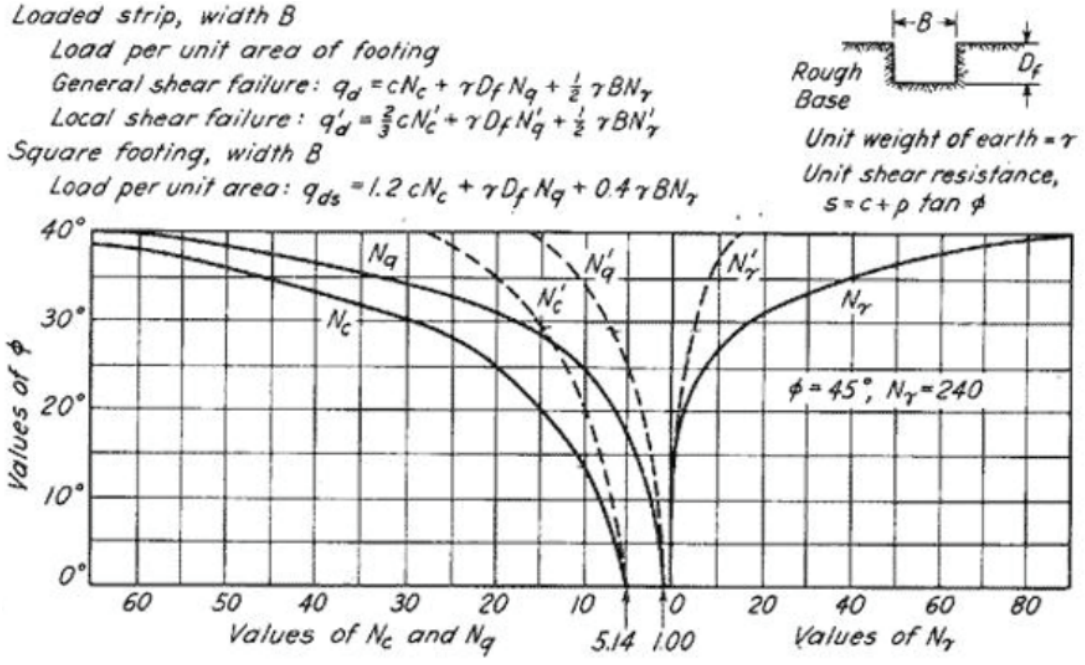


Figure 2.5: Values of dimensionless bearing capacity factors with varying friction angles, $\varphi$ (from Terzaghi et al. [1996]).

It should be noted that Terzaghi et al. [1996] suggested factors and constants for other forms of foundations apart from the strip foundation. Equation 2.5 is the bearing capacity for a foundation with a square form and Equation 2.6 shows it for a foundation with a circular form. For these two forms, B is the width of the square and the diameter of the circle, subsequently.

$$q_{ult} = 1.3 \cdot N_c \cdot c + N_q p' + 0.4 \cdot N_\gamma \cdot \gamma \cdot B \tag{2.5}$$

$$q_{ult} = 1.3 \cdot N_c \cdot c + N_q p' + 0.3 \cdot N_\gamma \cdot \gamma \cdot B \tag{2.6}$$

As can be seen, for non-strip footings, the cohesion term increases by 30%, while the overburden component does not change, but the weight component decreases by 20% for square form and by 40% for circular footing.

### 2.2.3 Meyerhof's bearing capacity theory

By using the limit equilibrium method, Meyerhof [1951] developed a solution for shallow and deep foundations with rough soil-solid interfaces. Figure 2.6 shows the failure surface assumed by Meyerhof [1951].

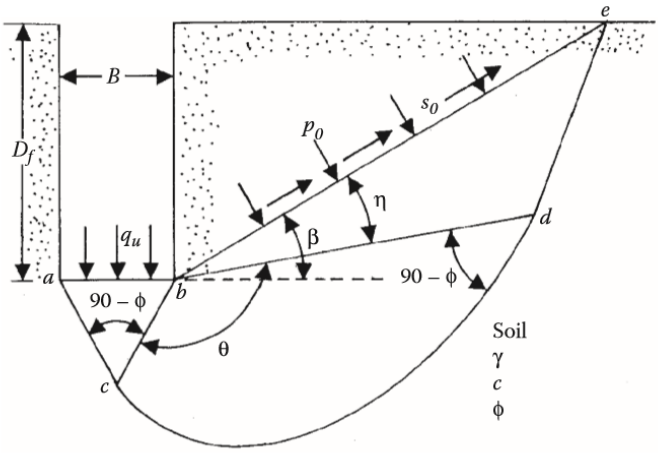


Figure 2.6: Plastic zones for a rough shallow strip foundation in Meyehof's bearing capacity theory (from Das [2017]).

The triangular wedge abc acts elastically, zone bcd is logsprial shear zone, and triangle bde is a mixed shear zone. Unlike Terzaghi and Prandtl, Meyerhof's free surface has both normal stress and shear stresses, marked as $p_0$ and $s_0$ in Figure 2.6. By using the superposition method, the ultimate bearing capacity is defined the same as Terzaghi et al. [1996] method has suggested (see Equation 2.3). Derived formulas for dimensionless bearing capacity factors are different from the previous two papers. These factors now also depend on the foundations roughness. $N_\gamma$ is derived by trial and error, but the other factors are found analytically. Derivation of the

formulas can be found in Das [2017], but the formulas are as follows:

$$\begin{aligned} N_q &= \frac{(1+sin\varphi)\cdot e^{\,2\theta\tan\varphi}}{1-sin\varphi\cdot sin(2\eta+\varphi)} \\ N_c &= (N_q-1)\cdot cot\varphi \\ N_\gamma &= \frac{4\cdot P_p\cdot sin(45+\frac{\varphi}{2})}{\gamma\cdot B^2}-\frac{1}{2}\tan(45+\frac{\varphi}{2}) \end{aligned} \tag{2.7}$$

where $\theta$ and $\eta$ are a function of degree of mobilization of shear strength, m, and the angle between the exit point of the failure line (point e in the Figure 2.6) and the horizontal line. For no mobilization of shear stress, m=0, we have:

$$\eta = 45^\circ - \frac{\varphi}{2} \quad and \quad \theta = 90^\circ + \beta$$

and for a full mobilization of shear stress, m=1, we have:

$$\eta = 0 \quad and \quad \theta = 135^\circ + \beta - \frac{\varphi}{2}$$

By varying these two parameters, dimensionless factors are shown in Figure 2.7.

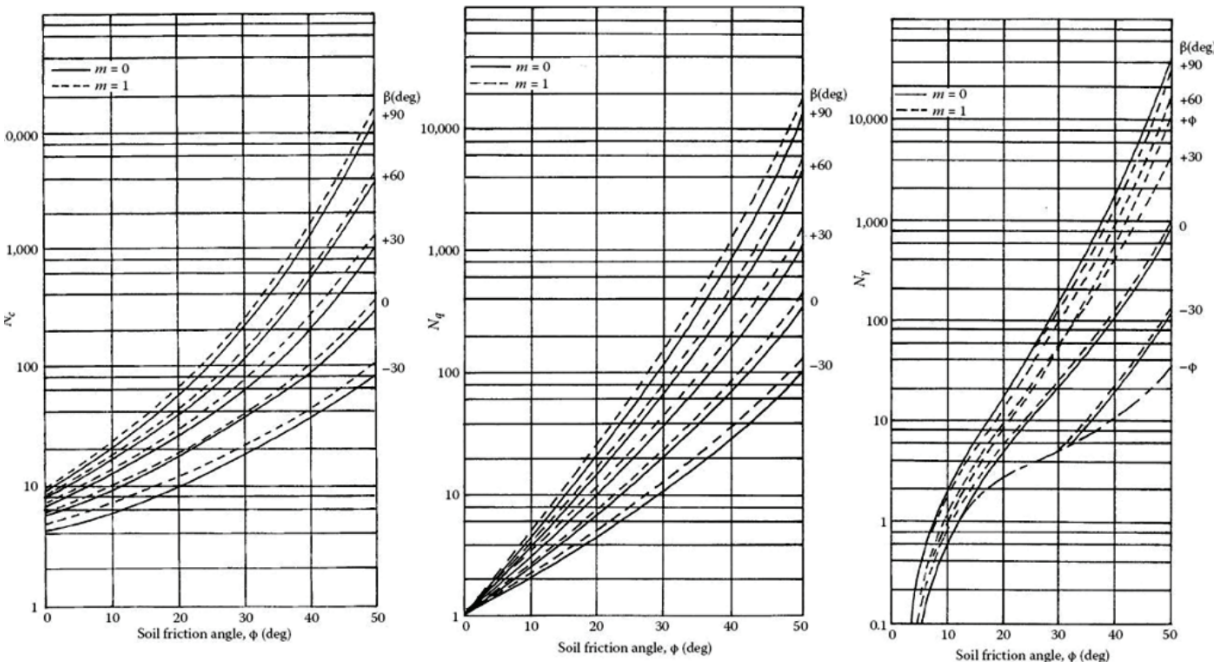


Figure 2.7: Meyerhofs bearing capacity factors (from Meyerhof [1951])

For the special case of no overburden, the equations will be simplified to the following:

$$\begin{aligned} N_q &= \frac{1+sin\varphi}{1-sin\varphi}e^{\,\pi\cdot\tan\varphi} \\ N_c &= (N_q-1)\cdot cot\varphi \\ N_\gamma &= (N_q-1)\cdot\tan(1.4\cdot\varphi) \end{aligned} \tag{2.8}$$

Equations for $N_q$ and $N_c$ are similar to the one developed by Terzaghi et al. [1996] and Prandtl [1921].

Meyerhof [1963] finds the partly theoretical and partly semi-empirical solution for the circular and rectangular foundations. The dimensionless bearing capacity factor for the strip, circular, and rectangular are drawn in Figure 2.8.

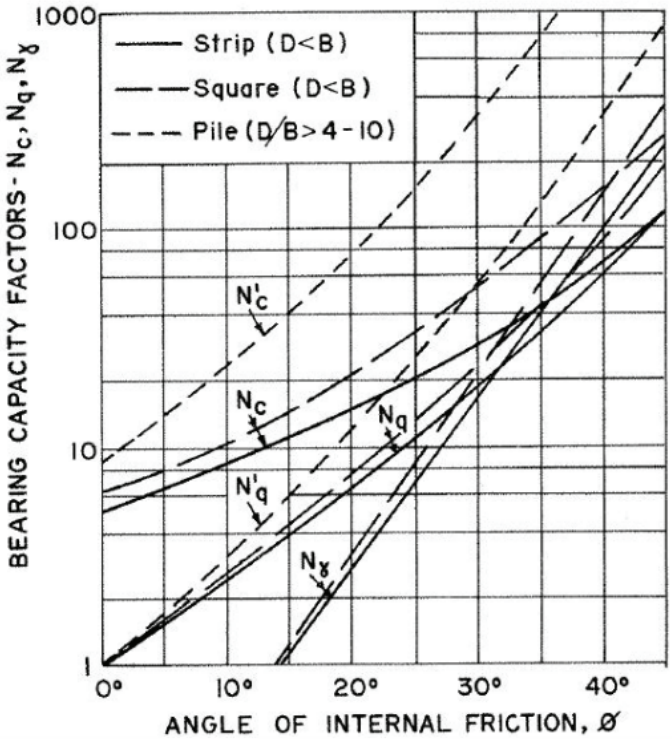


Figure 2.8: Dimensionless bearing capacity factors for strip, square and pile foundation (from Meyerhof [1963])

Alternatively, we can expand the ultimate bearing capacity formula to:

$$q_{ult} = s_c \cdot N_c \cdot c + s_q \cdot N_q \cdot p' + \frac{1}{2} \cdot s_\gamma \cdot N_\gamma \cdot \gamma \cdot B \tag{2.9}$$

where shape factor, $s_q$, $s_c$ and $s_\gamma$ are defined as follows:

$$s_c = 1 + 0.2 \cdot \tan^2(\frac{\pi}{2} + \frac{\varphi}{2}) \cdot \frac{B}{L} \tag{2.10}$$

$$\begin{aligned} s_q = s_\gamma &= 1 && when\ \varphi = 0° \\ s_q = s_\gamma &= 1 + 0.1 \cdot \tan^2(\frac{\pi}{2} + \frac{\phi}{2}) \cdot \frac{B}{L} && when\ \varphi \geq 10° \end{aligned} \tag{2.11}$$

Meyerhof [1963] states that for friction angles higher than 30°, laboratory experiments show smaller $N_\gamma$ for strip foundations in comparison to circular and square foundations. The opposite

is true for bearing capacity theory where strip foundations always have a higher value than circular and square foundations in cohesionless soil. Meyerhof [1963] states that the effect of intermediate principal stress leads to this discrepancy and he suggests using the triaxial test to obtain strength parameters for circular and square footings and a plane strain compression test to obtain the parameters for strip footings. He proposes the following formula to find the friction angle which should be used in the calculation of finding bearing capacity:

$$\varphi = (1.1 - 0.1 \cdot \frac{B}{L}) \cdot \varphi_t \tag{2.12}$$

where $\varphi$ is the friction angle suggested to use and $\varphi_t$ is the friction angle interpreted from triaxial tests.

### 2.2.4 Conclusion

In most geotechnical practices concerning bearing capacity problems, and its application on practical engineering problems, the following is generally accepted:

1. The superposition method (see Section 2.2.2), which sums up bearing capacity as a sum of three elements, namely cohesion, overburden and weight of soil (Equation 2.3)
2. The failure surface and its geometry, seen in Figure 2.9, which is a modified version of Terzaghi's model after experimental results
3. The dimensionless bearing capacity factors, $N_q$ and $N_c$, which are derived by Prandtl [1921] and Reissner [1924] and confirmed by Meyerhof [1951].

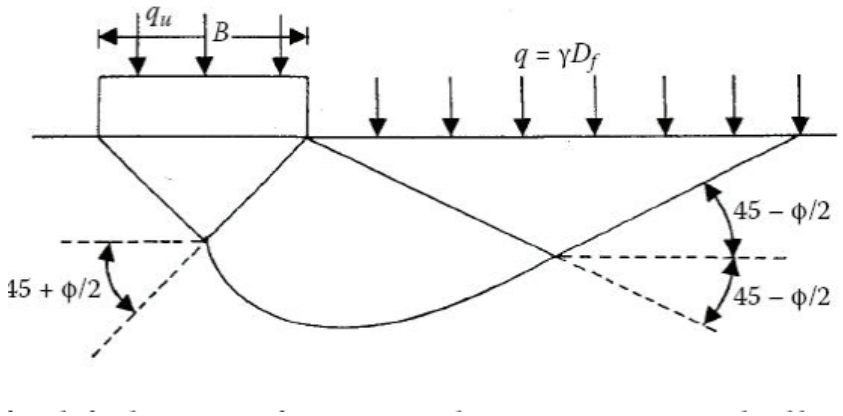


Figure 2.9: Modified Terzaghi's failure surface after laboratory tests (from Das [2017])

The only reason for the lack of one unified theory for ultimate bearing capacity is the lack of a closed-form solution for dimensionless bearing capacity, $N_\gamma$. This is the only variable that causes the difference between the different proposed solutions and formulas available in the literature. Up until now, two theories have been discussed as proposed solutions for $N_\gamma$, which are graphically presented in Figure 2.10. Some of the most well-known proposals for

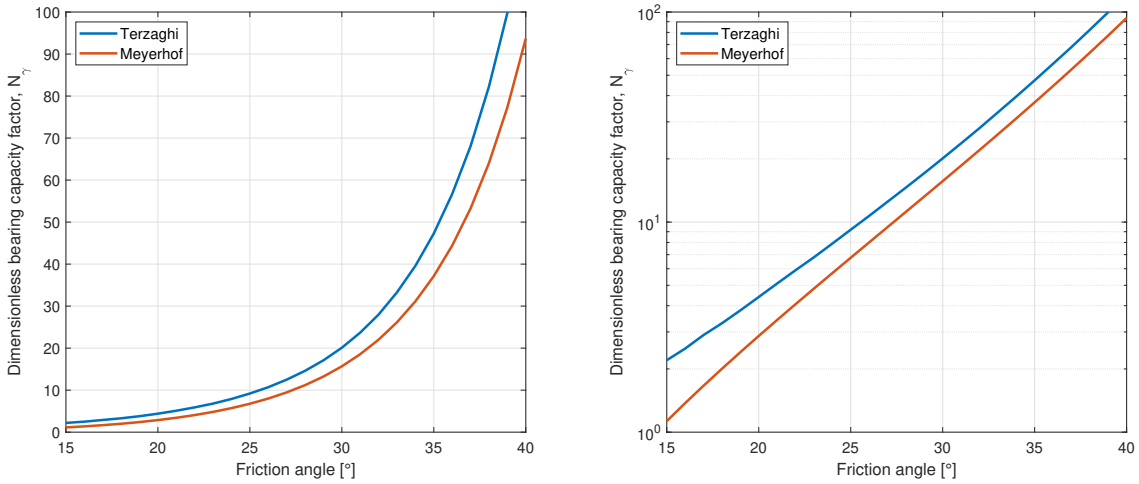


(a) 2D plot

(b) logarithmic plot

Figure 2.10: Graphical Representation of $N_\gamma$ proposed by Terzaghi and Meyerhof

determining $N_\gamma$ will be presented in Chapter 3.

Chapter 3

# Bearing Capacity in Ponderable Soils

In this chapter, the effect of soil density on the bearing capacity, which is expressed by the bearing capacity factor $N_\gamma$, will be explored in the classical soil mechanics. As mentioned in Chapter 2, previous researchers, namely Golder et al. [1941] and Meyerhof [1951], have found an exact solution for the effect of cohesion and overburden on the ultimate bearing capacity. There is a lack of closed-form solutions for the effect of soil density, which has brought about the development of several methods and theories that have attempted to solve this problem. Figure 3.1 shows the range of $N_\gamma$ calculated by different methods for friction angle $\varphi$=30°. The methods are color sorted into 7 categories:

- Limit Equilibrium
- Finite difference/finite element
- Method of characteristics
- Finite element limit analysis
- Ordinary differential equation
- Formulas
- Upper bound solutions
- Exact solution (Martin [2004])

The proposed value for $N_\gamma$ by these different methods ranges from 13 to almost 25, even though the exact solution is around 15. It should be noted that most of these formulas overestimate the factor which means they are on the unsafe side.

Das [2017] states the primary reason for the development of several theories for finding $N_\gamma$ and their inability to correlate with laboratory experiments lies in the difficulty of the selection of friction angle. The friction angle of soil depends on intermediate principal stress and the natural anisotropy of soil means that selection of representative friction angle is not easy (more about this in Chapter 7).

According to Loukidis and Salgado [2009] another reason for various expressions of $N_\gamma$ can be related to the different assumptions of failure, geometry and mechanisms below the footing base (active or rigid wedge).

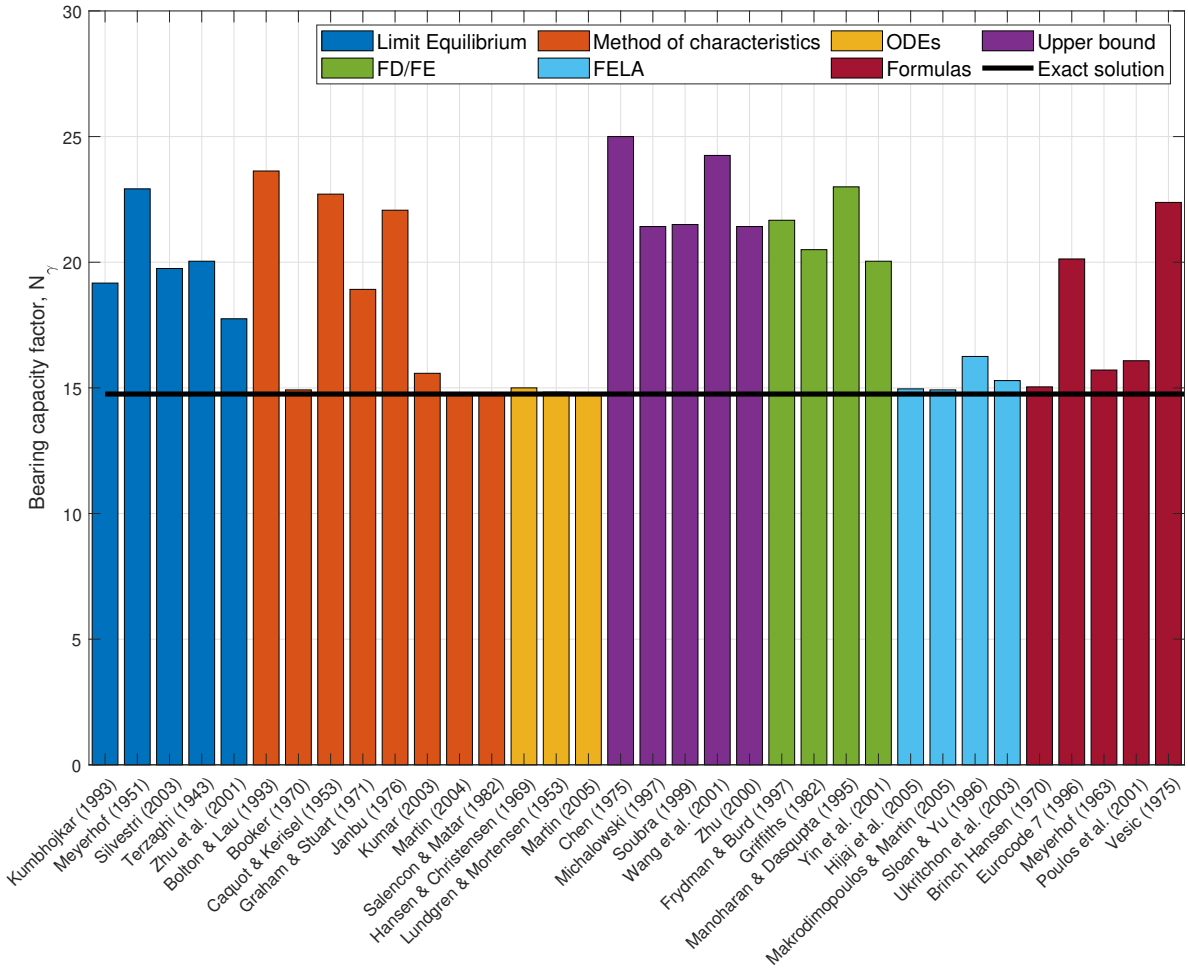


Figure 3.1: $N_\gamma$ for $\varphi$=30° by various authors (redrawn after Martin [2005])

In the following sections, some of the proposed solutions for the bearing capacity factor, $N_\gamma$, will be explored.

## 3.1 Brinch-Hansen's bearing capacity formula

Hansen [1961] proposes a modification to Terzaghi's bearing capacity formula by adding shape factors,$s$, depth factors, $d$, and inclination factors, $i$. The equation then becomes:

$$q_{ult} = s_c \cdot d_c \cdot i_c \cdot N_c \cdot c + s_q \cdot d_q \cdot i_q \cdot N_q \cdot p' + \frac{1}{2} \cdot s_\gamma \cdot d_\gamma \cdot i_\gamma \cdot N_\gamma \cdot \gamma \cdot B \tag{3.1}$$

According to Hansen [1961], $N_\gamma$ is found by Lundgren-Mortensen rupture for vertical loading (see Figure 3.2):

$$N_\gamma = 1.5 \cdot (N_q - 1) \cdot \tan\varphi \tag{3.2}$$

Figure 3.3 shows the dimensionless bearing capacity factors used by Hansen [1970].

Hansen [1961] used the following shape factors, which are based on the experiments done

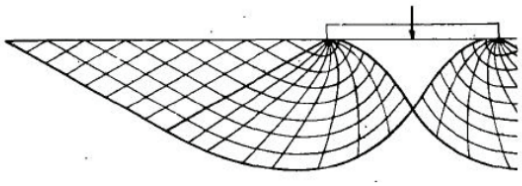

Figure 3.2: Lundgren-Mortensen failure mechanism used for calculation of $N_\gamma$ (from Hansen [1970])

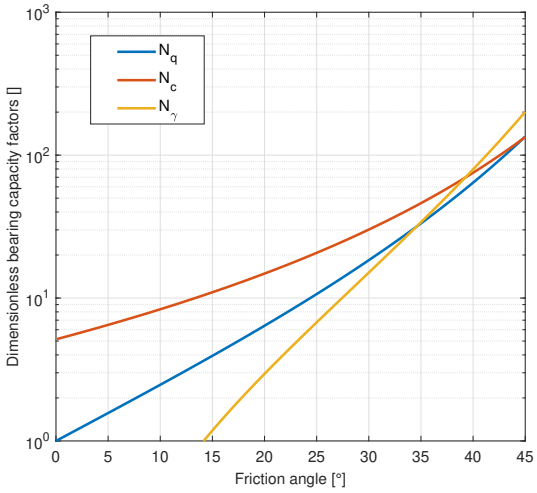


Figure 3.3: Dimensionless bearing capacity factors as a function of friction angle (adapted from Hansen [1970])

by de Beer [1970]:

$$\begin{aligned} s_c &= 1 + \frac{N_q}{N_c} \cdot \frac{B}{L} \\ s_q &= 1 + sin\varphi \cdot \frac{B}{L} \\ s_\gamma &= 1 - 0.4 \cdot \frac{B}{L} \end{aligned} \tag{3.3}$$

Hansen [1961] described the depth factor for a foundation with a embedment of $D_f$ as follow for ${}^{D_f}/_{B} \leq 1$:

$$\begin{aligned} d_c &= d_q - \frac{1 - d_q}{N_q \cdot \tan\varphi} \\ d_q &= 1 + 2 \cdot \tan\varphi \cdot (1 - \sin\varphi)^2 \cdot \frac{D_f}{B} \\ d_\gamma &= 1 \end{aligned} \tag{3.4}$$

and following factors for $^{D_f}/_{B} > 1$:

$$\begin{aligned} d_c &= 1 + 0.4 \cdot \arctan(\frac{D_f}{B}) \\ d_q &= 1 + 2 \cdot \tan\varphi(1 - \sin\varphi)^2 \cdot \arctan(\frac{D_f}{B}) \\ d_\gamma &= 1 \end{aligned} \tag{3.5}$$

## 3.2 Proposed solution by Vesic

By using the theory of plasticity, Vesić [1973] divided the bearing capacity problem into three zones, active Rankine, radial Prandtl zone, and passive Rankine zones. Vesic states that the shape of the failure line is confirmed experimentally by de Beer [1970]. Based on the result of experiments, Vesić [1973] proposes the following formula for calculation of $N_\gamma$:

$$N_\gamma = 2 \cdot (N_q + 1) \cdot \tan\varphi \tag{3.6}$$

According to Das [2017], this proposed solution has error not exceeding 5% for friction angle between 20° and 40° compared to the exact solution. He proposes following shape factors for a rectangular foundation:

$$\begin{aligned} s_c &= 1 + \frac{B}{L} \cdot \frac{N_q}{N_c} \\ s_q &= 1 + \tan\varphi \cdot \frac{B}{L} \\ s_\gamma &= 1 - 0.4 \cdot \frac{B}{L} \end{aligned} \tag{3.7}$$

and the following shape factors are for circular and square-shaped foundations:

$$\begin{aligned} s_c &= 1 + \frac{N_q}{N_c} \\ s_q &= 1 + \tan\varphi \\ s_\gamma &= 0.6 \end{aligned} \tag{3.8}$$

Vesić [1973] uses the same depth factor as Hansen [1961].

## 3.3 Solution proposed by Janbu

This solution was developed by Janbu [1976] and was later further developed to the current version (outlined in Grande et al. [2016]). This method solves the bearing capacity problem for a so-called effective stress analysis (a-$\varphi$ analysis) and a total stress analysis ($S_u$ analysis). Here,

we will look at two cases where loading is centric and inclined on a-$\varphi$ and $S_u$ basis.

### 3.3.1 effective stress analysis

In this method, instead of having inclination factors, a roughness ratio is defined. Roughness ratio for an effective stress analysis is:

$$r = \frac{\tau_h}{\sigma'_v \cdot \tan\varphi} \tag{3.9}$$

Incorporating inclined load into the bearing capacity formulation means that the direction of principal stress is tilted from vertical stress by an angle, called $\omega$, which is defined as:

$$w = \tan^{-1}(f_w \cdot \tan\alpha_{c+}) \tag{3.10}$$

where:

$$f_w = \frac{1}{r}\left(1 - \sqrt{1 - r^2}\right) \tag{3.11}$$

and

$$\tan\alpha_{c+} = \tan\varphi + \sqrt{1 + \tan^2\varphi} \tag{3.12}$$

Opening of the Prandtl zone will become $\pi/2$ - $\omega$. The roughness ratio will affect the active Rankine zone as well. The stress field for this bearing capacity problem is shown in Figure 3.4.

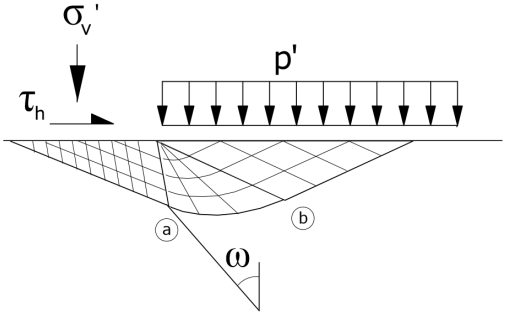


$$\begin{aligned}
\sigma'_{\mathrm{vn}} &= \sigma'_{\mathrm{v}} - p' \\
\sigma'_{\mathrm{vn}} &= (N_q - 1)(p' + a) \\
\tau_h &= r \cdot \tan\rho(\sigma'_{\mathrm{v}} + a) \\
\tan\omega &= f_\omega \tan\alpha_{c+} \\
f_\omega &= \frac{1}{r}\left(1 - \sqrt{1 - r^2}\right) \\
\tan\alpha_{c+} &= \tan\rho + \sqrt{1 + \tan^2\rho} \\
\alpha_{c+} &= \frac{\pi}{4} + \frac{\rho}{2}
\end{aligned}$$

Figure 3.4: Stress field for a centric, inclined load in an effective stress analysis (from Grande et al. [2016])

The general bearing capacity for a weightless soil is defined as:

$$\sigma'_v = N_q \cdot (p' + a) - a \tag{3.13}$$

where the $N_q$ is defined as:

$$N_q = \frac{(1 + f_w^2) \cdot N_+}{1 + f_w^2 \cdot N_+} \cdot e^{(\pi - 2\omega)\cdot\tan\varphi} \tag{3.14}$$

where $N_+$ is defined as:

$$N_+ = \frac{1+\sin\varphi}{1-\sin\varphi} \tag{3.15}$$

This means that $N_q$ is a function of friction angle, $\varphi$ and roughness ratio, r. The diagram of different $N_q$ for different values of roughness and friction angle is shown in Figure 3.5.

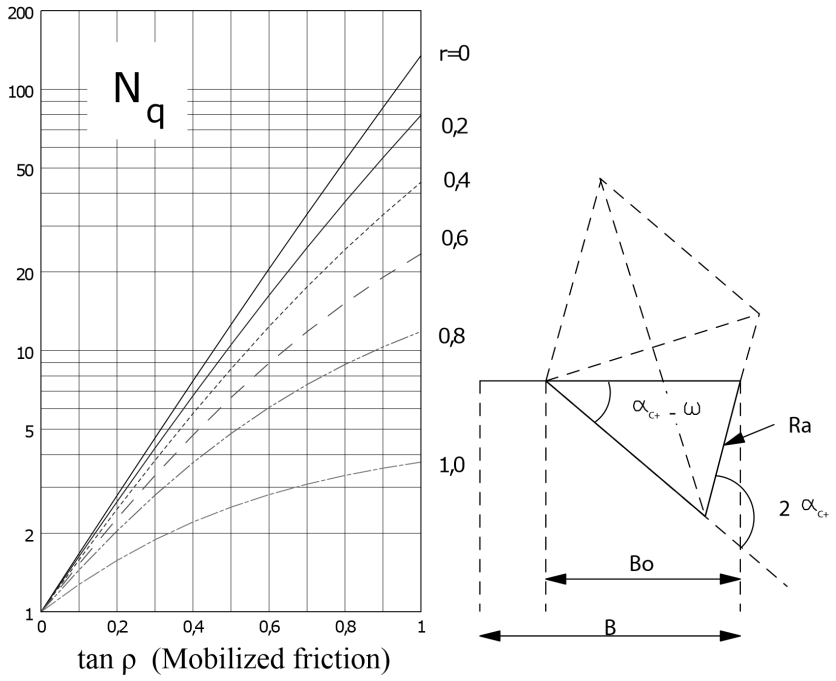


Figure 3.5: Bearing Capacity factor, $N_q$ diagram (from Grande et al. [2016])

For taking into account the weight of the soil, the method of characteristics is used. According to this method, foundation pressure is increasing almost linearly from the outer foundation point with $2\gamma N_\gamma$. For solving the problem, foundation pressure is assumed in a triangular stress distribution (see Figure 3.6).

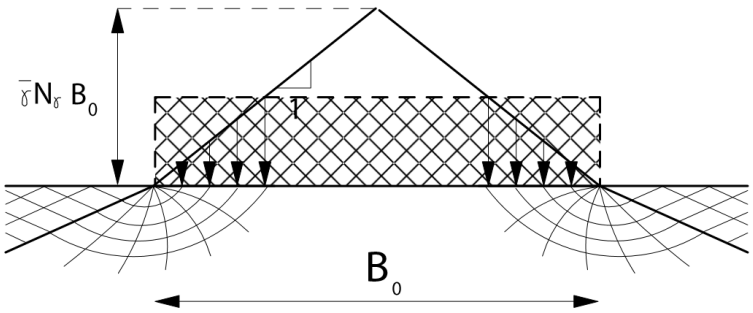


Figure 3.6: Geometry used in the method of characteristics (from Grande et al. [2016])

By defining an equivalent depth, $z_0$ at 80% of maximum depth, a dimensionless foundation width, $B_0$ is calculated which is used for the bearing capacity factor, $N_\gamma$. Figure 3.7 shows how

the reference depth is located in the geometry of the bearing capacity problem.

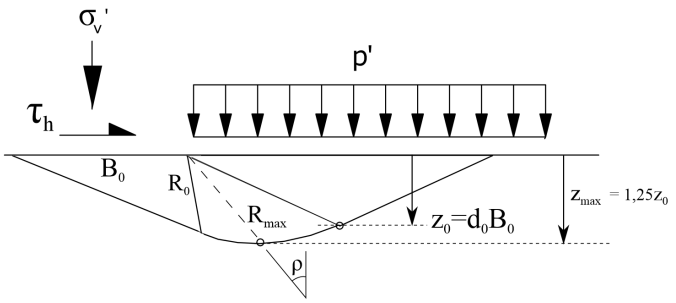


Figure 3.7: Assumption of geometry and reference depth, $z_0$ (from Grande et al. [2016])

Here, reference depth is defined as:

$$d_0 = \sin(\alpha_{c+} - \omega) \cdot e^{(\alpha_{c+} - \omega) \cdot \tan\varphi} \cdot \frac{1}{1.25 \cdot (2 - r)} \tag{3.16}$$

Reference depth, $z_0$ is related to bearing capacity factor, $N_\gamma$ by:

$$d_0 = \frac{1}{2} \cdot \frac{N_\gamma}{(N_q - 1)} \tag{3.17}$$

Hence, the main equation for calculation of bearing capacity becomes:

$$\sigma'_v = (N_q - 1) \cdot (p' + a) + \frac{1}{2} \cdot \gamma \cdot N_\gamma \cdot B_0 \tag{3.18}$$

Figure 3.8 shows values of $N_\gamma$ for different roughness ratio and friction angles. Grande et al. [2016] state that the weight element of bearing capacity reduces by about 30% for non-strip vertical loading. The authors suggest using conservative $N_\gamma$ for non-strip loading. Grande et al. [2016] states that it is not recommended to correct for depth factors in effective stress analysis.

### 3.3.2 Total stress analysis

This is a specific case of the effective stress analysis where friction angle is zero and the cohesion is equal to shear strength, $S_u$. Figure 3.9 shows the stress field for a centric, inclined load on a soil with total stress behavior. Here, the bearing capacity will be defined as:

$$\sigma_v = N_c \cdot S_u + p \tag{3.19}$$

where bearing capacity factor, $N_c$ is defined as:

$$N_c = 1 + \pi - \sin^{-1} r + \sqrt{1 - r^2} \tag{3.20}$$

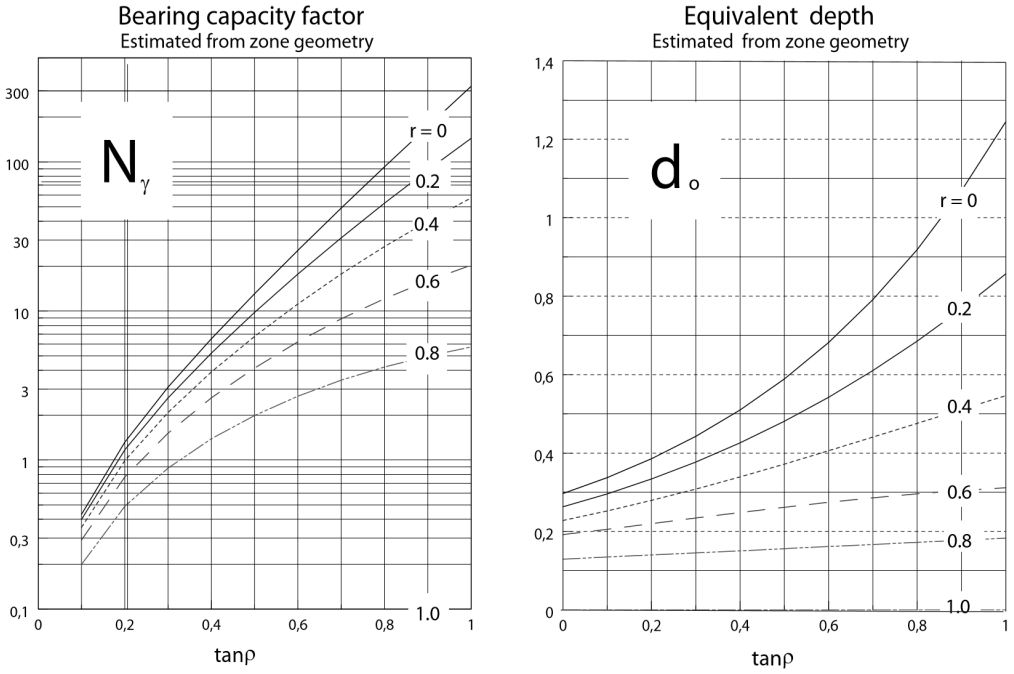


Figure 3.8: Bearing capacity factor, $N_\gamma$, chart for inclined loading ( from Grande et al. [2016])

Roughness ratio, r, now is defined as the ratio of horizontal stress to shear strength:

$$r = \frac{\tau_h}{S_u} \tag{3.21}$$

Grande et al. [2016] state that shape factor for total stress analyses is corrected by following relationship:

$$N_{c,\ quadratic} = (1 + 0.2 \cdot (1 - r)) \cdot N_{c,\ strip} = (1 + f_A) \cdot N_{c,\ strip} \tag{3.22}$$

Grande et al. [2016] state the following depth factor:

$$N_{c,\ D} = (1 + f_D) \cdot N_{c,\ shallow} \tag{3.23}$$

where the correction factor, $f_D$ comes from Figure 3.11.

## 3.4 Michalowski's bearing capacity proposals

By the using tkinematical approach of upper bound limit analysis, Michalowski [1997] found a solution for solving $N_\gamma$. According to Michalowski [1997], apart from weightless soil, the rigid-block mechanism does not follow the exact geometry proposed by Prandtl [1921]. This is since $N_c$ and $N_q$ does not follow the proposed formulas when $\gamma \neq 0$. By correlating the bearing capacity to dimensionless coefficients, namely $\frac{c}{\gamma \cdot B}$ and $\frac{q}{\gamma \cdot B}$, Michalowski [1997] suggested the

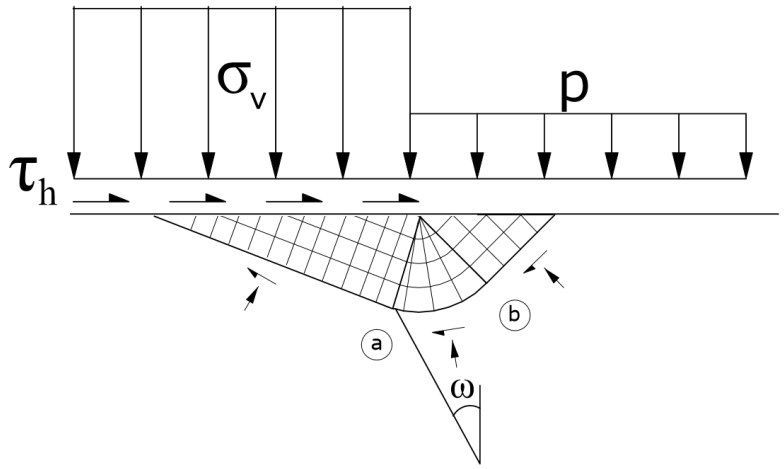


Figure 3.9: Stress field for a centric, inclined load in a total stress analysis ( from Grande et al. [2016])

following formula for $N_\gamma$ which only depends on friction angle:

$$\begin{aligned} N_\gamma &= e^{\,0.66+5.11\cdot\tan\varphi^*}\cdot\tan\varphi^* \;\; (rough\ footings) \\ N_\gamma &= e^{\,5.1\cdot\tan\varphi^*}\cdot\tan\varphi^* \;\; (smooth\ footings) \end{aligned} \tag{3.24}$$

where $\tan\varphi^*$ is defined to take into account for non-associating flow:

$$\tan\varphi^* = \frac{cos\psi\cdot sin\varphi}{1-sin\psi\cdot sin\varphi} \tag{3.25}$$

In this equation, $\psi$ is the dilation angle and $\varphi$ is the friction angle. A graphical representation of the dimensionless bearing factor, namely $N_\gamma$, can be seen in Figure 3.12. The figure shows how $N_\gamma$ would differ between a smooth and rough footing. It also shows the significance of the dilation angle, $\psi$ in the proposal of Michalowski [1997].

## 3.5 Martin's bearing capacity

When considering the self-weight of soil, the stress characteristics field is not necessarily kinematically admissible and it is not necessarily possible to extend the stress field outside of the plastic zones (Frydman and Burd [1997]). This means that solutions obtained by this method are not necessarily exact or even lower bound to the exact solution (Frydman and Burd [1997]). A further complication is the assumption of rough footing which according to Martin [2005] and Frydman and Burd [1997], "*the precise nature of the boundary condition that should be applied at the base of footing is not clear*".

When considering the weight of soil, shear strength is going to increase with depth, hence any velocity discontinuity which were assumed to be straight in Prandtl [1921] theories, are

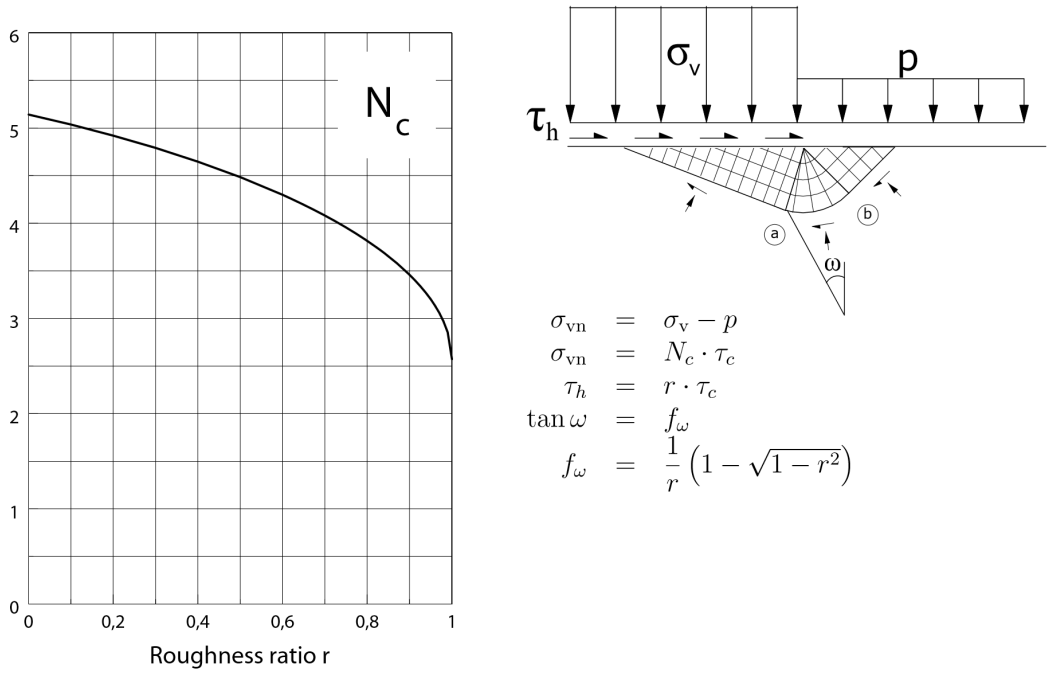


Figure 3.10: Bearing Capacity factor, $N_c$ diagram Grande et al. [2016]

now curved and their model can not feature the exact solution. According to Martin [2005], most methods assume a *a priori* failure geometry and try to find a stress field which can lead to failure. This assumption is not necessarily correct. Instead, Martin [2005] builds a stress field and a velocity field associated with it and tries to match these two. Figure 3.13 shows what these two fields look like.

By integrating the traction on the boundary beneath the footing, and calculation of internal and external work rates in the velocity field, lower bound and upper bound answers can be obtained for the bearing capacity problem. By performing a series of more accurate analyses, by having finer mesh and lower allowable error, these two answers can get close to each other. The author then assumes a cohesionless soil and finds the bearing capacity factor, $N_\gamma$ by:

$$N_\gamma = \lim_{\gamma B/q \to \infty} 2Q_u/\gamma B^2 \tag{3.26}$$

Martin [2004] details how a couple of iterations were used to converge upper and lower bound solutions to get $N_\gamma$ factors with 4 digit precision. Figure 3.14 shows bearing capacity calculated by Martin [2004] for footing with different smoothness.

Martin [2005] assumed the following in his work:

- Plane strain situation
- Associated flow rule, $\psi = \varphi$
- centric vertical loading

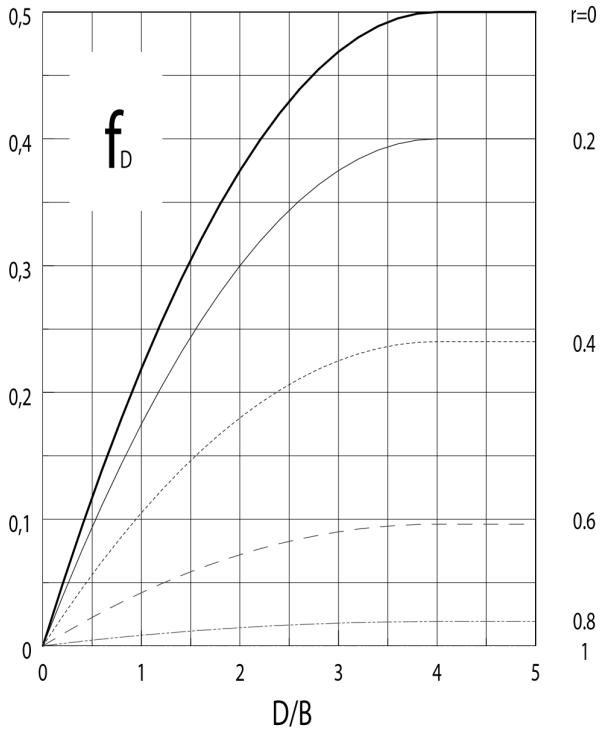


Figure 3.11: Correction for depth factor for total stress analysis ( from Grande et al. [2016])

#### 3.5.0.1 Solution proposed by geotechnical engineering group of University of Newcastle

Hjiaj et al. [2005] build his method on two previous works; first by using mathematical foundations laid by Lyamin and Sloan [2002a] which finds a lower bound solution by using the finite element method, the second work is the upper bound method described by Lyamin and Sloan [2002b]. Hjiaj et al. [2005] ran upper bound and lower bound analyses to get a lower bound and upper bound bearing capacity. These analyses were find-tuned by using finer mesh until relative error (the difference between lower bound and the average) becomes sufficiently small.

Hjiaj et al. [2005] states that a slip method will yield an upper bound solution if a kinematically admissible velocity field can be yielded by the integration of stress-strain equations for soil mass. If the same stress field can be extended to the soil mass inside the failure line in a way that boundary conditions, equilibrium equations and yield conditions of the soil are satisfied, then the same solution is also a lower bound and hence, the exact solution (the approach taken by Martin [2004]).

Hjiaj et al. [2005] ran analyses for different friction angles and then assigned averages of Lower and upper bound results to each friction angle. They proposed the following fitting formula for predicting $N_\gamma$ for rough foundations:

$$N_\gamma = e^{\pi+3\pi^2 \tan\varphi} \cdot \tan^{\frac{2\pi}{3}} \varphi \tag{3.27}$$

The authors stated that this formula has a maximum error of ± 3.42 %. This formula matches

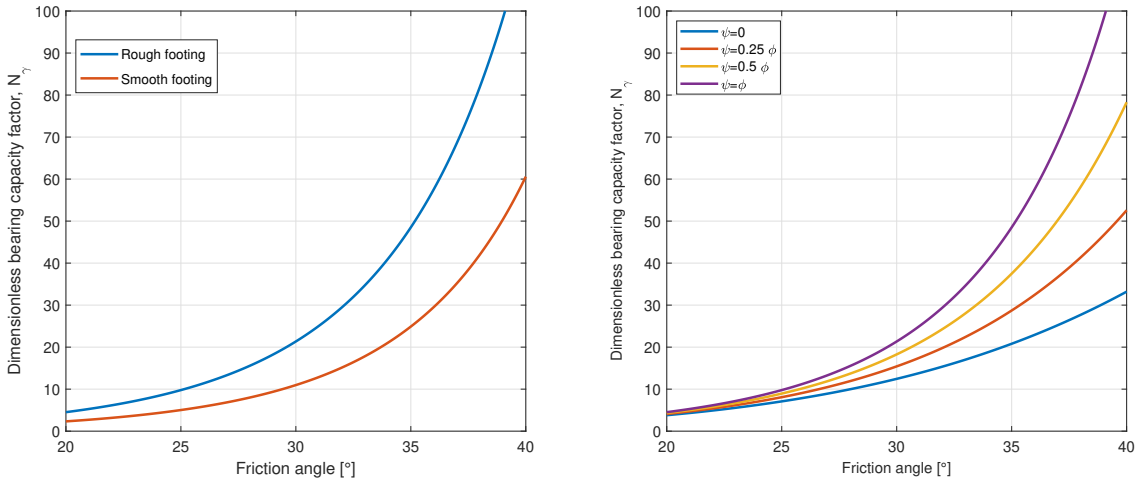


(a) Smooth/rough footing

(b) non-associated flow (rough footing)

Figure 3.12: Graphical representation of $N_\gamma$ proposed by Michalowski [1997]

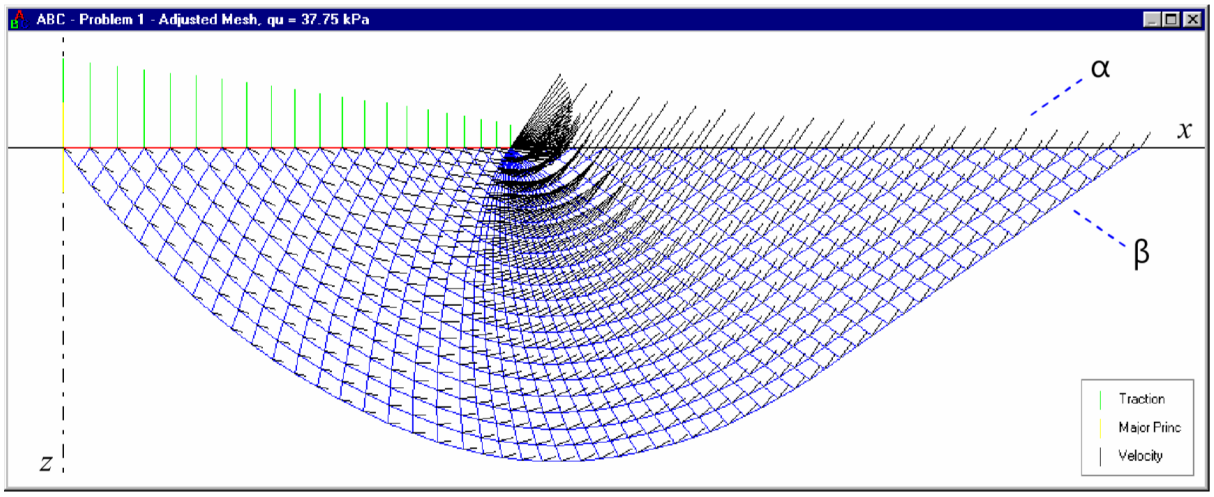


Figure 3.13: Stress and velocity field generated by ABC program (from Martin [2005])

quite well with the factors proposed by Martin [2004] as well. The bearing capacity factors, $N_\gamma$, predicted by Equation 3.27 have a maximum 2% difference from Martin [2004] results, which means the equation is sufficiently exact to be used. The authors also ran the same simulation with a smooth foundation and found roughness factor, $\beta$, which is defined as:

$$\beta = \frac{N_\gamma^{smooth}}{N_\gamma^{rough}} \tag{3.28}$$

Table 3.1 shows the calculated $\beta$ factors. It can be seen that for most realistic friction angles, namely between 20 ° and 45 °, the $\beta$ factor is about 0.5 which is in agreement with the value suggested by Meyerhof [1951].

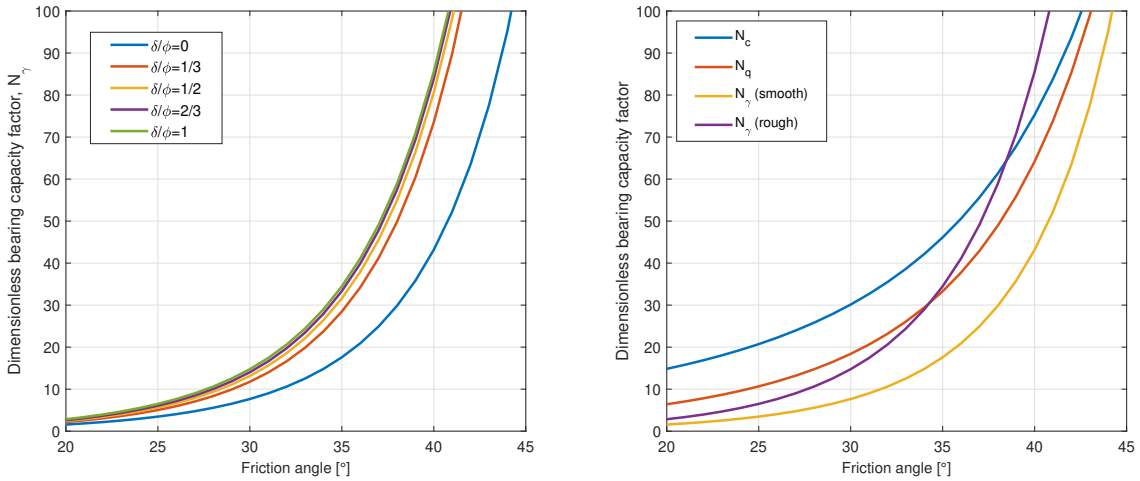


(a) $N_\gamma$ in Smooth/rough footings

(b) $N_c$, $N_q$ and $N_\gamma$

Figure 3.14: Graphical representation of proposed bearing capacity factors by Martin [2004]

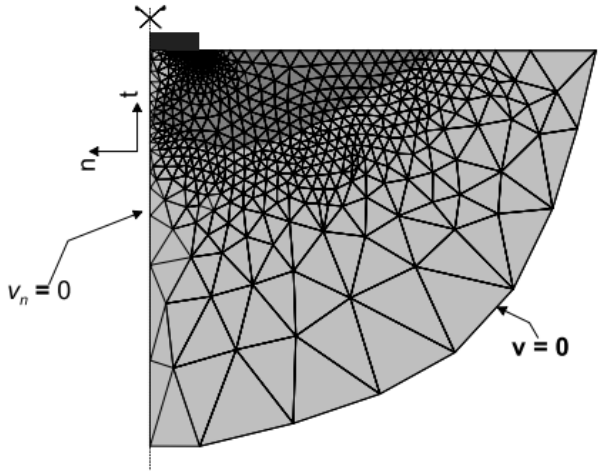


Figure 3.15: An example of meshing and boundary condition for a upper bound analysis (from Hjiaj et al. [2005])

#### 3.5.0.2 Loukidis and Salgado's bearing capacity proposals

By using finite element code *SNAC*, Loukidis and Salgado [2009] performed analyzes using the elastic-perfectly plastic Mohr-Coulomb model and investigated the effect of dilatancy angle on bearing capacity and tried to find $N_\gamma$, $N_q$ and shape factors for circular footings.

The authors used the pair of dilatancy angles and friction angles seen in Table 3.2 to test the effect of the dilancy factor in calculating bearing capacity. As stated in Nordal [2016], by introducing non-associated flow rule to an MC model, the solution can not reach a defined, constant maximum load.

Figure 3.16 shows how maximum shear strain increments align with the collapse mechanism suggested by Martin [2004]. For associated flow cases in both weightless and ponderable

Table 3.1: Roughness factor, $\beta$ calculated for different friction angles (from Hjiaj et al. [2005])

| $\varphi$ | 5 ° | 10 ° | 15 ° | 20 ° | 25 ° | 30 ° | 35 ° | 40 ° | 45 ° |
|---|---|---|---|---|---|---|---|---|---|
| $\beta$ | 0.76 | 0.65 | 0.6 | 0.56 | 0.54 | 0.53 | 0.52 | 0.51 | 0.51 |

Table 3.2: Sets of dilancy angles and friction angles used in analyses Loukidis and Salgado [2009]

| Friction angle, $\varphi$ ° | Dilatancy angle, $\psi$ ° | | | |
|---|---|---|---|---|
| | Set 1 | Set 2 | Set 3 | Set 4 |
| 30 | 30 | 10 | 2 | - |
| 35 | 35 | 15 | 6 | 2 |
| 40 | 40 | 20 | 12 | 6 |
| 45 | 45 | 25 | 18 | 12 |

soil the two mechanisms align perfectly (Bearing capacity program ABC uses associated flow rule). Further, the authors run these two sets of analyses (weightless soil with surcharge, and,

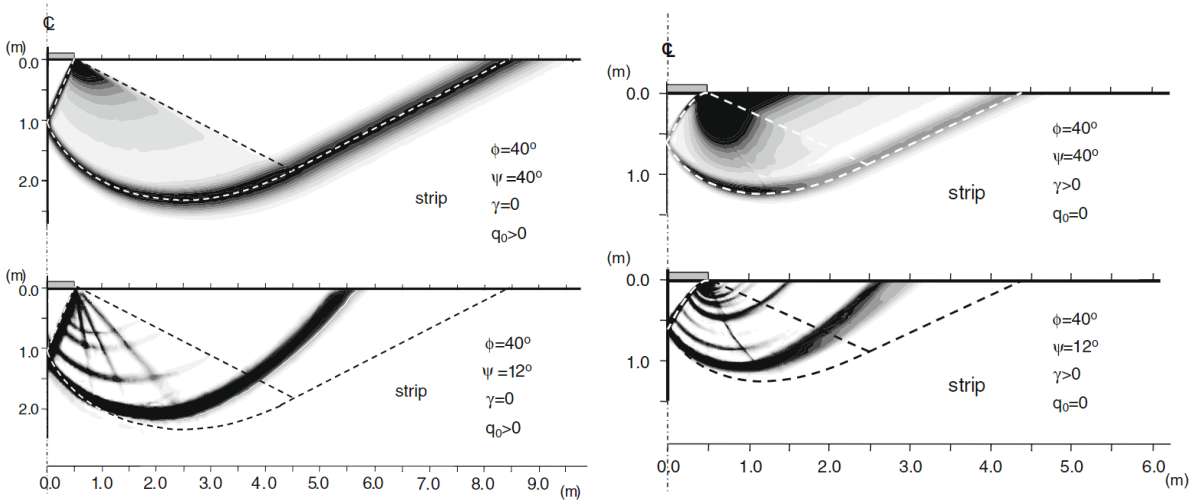


(a) Weightless soil

(b) Ponderable soil (no surcharge)

Figure 3.16: Maximum shear strain increments compared to the collapse mechanism (dashed lines) by Martin [2004] (from Loukidis and Salgado [2009])

ponderable soil without surcharge) and they found the bearing capacity factors, namely $N_q$ and $N_\gamma$. Those factors were compared to their exact values (see Figure 3.17). The figures show the case of $\psi = \varphi$ is very close to their exact solution. Loukidis and Salgado [2009] suggest following formula for calculating $N_q$ in materials with non-associated flow behavior:

$$N_q = \frac{1+\sin\varphi}{1-\sin\varphi} \cdot e^{F(\varphi,\psi)\cdot\pi\cdot\tan\varphi} \tag{3.29}$$

where:

$$F(\varphi,\psi) = 1 - \tan\varphi\Big(\tan\big(0.8\cdot(\varphi-\psi)\big)\Big)^{2.5} \tag{3.30}$$

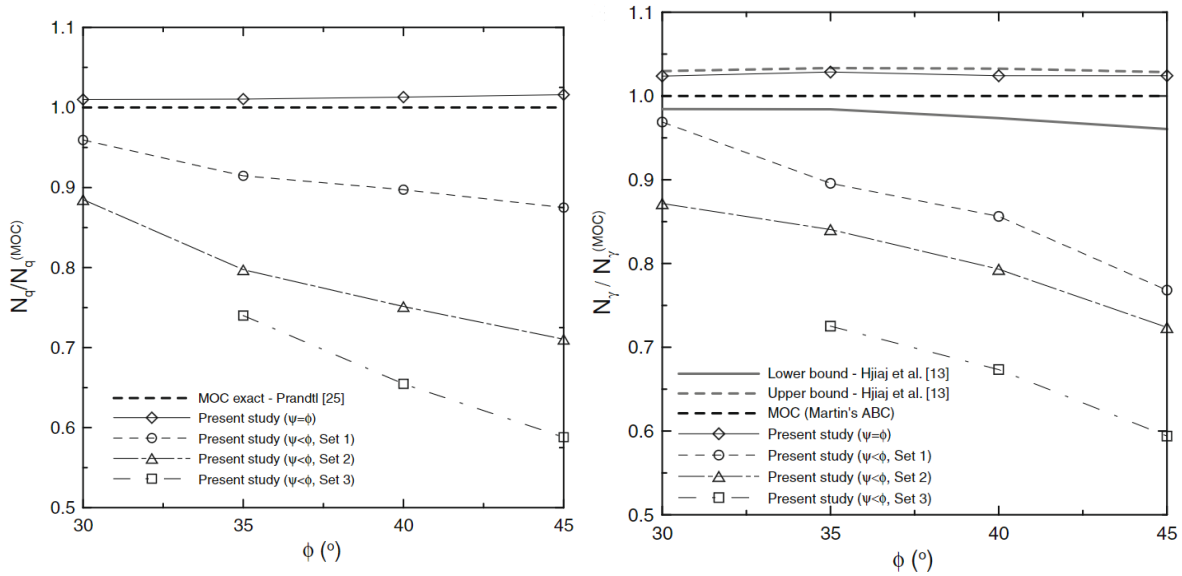


(a) bearing capacity factor $N_q$

(b) bearing capacity factor $N_\gamma$

Figure 3.17: Comparison of results of bearing capacity factors obtained by Loukidis and Salgado [2009] and other works (from Loukidis and Salgado [2009])

The authors make a similar formula for predicting $N_\gamma$:

$$N_\gamma = \tan(1.34 \cdot \varphi) \cdot \left( \frac{1+\sin\varphi}{1-\sin\varphi} \cdot e^{F(\varphi,\psi)\cdot\pi\cdot\tan\varphi} - 1 \right) \tag{3.31}$$

The authors run their analyses for circular foundations as well for computing shape factors. They proposed the following formulas for shape factors:

$$s_\gamma^{circular} = 1 + \left( 0.26 \cdot \frac{1+\sin\varphi}{1-\sin\varphi} - 0.73 \right) \tag{3.32}$$

$$s_q^{circular} = 1 + 2.9 \cdot \tan^2\varphi \tag{3.33}$$

$s_\gamma$ shows acceptable error margin (at most 2%) but this is not the same case for $s_q$ which has a maximum 9% error margin. In reality, bearing capacity of square or circular footing is smaller than the strip footing (no embedment), however, the theoretical solution shows the opposite. This is because the friction angle is lower in a circular/square loading where the loading is closer to triaxial loading. Meyerhof [1951] suggests using a 10% higher friction angle for strip footing (when the friction angle is interpreted from triaxial tests (more on this in Chapter 7).

## 3.6 Eurocode Design Methods

Norsk Standard [2016], annex D suggests following relations for finding bearing capacity in both total and effective stress analysis:

### 3.6.1 Total stress

The proposed equation for calculating bearing capacity on a total stress basis is:

$$\sigma_v = (\pi + 2) \cdot b_c \cdot S_c \cdot i_c \cdot S_u + p \tag{3.34}$$

Where $b_c$ is the factor to take into account inclination of footing to the horizontal ($\alpha$) and it is defined as:

$$b_c = 1 - \frac{2 \cdot \alpha}{\pi + 2} \tag{3.35}$$

and shape factors are defined as:

$$s_c = 1 + 0.2 \cdot \frac{B}{L} \qquad rectangular\ footing \tag{3.35a}$$

$$s_c = 1.2 \qquad square\ or\ circular\ footing \tag{3.35b}$$

and inclination factor caused by a horizontal load of H, on footing with area A:

$$i_c = \frac{1}{2} \cdot \left(1 + \sqrt{1 - \frac{H}{A \cdot S_u}}\right) \tag{3.36}$$

### 3.6.2 Effective stress

The following equation is proposed for calculating bearing capacity in effective stress:

$$q_{ult} = s_c \cdot b_c \cdot i_c \cdot N_c \cdot c + s_q \cdot b_q \cdot i_q \cdot N_q \cdot p' + \frac{1}{2} \cdot s_\gamma \cdot b_\gamma \cdot i_\gamma \cdot N_\gamma \cdot \gamma \cdot B \tag{3.37}$$

where bearing capacity factors are defined as:

$$\begin{aligned} N_q &= e^{\pi \tan \varphi} \tan^2(45 + {}^{\varphi}/_{2}) \\ N_c &= (N_q - 1) \cdot \cot \varphi \\ N_\gamma &= 2 \cdot (N_q - 1) \cdot \tan \varphi \qquad where\ \delta \geq {}^{\varphi}/_{2}\ (rough\ base) \end{aligned} \tag{3.38}$$

The factors for taking inclination of the foundation base into account are defined as follow:

$$\begin{aligned} b_q = b_\gamma &= (1 - \alpha \cdot \tan \varphi)^2 \\ b_c &= b_q - \frac{1 - b_q}{N_c \cdot \tan \varphi} \end{aligned} \tag{3.39}$$

and shape factors of overburden constituent, $s_q$, are defined as follows:

$$s_q = 1 + \frac{B}{L} \cdot \sin\varphi \qquad rectangular\ footing \tag{3.39a}$$

$$s_q = 1 + \sin\varphi \qquad square\ and circular\ footing \tag{3.39b}$$

(3.40)

and shape factors of density constituents, $s_\gamma$, are defined as follows:

$$s_\gamma = 1 - 0.3 \cdot \frac{B}{L} \qquad rectangular\ footing \tag{3.40a}$$

$$s_\gamma = 0.7 \qquad square\ and\ circular\ footing \tag{3.41}$$

(3.41a)

and shape factors of cohesion constituents for all shapes:

$$s_c = \frac{s_q \cdot N_q - 1}{N_q - 1} \tag{3.42}$$

and finally, inclination factors are defined as (H is the horizontal load):

$$\begin{aligned} i_c &= i_q - \frac{1 - i_q}{N_c \cdot \tan\varphi} \\ i_q &= \left(1 - \frac{H}{V + A \cdot c \cdot \cot\varphi}\right)^m \\ i_\gamma &= \left(1 - \frac{H}{V + A \cdot c \cdot \cot\varphi}\right)^{m+1} \end{aligned} \tag{3.43}$$

where:

$$m = \frac{2 + B/L}{1 + B/L} \qquad H\ in\ the\ direction\ of\ B \tag{3.43a}$$

$$m = \frac{2 + L/B}{1 + L/B} \qquad H\ in\ the\ direction\ of\ L \tag{3.43b}$$

## 3.7 Conclusion

It should be noted that the solution presented by Martin [2004], which gives the most precise solution of $N_\gamma$, will be called *exact solution* from now on.

Chapter 4

# Methods

## 4.1 Introduction

The limit analysis is a tool that can give a rigorous solution for simple geotechnical problems. By discretization of the problem domain by use of the finite element, it is possible to use the plasticity theorem to solve more complex geotechnical problems. Finite element limit analysis (FELA) is a newly developed method that finds the lower and upper bound solution by using optimization techniques. This method is executed by increasing external load(s) or reducing material strength (c-$\varphi$ analysis) up until the failure point. This chapter will explain the fundamentals of this method, which is the foundation of this thesis.

## 4.2 Limit analysis

In classical soil mechanics, the soil is assumed to be perfectly elastic-rigid plastic, which means soil's state of failure is independent of loading history. With this assumption, the focus will be on the way the structure, in or on soil, might collapse. The goal is to find a factor of external load(s) that if exerted on the structure, the soil under or around it can fail. Plasticity theorems help us to find bounds of exact collapse load without constructing an incremental load-deformation analysis. For this purpose, two theorems famously referred to as lower bound theorem, or static approach, and upper bound theorem, or kinematic approach, are being used. The purpose of limit analysis is to find the set of two loads, namely $F_c^k$ and $F_c^s$, which satisfies the upper and lower bound theorems, for a case with known boundary conditions and a soil mass with given strength parameters, Huang and Yu [2017].

The solution obtained by the lower bound theorem is always on the lower bound if it is not equal to the exact solution. This gives the advantage of always being on the safe side. On the

contrary, the solution obtained by the upper bound theorem is always on the upper bound side of the exact solution, if not equal to the exactly correct solution. This means that the theorem gives an unsafe estimate of the collapse load. If the gap between the two solutions obtained by upper and lower bound gets smaller, it means that the two solutions are getting closer to the exact solution. The average of the two solutions usually gives a good estimate of the exact solution. The goal of refining the solution is always to close this so-called gap between upper and lower solution, Huang and Yu [2017].

### 4.2.1 Lower Bound Theorem

In the classical soil mechanics, for applying the theorem of lower-bound, a statically admissible stress field has to be defined which is in equilibrium with the external loads applied on boundaries. These stress fields have to not violate the yield conditions. Thus the collapse cannot occur.

The lower-bound theorem states the following (from Drucker and Prager [1952]):

*"If all changes in geometry occurring during collapse are neglected, a statically admissible collapse load, $F_c^s$, is always less than or equal to the exact collapse load $F_c$ (i.e., $F_c^s \leq F_c$). The equality sign is valid only when the statically admissible stress field is the true stress field. In other words, the load derived from a statically admissible stress field, $F_c^s$, is a lower bound of the true collapse load, $F_c$."*

### 4.2.2 Upper Bound Theorem

For this theorem to be admissible, assumed plastic mechanics has to be compatible. Then, this theorem states that if the rate of work caused by external loads is equal to the rate of internal dissipation of energy, then structure collapses.

In other words, The upper bound theorem states the following (from Drucker and Prager [1952]):

*"If all changes in geometry occurring during collapse are neglected, a kinematically admissible collapse load, $F_c^k$, is always greater than or equal to the exact collapse load $F_c$ ($F_c^k \geq F_c$). The equality sign is valid only when the kinematically admissible velocity field is the true velocity field. In other words, the load derived from a kinematically admissible velocity field, $F_c^k$, is an upper bound on the true collapse load factor."*

## 4.3 Finite element limit analysis

### 4.3.1 Utilized program

In this thesis, Optum G2, for two-dimensional-analyses, and Optum G3, for three dimensional analyses, was used.

### 4.3.2 Philosophy

As discussed, the main goal of limit analysis is to find the maximum magnitude of external loads that a soil body can take without leading to structure failure. Finite element limit analysis finds lower and upper bound multiplier of collapse load. Lower bound limit analysis tries to approach the "real answer" from below by increasing the admissible load, and the upper bound limit analysis is trying to approach it from above, by decreasing the admissible load. This concept is depicted in Figure 4.1.

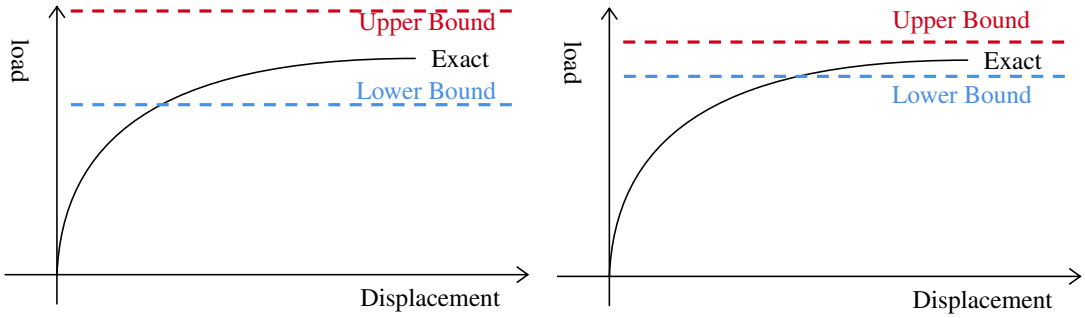


(a) Coarse Meshing (b) Fine Meshing

Figure 4.1: Upper and Lower Bound Solution in comparison to exact solution

Throughout this thesis, results of the lower and upper bound will be compared to each other by comparing the error of the results. For cases where there is a rigorous theoretical solution, absolute relative error is used, which is equal to:

$$\eta = \frac{x_{upper-lower\ bound} - x_{exact}}{x_{exact}} \cdot 100\% \tag{4.1}$$

For the cases where there are no theoretical solutions, the absolute relative error is found as:

$$\eta = \frac{x_{upper-lower\ bound} - x_{average}}{x_{average}} \cdot 100\% \tag{4.2}$$

where $x_{average}$ is the average of upper and lower bound solutions.

## 4.4 Theory behind finite element limit analysis

In this section, a quick introduction to the theory behind FELA will be given. Krabbenhøft et al. [2016d] explains the foundation and theory of the program in detail and the purpose of this chapter is not to give a full account of the theory but to give a summary of it.

### 4.4.1 Governing Equations

The foundation of the method builds up on formulating equations for perfectly rigid materials. Rigid materials do not deform until the yield point where they show unlimited plastic deformation. The governing equation for this type of materials uses velocity (deformation rate).

In a statistic problem setting, the problem in hand has a geometry like this:

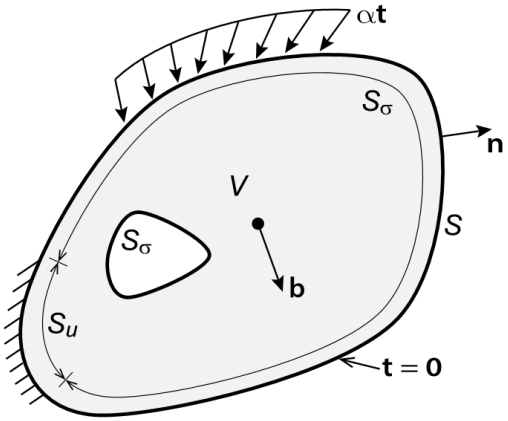


Figure 4.2: A solid with volume of V and boundary of S (sum of supported boundary, $S_u$ and boundary subjected to traction, $S_\sigma$) (from Krabbenhøft et al. [2016d])

static equilibrium (shown here for two-dimensional plane strain) has to be satisfied:

$$\begin{aligned} \frac{\partial \sigma_x}{\partial x} + \frac{\partial \tau_{xy}}{\partial y} + b_x = 0 \\ \frac{\partial \sigma_y}{\partial y} + \frac{\partial \tau_{xy}}{\partial x} + b_y = 0 \end{aligned} \tag{4.3}$$

or in matrix form:

$$\nabla^T \boldsymbol{\sigma} + \mathbf{b} = 0 \quad in \;\; V \tag{4.4}$$

here $\mathbf{b} = (b_x, b_y)^T$ is the body force and $\nabla^T$ is defined as:

$$\nabla^{\mathbb{T}} = \begin{vmatrix} \partial/\partial x & 0 & 0 & \partial/\partial y \\ 0 & \partial/\partial y & 0 & \partial/\partial x \end{vmatrix} \tag{4.5}$$

The boundary condition can be expressed as follows:

$$\begin{aligned} n_x\sigma_x + n_y\tau_{xy} &= \alpha t_x + t_{s_x} \\ n_y\sigma_y + n_x\tau_{xy} &= \alpha t_y + t_{s_y} \end{aligned} \tag{4.6}$$

where $\alpha$ is a load multiplier, $t_s$ is external load due to steady-state pore pressure, and $t_x$ and $t_y$ are the components of the traction in x and y direction and $\mathbf{n} = (n_x,\ n_y)^T$ is the outward normal force on the boundary in the x and y direction. This equation can be written in short form as:

$$\mathbf{P}^T\boldsymbol{\sigma} = \alpha\mathbf{t} \quad on\ \ S_\sigma \tag{4.7}$$

where:

$$\mathbb{P}^{\mathbb{T}} = \begin{vmatrix} n_x & 0 & n_y \\ 0 & n_y & n_x \end{vmatrix} \tag{4.8}$$

and yield condition has to be satisfied:

$$F(\sigma) \leq 0 \tag{4.9}$$

By linearization, the yield condition can be written as:

$$\boldsymbol{F}^T - \boldsymbol{k} + \boldsymbol{s} = \mathbf{0},\ \ \boldsymbol{s} \geq \mathbf{0} \tag{4.10}$$

Total strain is sum of plastic strain and elastic strain:

$$\boldsymbol{\epsilon} = \boldsymbol{\epsilon}^e + \boldsymbol{\epsilon}^p \tag{4.11}$$

where $\epsilon^e$ is the elastic strain and $\epsilon^p$ is the plastic strain. Elastic strain is equal to:

$$\boldsymbol{\epsilon}^e = \mathbb{C}\boldsymbol{\sigma} \tag{4.12}$$

where $\mathbb{C}$ is an elastic compliance modulus. Then, the flow rule states:

$$\dot{\boldsymbol{\epsilon}}^p = \dot{\lambda}\frac{\partial G}{\partial \boldsymbol{\sigma}} \quad where\ \ \dot{\lambda} \geq 0 \tag{4.13}$$

where $\dot{\epsilon}^p$ is the plastic strain rate and $\dot{\lambda}$ is plastic multiplier and G is a flow potential. Plastic strains occur when F($\sigma$) = 0, i.e. when soil is at collapse point. In other words, yielding condition has to be satisfied for yielding to happen:

$$\dot{\lambda}F(\boldsymbol{\sigma}) = 0 \tag{4.14}$$

Assuming strains are small enough, velocity field can be derived as:

$$\dot{\epsilon}^p = \nabla\dot{\boldsymbol{u}} \tag{4.15}$$

By Combining two equations, we have:

$$\nabla \dot{\boldsymbol{u}} = \dot{\lambda} \frac{\partial G}{\partial \boldsymbol{\sigma}} \tag{4.16}$$

If a model has hardening mechanisms, it can be modelled by assuming some variables, here: $\boldsymbol{\kappa} = (\kappa_1, \ldots, \kappa_n)^T$. The elastic domain is then given by:

$$F(\boldsymbol{\sigma}, \boldsymbol{\kappa}) \leq 0 \tag{4.17}$$

and here $F(\sigma, \kappa) = 0$ defines yield surface. Hardening rule is defined as:

$$\dot{\boldsymbol{\kappa}} = \dot{\lambda} \boldsymbol{h}(\boldsymbol{\sigma}, \boldsymbol{\kappa}) \tag{4.18}$$

where $\mathbf{h} = (h_1, \ldots, h_n)^T$ are hardening functions. Hardening happens when $\dot{\lambda} > 0$.

**Summary**

The governing equations can be expressed as follows:

$$\begin{aligned} \dot{\boldsymbol{\epsilon}} &= \mathbb{C}\dot{\boldsymbol{\sigma}} + \dot{\lambda} \nabla_\sigma G(\boldsymbol{\sigma}, \boldsymbol{\kappa}) \\ \dot{\boldsymbol{\kappa}} &= \dot{\lambda} \boldsymbol{h}(\boldsymbol{\sigma}, \boldsymbol{\kappa}) \\ F(\boldsymbol{\sigma}, \boldsymbol{\kappa}) \leq 0, \quad \dot{\lambda} F(\boldsymbol{\sigma}, \boldsymbol{\kappa}) &= 0, \quad \dot{\lambda} \geq 0 \end{aligned} \tag{4.19}$$

where $\nabla_\sigma G$ is equal to $\partial G / \partial \sigma$.

### 4.4.2 Principle of virtual work

The principle of virtual work can be expressed as:

$$\int_V \boldsymbol{\sigma}^T \nabla \boldsymbol{u} dV - \int_V \boldsymbol{b}^T \boldsymbol{u} dV - \int_s (\boldsymbol{t} + \boldsymbol{t}_s)^T \boldsymbol{u} dS = 0 \tag{4.20}$$

where **u** satisfies kinematic boundary conditions.

### 4.4.3 Complete Solution for Limit analysis

As it is done in many hand calculations of the upper bound method, Optum assumes a soil collapses when some magnitude of strain (shear strain) happens in the soil body.

#### 4.4.3.1 Lower bound principle

It is possible to state the governing equations in terms of lower principles, here the goal is to maximize $\alpha$ subjected to:

$$\begin{aligned} \nabla^T \boldsymbol{\sigma} + \mathbf{b} = 0 \quad & in \ V \\ \mathbf{P}^T \boldsymbol{\sigma} = \alpha \mathbf{t} \quad & on \ S_\sigma \\ \boldsymbol{F}^T - \boldsymbol{k} + \boldsymbol{s} = \mathbf{0}, \ \ & \boldsymbol{s} \geq \mathbf{0} \end{aligned} \tag{4.21}$$

This solution finds the collapse multiplier by finding a stress field that satisfies the equilibrium and boundary condition without trying to find an optimal solution.

As mentioned in Section 4.2.1, a geometry with perfectly plastic materials will collapse if a stress field can be found which can satisfy the following conditions:

- The equilibrium equations
- The boundary condition
- The yield condition

The external loads which are part of a stress field are a lower bound to the load(s) which causes collapse in soil mass.

#### 4.4.3.2 Upper bound principle

Upper bound problems can be expressed as an optimization problem where the goal is to minimize the following:

$$\int_V \boldsymbol{k}^T \dot{\boldsymbol{\lambda}} dV - \int_V \boldsymbol{b}^T \dot{\boldsymbol{u}} dV + \int_S \boldsymbol{t}_s^T \dot{u} dS \tag{4.22}$$

subjecting to the following equations:

$$\begin{aligned} \nabla \dot{\boldsymbol{u}} = \boldsymbol{F} \dot{\boldsymbol{\lambda}}, \ \ & \dot{\boldsymbol{\lambda}} \geq \mathbf{0} \\ \int_{S_\sigma} \boldsymbol{t}^T \dot{\boldsymbol{u}} dS = 1 & \end{aligned} \tag{4.23}$$

This solution tries to find a solution for flow rule by postulating a compatible velocity field. The multiplier, $\alpha$, is found based on the internal rate of work.

In other words, if a ratio of internal to external work equal or higher than the ratio that failure can be found, by satisfying the following requirements, the upper bound solution will be achieved:

- The strain-displacement relations
- The associated flow rule

- The displacement boundary condition

What is meant by the associated flow rule here (Equation 4.11), is a rule which relates the normal strain and shear strains at failure point to the failure envelope via a normality rule.

#### 4.4.3.3 Adaptive meshing

Throughout this thesis, adaptive meshing is used to get more precise results. The idea is to run an analysis first with a homogeneous meshing size all over the soil media, then based on the results of that simulation, generate a denser and finer mesh alongside the area with high shear dissipation. This iterative process generally results in a more precise solution than the normal meshing (Krabbenhøft et al. [2016d]).

#### 4.4.3.4 Effect of flow rule

The associated flow rule has a considerable effect on how soil will deform but much less importance on the ultimate strength. "Limit Analysis" in the programs always assumes associated flow rule and the non-associated flow rule can be used in "Elastoplastic" and "Multiplier Elastoplastic" but not in the limit analysis. Davis [1968] suggests following friction angles and cohesion to be used when one is using a calculation method which assumes associated flow, like limit analysis in Optum G2:

$$\begin{aligned} c_D &= \frac{c}{\omega_D} \\ \varphi_D &= \arctan \frac{\tan \varphi}{\omega_D} \end{aligned} \tag{4.24}$$

where:

$$\omega_D = \frac{1 - \sin\varphi \sin\psi}{\cos\varphi \cos\psi} \tag{4.25}$$

By using these formulas, it is possible to correct for the effect of dilatancy angle.

### 4.4.4 Available type of element

There are 6 types of elements available in Optum. Here follows a short description, which is depicted in Figure 4.3. More details are available in Krabbenhøft et al. [2016d].

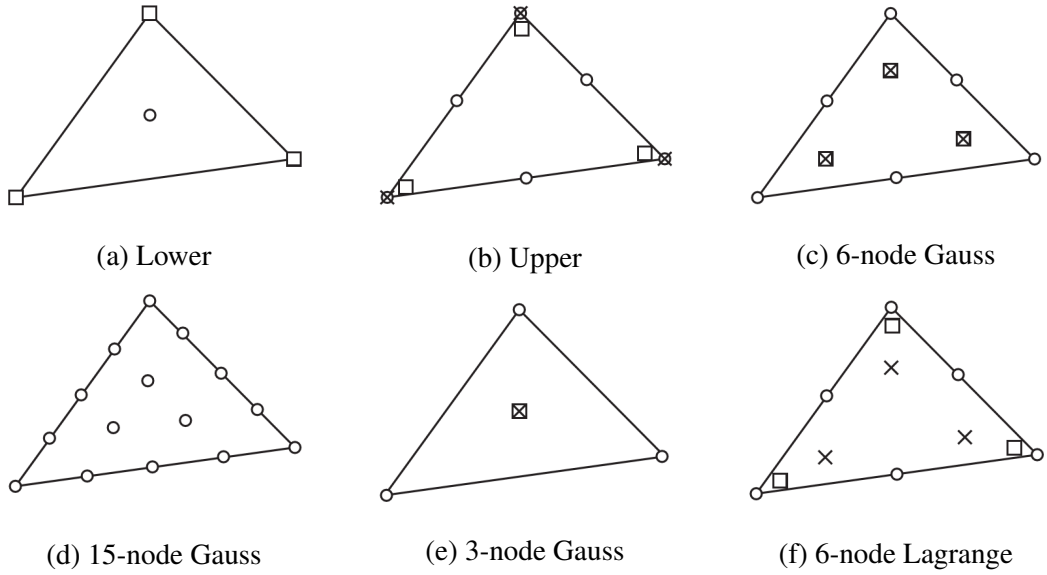

(a) Lower (b) Upper (c) 6-node Gauss

(d) 15-node Gauss (e) 3-node Gauss (f) 6-node Lagrange

Figure 4.3: Available elements in Optum G2, from Krabbenhøft et al. [2016d] (Displacement node: ∘ Stress node: □ Integration point: ×)

Following is an overview of elements available in the program:

1. Lower: This type of elements are used for rigorous lower bound. They uses a linear interpolation of stress and there are statically admissible stress discontinuities between elements (Lyamin and Sloan [2002a]).
2. Upper: This type of elements are used in rigorous upper bound. They uses linear interpolation of stresses and quadratic interpolation of displacement (Lyamin and Sloan [2002b]).
3. 6-node Gauss: This type of element, although not rigorous, converges from above. It uses linear interpolation of stress and quadratic interpolation of displacements.
4. 15-node Gauss: This type of element, although not rigorous, converges from above. It uses a cubic interpolation of stresses and 15 interpolation point for displacement.
5. 3-node Gauss: This type of element produces rigorous upper bound and may lead to a better result than an *upper* element type for highly confined problems.
6. 6-node Lagrange: This type of element produces better results than a 6-node Gauss element. It uses linear interpolation of stresses and quadratic interpolation of displacement.

## 4.5 User Interface

A short summary of user interface, different available features and their function are summarized in Appendix B (for more see Krabbenhøft et al. [2016a] and Krabbenhøft et al. [2016b]).

Chapter 5

# Numerical Limit Analysis in Tresca Soil

In this chapter, 8 cases of bearing capacity problems with the Tresca soil model will be investigated. The analyses are run with two-dimensional and three-dimensional versions of Optum and Matlab. For case 3 onward, more than a dozen analyses were done by utilizing the computational unit of Optum without interacting with the graphical user interface. This is done by running Optum by using Matlab API. The idea is to run Optum via the command prompt, get the results of the analysis, and update a soil parameter or geometry on a loop. By this automation, hundreds of analyses can be done with the help of MATLAB and the results can be fetched at the end. The codes used for this are summarized in Appendix C.

## 5.1 Case 1: Vertical Loading of Tresca Soil

In this case, the ultimate limit bearing capacity will be investigated for a Tresca soil under plane strain situation with vertical and centric loading with no overburden pressure.

### 5.1.1 Theoretical Solution

As shown in Section 3.3, there is an exact solution for a vertical, centric loading on a soil mass with the Tresca model. For this type of loading, the ultimate limit bearing capacity can be defined by:

$$\sigma_v = N_c \cdot S_u + p \tag{5.1}$$

where p is overburden pressure, $S_u$ is the undrained shear strength and $N_c$ is a bearing capacity factor which is defined in Equation 3.20. The famous solution of $N_c$ is equal to $2+\pi$ for a vertical loading.

### 5.1.2 Computation Results of *OptumG2* Runs

In this case, a bearing capacity problem was run on a soil in which the Tresca model was assigned. The model was run for a different number of meshes, with and without adaptive meshes.

#### 5.1.2.1 Geometry and Meshing

Figure 5.1 shows the geometry and the meshing used for this case with three different numbers of elements. Soil body has 10 m width and 4 m height and there is a rigid foundation with 1 m width resting on it.

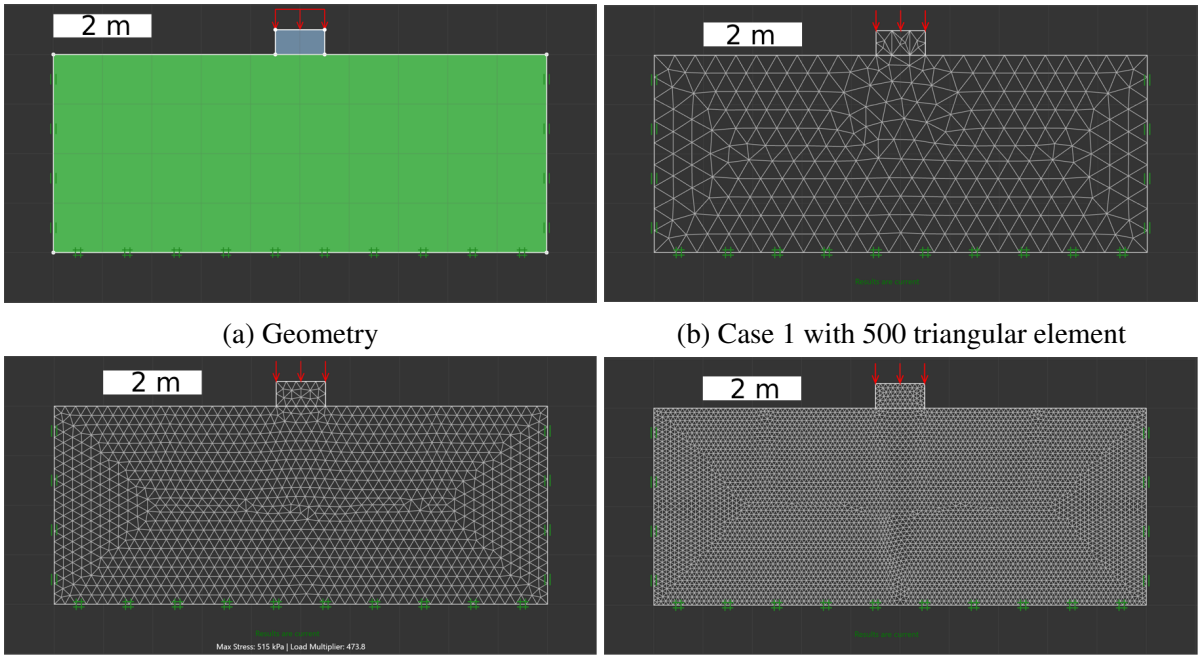


(a) Geometry

(b) Case 1 with 500 triangular element

(c) Case 1 with 2000 triangular element

(d) Case 1 with 10 000 triangular element

Figure 5.1: Geometry and meshing of case 1

Two types of meshing were used, namely conventional meshing and adaptive meshing. Adaptive meshing tries to put more refined elements where it is needed. Figure 5.2 shows how the adaptive mesh is putting denser and smaller elements where the shear dissipation has higher values.

#### 5.1.2.2 Results for regular meshing

Figure 5.3 shows normalized ultimate load (ultimate load divided by undrained shear strength) obtained for the different number of triangular elements. Both lower bound and upper bound

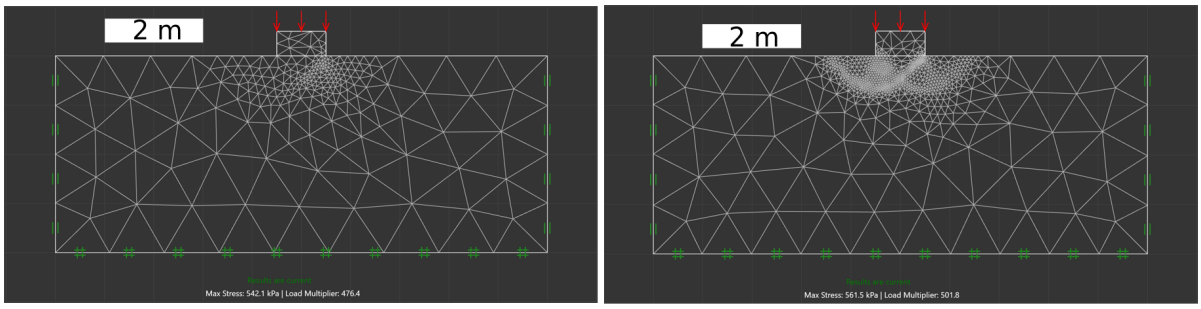


(a) Case 1 with 500 triangular element (b) Case 1 with 2000 triangular element

Figure 5.2: Case 1 with 3 iterations of adaptive meshing controlled by shear dissipation

simulations were run and their average is shown as well. Besides, the figure shows how the absolute relative error is decreasing by increasing the number of triangular elements.

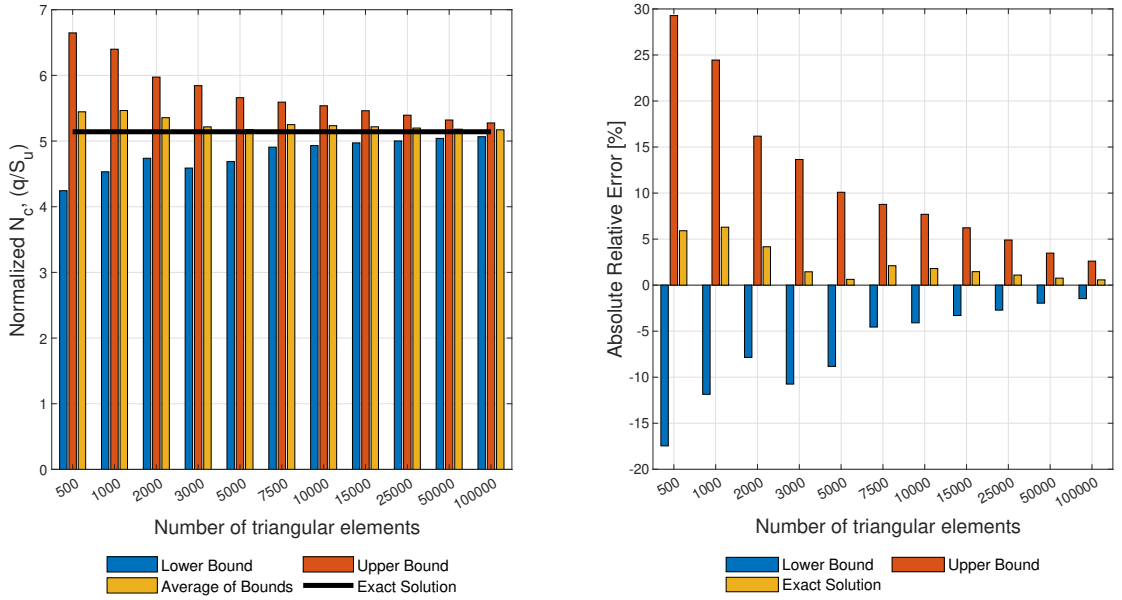


(a) Normalized ultimate load (b) Absolute relative error

Figure 5.3: Results for regular meshing (without adaptive meshing) for different number of triangular meshes

The figure shows how the gap between upper and lower bound closes as meshing gets more refined. Closing this gap gives more precision to the simulation.

#### 5.1.2.3 Results for meshing with adaptive meshing

Figure 5.4 shows the obtained normalized ultimate load for the different number of triangular elements. As earlier, results of the lower bound, upper bound, and their averages with the

absolute relative error is shown. It can be seen that absolute relative error is significantly lower and it reduces to small amounts by increasing the element number.

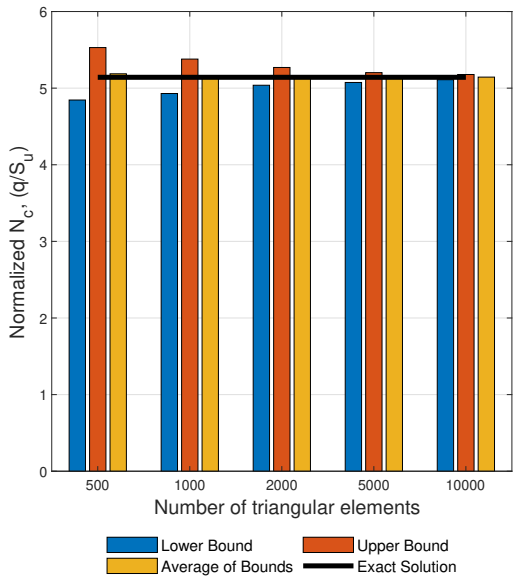


(a) Normalized ultimate load

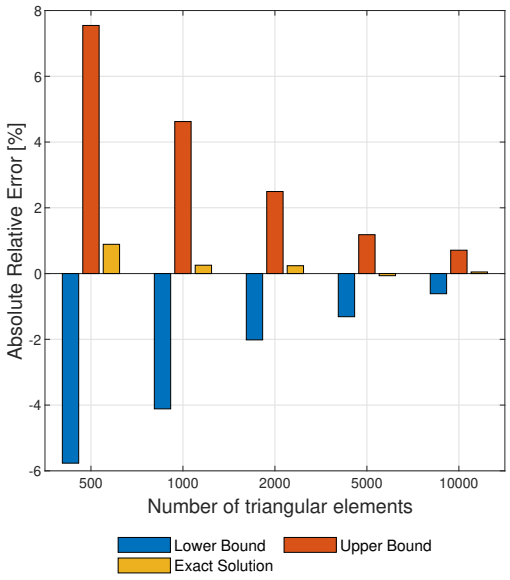


(b) Absolute relative error

Figure 5.4: Results for regular meshing (without adaptive meshing) for different number of triangular meshes

Figure 5.5 shows how the failure envelope developed by the theoretical solutions in Section 3.3 fits well with obtained results by the program. Furthermore, the figure shows how adaptive meshing refines meshing along the failure line.

#### 5.1.2.4 Comparison of results

Figure 5.6 shows a comparison of results from regular meshing and adaptive meshing. It shows how the average of lower and upper bound reduces from regular meshing to adaptive meshing for the same number of elements.

Bearing capacity problems are usually less computationally demanding, but for a more complicated problem, the importance of the distribution of elements is even higher. This simple case shows how putting the elements in the right place, even when the number of meshes is not significant, can reduce the calculation error effectively.

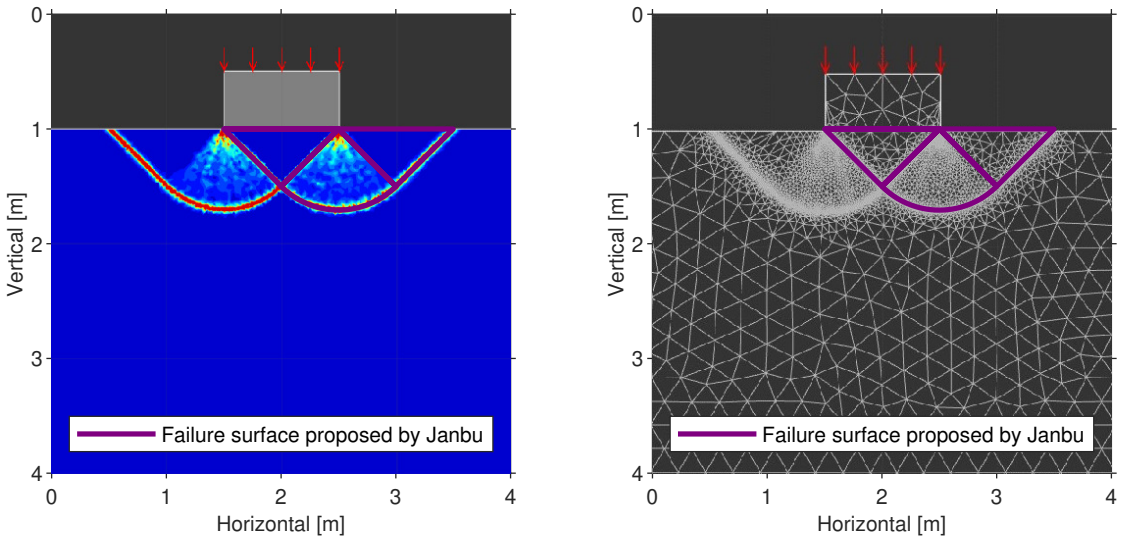


(a) shear dissipation (b) Mesh

Figure 5.5: Comparison of failure envelope developed by theoretical solutions and obtained results

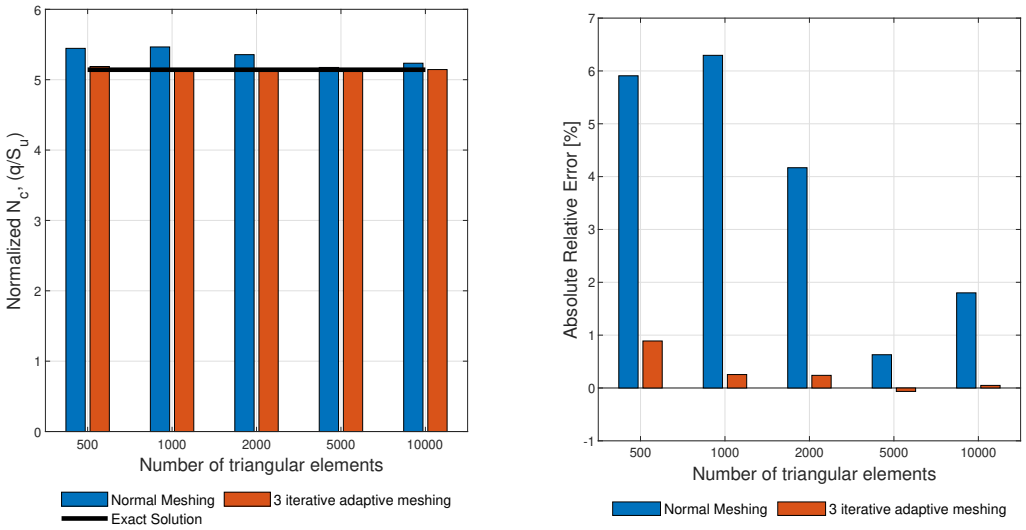


(a) Normalized ultimate load (b) Absolute relative error

Figure 5.6: Comparing the average of lower bound and upper bound between regular meshing and adaptive meshing

## 5.2 Case 2: Vertical Loading of a circular foundation on a Tresca Soil

In this case, the ultimate limit bearing capacity of circular footings will be investigated for a Tresca soil with vertical and centric loading with no overburden pressure. For this case, both three dimensional and two-dimensional versions of the program is going to be used.

### 5.2.1 Theoretical Solution

The solution for a circular foundation with centric loading on soil with the Tresca model is quite similar to the plane strain case. Ultimate limit bearing capacity can be defined as:

$$\sigma_v = N_c \cdot S_u + p \tag{5.2}$$

Cox et al. [1961] calculated bearing capacity factor $N_c$, for a circular foundation by using the method of characteristics, giving it an exact solution of 6.05. Another solution suggested by Meyerhof [1963] suggests another solution, where the $N_c$ is equal to 6.18, or roughly to $3+\pi$. Other solutions based on numerical analyses, such as Gourvenec and Randolph [2003], have suggested a bearing capacity factor equal to 6.05.

### 5.2.2 Computation Results of *OptumG2* Runs

In this case, bearing capacity of a circular foundation on a Tresca soil was computed. The two-dimensional version of the Optum, with axisymmetry, will be used. 5 runs, with a different number of elements, were used to run lower and upper bound analyses.

#### 5.2.2.1 Geometry and Meshing

Figure 5.7 shows the geometry and meshing for this case for a special case with 10.000 elements using regular meshing and meshing with 3 iterations of adaptive meshing. Soil body has 3 m width and 3 m height and there is a rigid foundation resting on it with 1 m radius.

#### 5.2.2.2 Results for regular meshing

Figure 5.8 shows normalized bearing capacity factor, $N_c$, obtained for a different number of triangular elements. By increasing the number of elements, the average of two bounds is getting

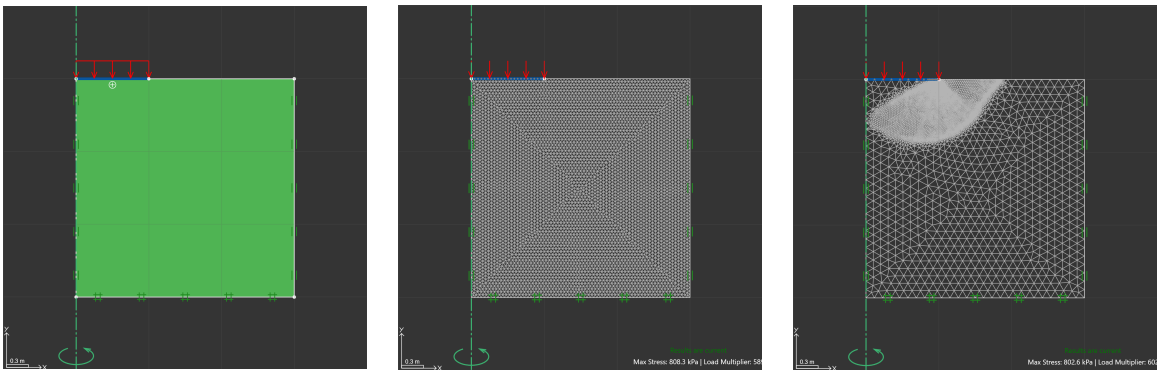

(a) Geometry (b) Regular meshing (c) adaptive meshing

Figure 5.7: Geometry and meshing of case 2

close to the exact solution. The figure also shows how the absolute relative error is decreasing with increasing the number of triangular elements.

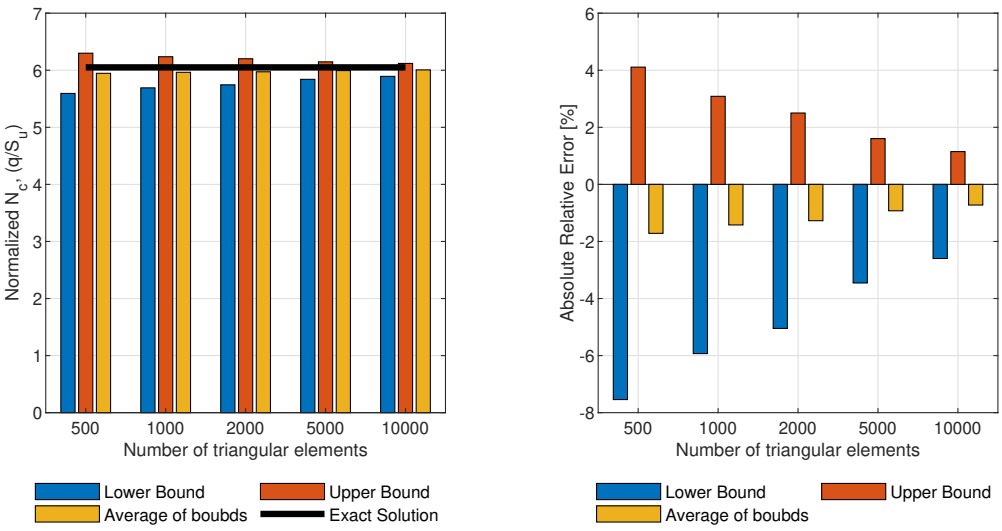


(a) Normalized ultimate load (b) Absolute relative error

Figure 5.8: Results for regular meshing (without adaptive meshing) for different number of triangular elements

#### 5.2.2.3 Results for meshing with adaptive meshing

Figure 5.9 shows the calculated bearing capacity factor for a different number of triangular elements with 3 iterative adaptive meshing. It can be seen than the solution is getting closer to 6.03, rather than 6.05. Furthermore, it can be seen that absolute relative error is significantly lower in comparison to regular meshing and the error reduces to a small amount by increasing the number of used elements.

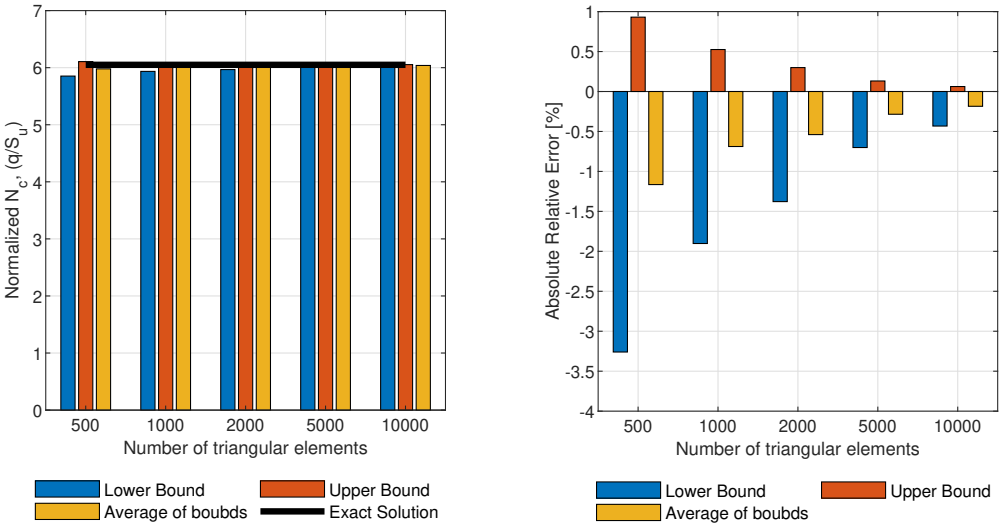


(a) Normalized ultimate load

(b) Absolute relative error

Figure 5.9: Results for case 2 with adaptive meshing for different number of triangular elements

#### 5.2.2.4 Comparison of results

Figure 5.10 shows how the average of lower and upper bounds changes by increasing the number of elements, for both regular meshing and adaptive meshing. Most importantly, the figure shows how the error is decreasing by increasing the number of elements. It also shows how the adaptive meshing is giving lower error than regular meshing for every number of elements.

### 5.2.3 Computation Results of *OptumG3* Runs

Bearing capacity of a circular foundation on a Tresca soil was analyzed using the three-dimensional version of Optum. Three types of meshing, namely lower, upper, and mixed, was used to run the analyses. The mixed element type is a mixture of lower and upper element types, so the average of bounds is the average of lower and upper bounds, while the mixed solution is going to be reported separately. As the two-dimensional problem, a total of 5 sets of analyses, with a different number of elements, was computed. As the problem is symmetrical, only $^1/_4$ of the problem was modeled.

#### 5.2.3.1 Geometry and Meshing

Figure 5.11 shows the geometry and meshing used for this case. A soil body with dimensions of $4 \times 4 \times 4$ ($B \times H \times L$) was used where a foundation with 1 m diameter and 1 m height is resting on the soil mass.

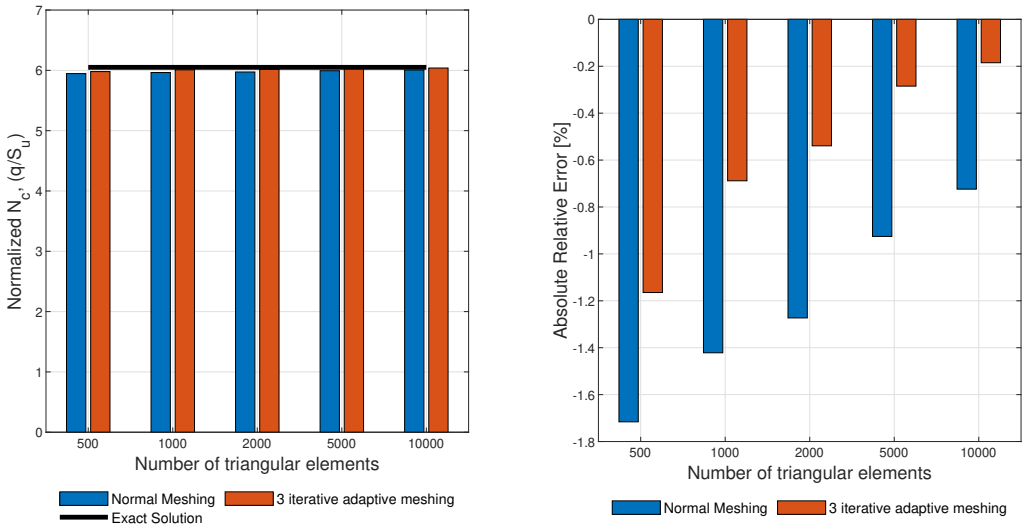


(a) Normalized ultimate load (b) Absolute relative error

Figure 5.10: Comparing the average of lower bound and upper bound between regular meshing and adaptive meshing

The figure also shows how 10.000 elements are distributed for regular meshing and adaptive meshing.

#### 5.2.3.2 Results for regular meshing

Figure 5.12 shows the results of the analyses for regular meshing with OptumG3 with a different number of elements. It can be seen that results are getting closer as the number of the elements increasing, but the precision of the simulation does not increase to the level of the 2D version.

#### 5.2.3.3 Results for meshing with adaptive meshing

Figure 5.13 shows the results of the analyses for the case where three iterations of adaptive meshing were used. The number of meshes was kept constant while through adaptive meshing their size and place would vary in the area with high shear dissipation.

It can be seen that by increasing the number of elements, results are getting closer to 6.08, rather than 6.05. The error of simulation is shown as well. Increasing the number of elements generally decreases the error, but it is not able to lower it to below 1%, as was seen in the 2D version.

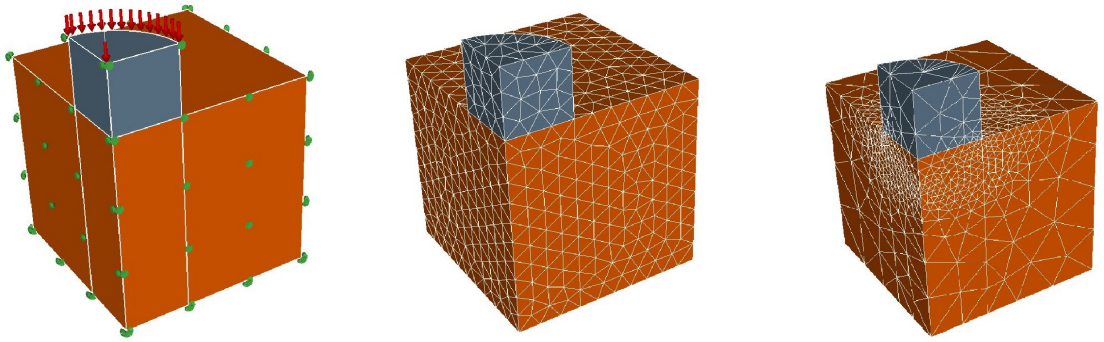

(a) Geometry (b) Regular meshing (c) Adaptive meshing

Figure 5.11: Geometry and meshing of case 1 (10.000 triangular elements)

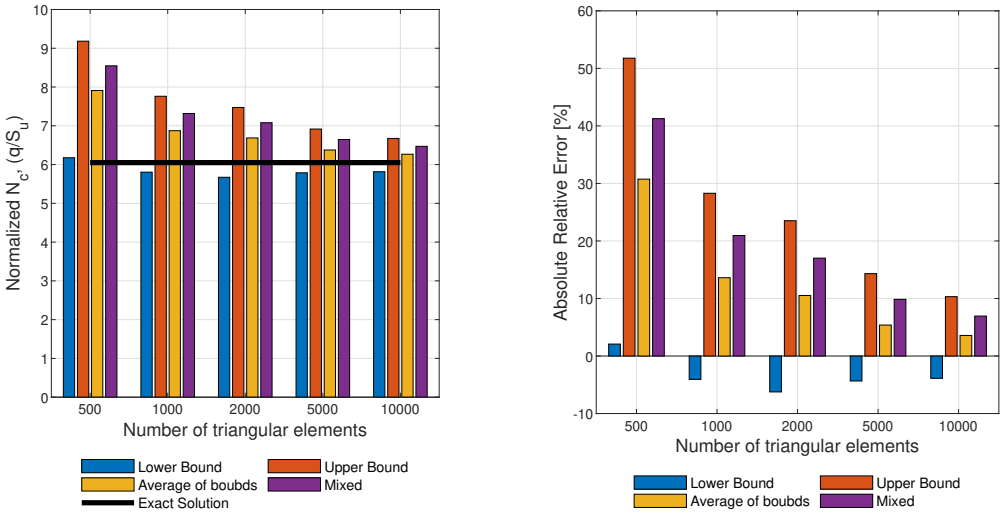


(a) Normalized ultimate load (b) Absolute relative error

Figure 5.12: Results for regular meshing for different number of triangular elements

### 5.2.4 Comparison of results

Figure 5.14 shows a comparison of the results obtained from 2D and 3D analyses with adaptive meshing. Average of lower and upper bound for both 2D and 3D versions, alongside results of mixed solutions from 3D analyses are reported.

It can be seen that the results of the 3D analyses are generally reporting higher bearing capacity than the exact solution while the 2D version is doing the opposite. Furthermore, for 3D results, the mixed solution is overestimating the bearing capacity in comparison to the average of lower and upper bounds.

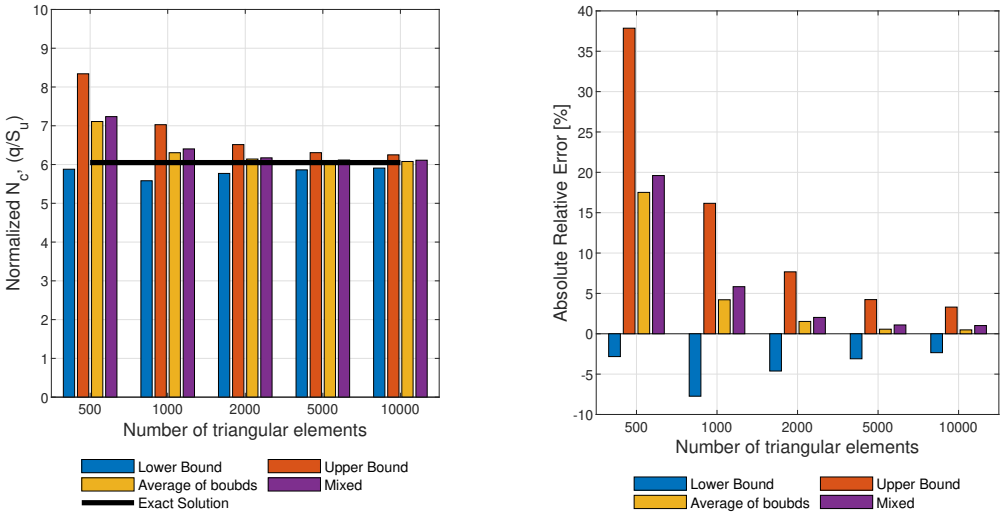


(a) Normalized ultimate load (b) Absolute relative error

Figure 5.13: Results of analyses with adaptive meshing for a different number of elements

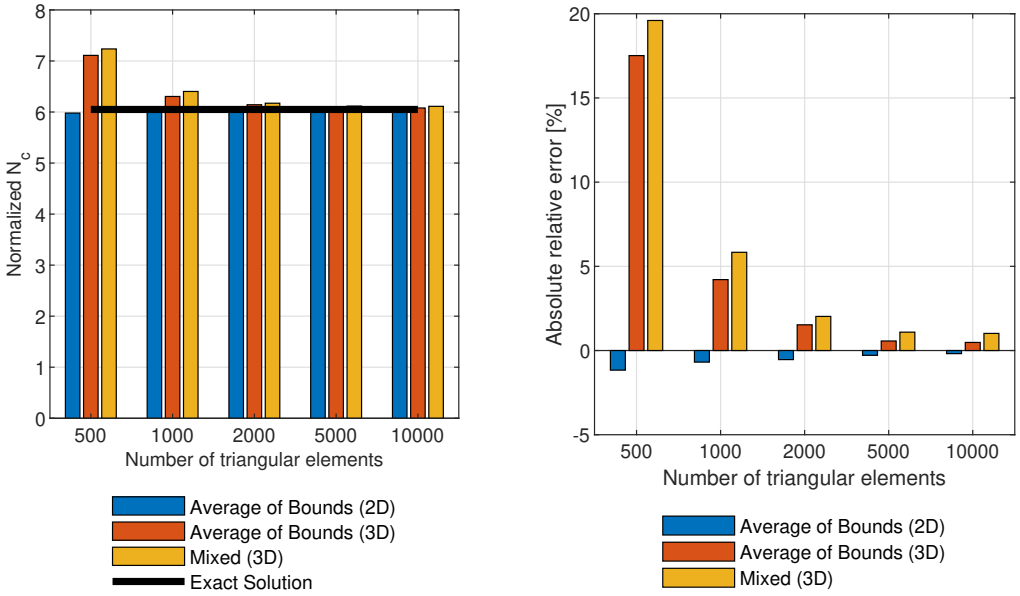


(a) Normalized ultimate load (b) Absolute relative error

Figure 5.14: Comparing the results between 2D and 3D analyses (adaptive meshing)

## 5.3 Case 3: Combined Horizontal and Vertical loading on Tresca Soil

In this case, the ultimate limit bearing capacity of Tresca soil with inclined loading and overburden pressure equal to p=20 kPa will be investigated.

### 5.3.1 Theoretical Solution

As explained in subsection 3.3, bearing capacity factor, $N_c$, can be calculated based on the roughness ratio. The exact solution for a combined horizontal and vertical loading is shown in Figure 5.15.

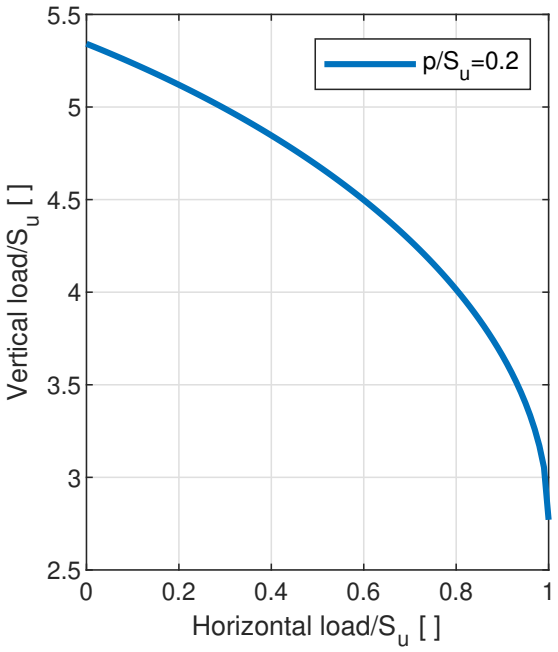


Figure 5.15: Exact solution for combined loading in Tresca Model (for p=20 kPa)

### 5.3.2 Computation Results of *OptumG2* Runs

In this case, two sets of computations, with and without adaptive meshing, were computed. Each set of analyzes is comprised of 96 single runs. Roughness ratio, ratio of horizontal stress to vertical stress, was increased incrementally from 0 to 0.95, with 0.01 increments and the result of each of these ratios are recorded.

#### 5.3.2.1 Geometry and Meshing

Figure 5.16 shows the geometry and meshing generated by the program. The meshing shown in the figure is the case with three iterative meshings. The soil body has an overburden pressure

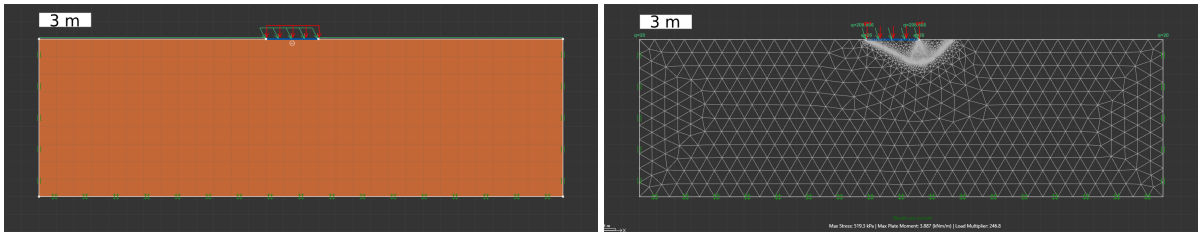


(a) Geometry (b) Meshing

Figure 5.16: Geometry and meshing of Case 3

equal to 20 kPa. Furthermore, the soil body has 30 m width, 9 m height and a footing 3 m in width is resting on it. 5.000 triangular elements were used for this case.

Figure 5.17 shows a comparison between the failure surface suggested by Janbu and the one suggested by the program. The agreement between the numerical results and the theoretical ones can be observed for r≤0.95. For ratios higher than this, the error of computation goes up, which can be due to of numerical difficulties.

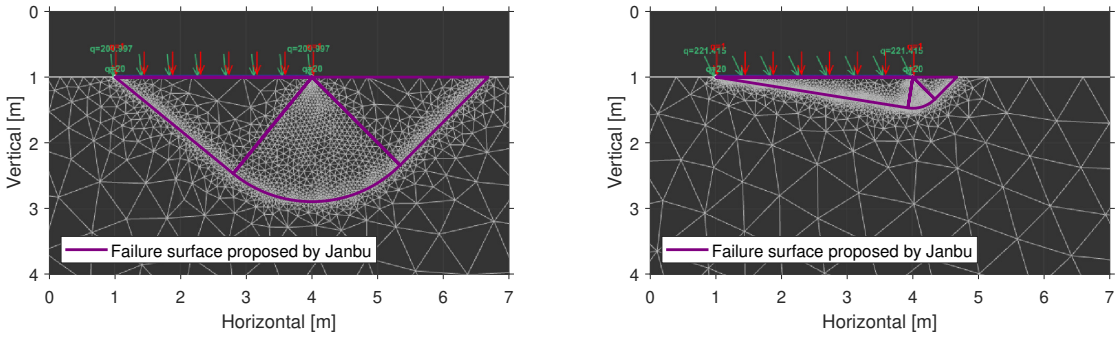


(a) r=0.2 (b) r=0.95

Figure 5.17: Comparison of failure envelope suggested by theoretical and numerical solutions

Furthermore, the figure shows how the failure envelope starts to incline to one side as the roughness ratio increases from zero to higher values.

#### 5.3.2.2 Results for regular meshing

Figure 5.18 shows the lower and upper bound results, and their average against the exact theoretical solution. The error of each of these bounds and their average is drawn as well.

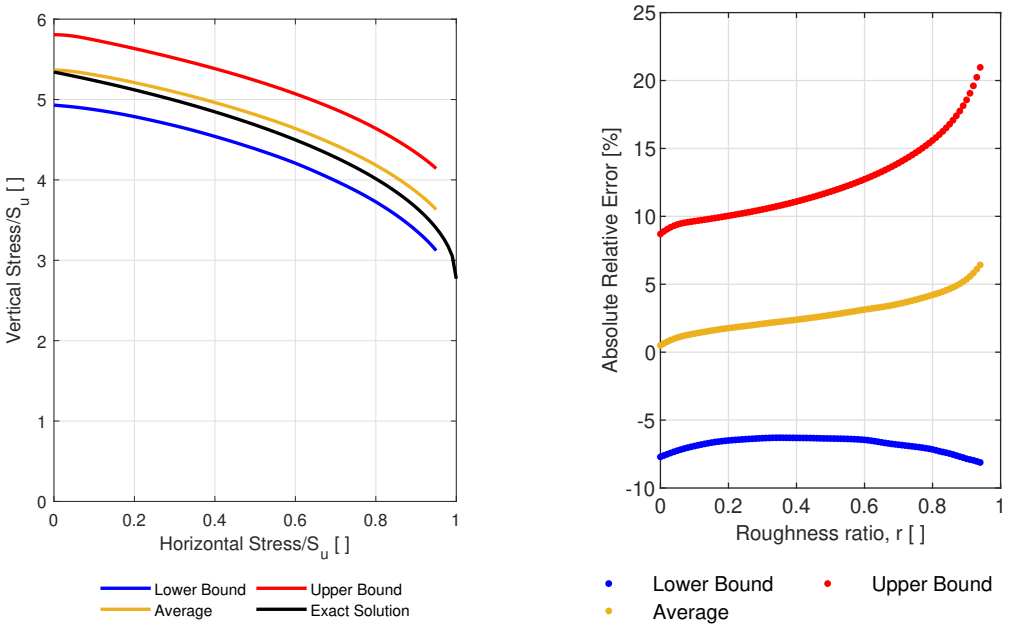


(a) Bearing Capacity

(b) Absolute Relative Error

Figure 5.18: Result of computations for meshing with 5000 triangular meshes

This set of runs show that regular meshing is overshooting and the results are higher than the exact solution.

#### 5.3.2.3 Results for meshing with adaptive meshing

In this set of runs, everything was the same except for the meshing type. This gives more precision to the simulation. Figure 5.19 shows the results of the simulations.

The absolute relative error is under 1%. This is an acceptable error and shows robustness, and accuracy, and precision of the solution/program.

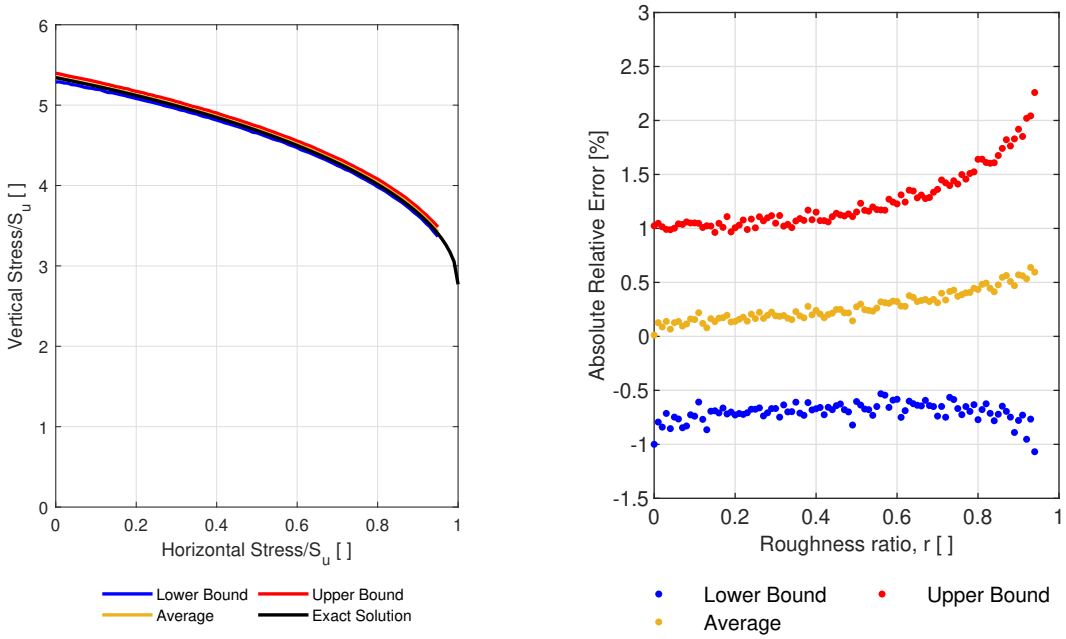


(a) Bearing Capacity

(b) Absolute Relative Error

Figure 5.19: Result of computations for adaptive meshing with 5000 triangles

## 5.4 Case 4: Vertical loading on Tresca soil with Embedment

In this case, the ultimate bearing capacity of Tresca soil with different embedments will be investigated. The soil is weightless to eliminate the surcharge effect.

### 5.4.1 Theoretical Solution

There is no rigorous solution for the effect of embedment on undrained analyses. There are however some solutions suggested by different authors. As mentioned in Section 2.2.3, Meyerhof [1951] suggested a linear depth factor for cohesion. The embedment factor suggested by Hansen [1970] is summarized in Section 3.1, which is simplified to the following formula for a special case (undrained case, $\varphi$=0):

$$\begin{aligned} 1 + 0.4 \cdot \frac{d}{B} \qquad & for \ \frac{d}{B} \leq 1 \\ 1 + 0.4 \cdot \arctan \frac{d}{B} \qquad & for \ \frac{d}{B} \geq 1 \end{aligned} \tag{5.3}$$

Gourvenec and Barnett [2011] has proposed the following relationship for a homogeneous soil:

$$d_c = 1 + 0.8890 \cdot \frac{d}{B} - 0.2194 \cdot \frac{d}{B} \tag{5.4}$$

None of these solutions are an exact solution, so there is no reference results that the simulation can be compared to.

### 5.4.2 Computational Results of OptumG2

For this case, upper and lower bound analyses with adaptive meshing and a fixed number of triangular elements (25.000) were used. The ratio of depth to width ($^D/_B$) was increased from 0 to 25 with 0.2 increments, totaling 126 pairs of analyses.

#### 5.4.2.1 Geometry and Meshing

Figure 5.20 shows the geometry of the problem. Soil body is 20 m wide and 9 m tall. There is a rigid foundation column which is 0.2 m wide and has varying height, which changes as the ratio of $^D/_B$ changes. There is a loading surface acting at the bottom of the foundation.

It was assumed no tension alongside vertical walls of the foundation to eliminate the effects of the friction between the wall and soil. Figure 5.20 also shows the meshing and failure line for $^D/_B$=25. It can be seen that the failure surface comes out to the soils surface in a semi-arc

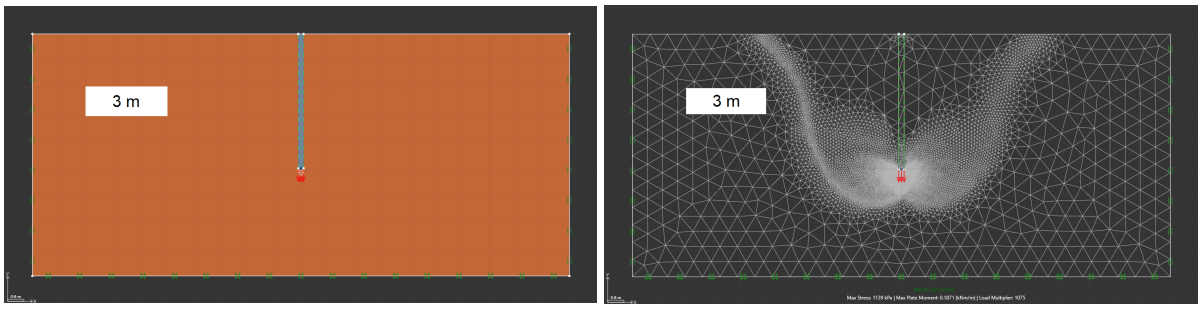


(a) geometry (b) Meshing

Figure 5.20: Geometry and meshing for Case 4 ($^{D}/_{B}$=25)

direction.

#### 5.4.2.2 Results for Adaptive Meshing

Figure 5.21 shows the results of the simulations. Results are shown as a normalized bearing capacity, which is the ultimate bearing capacity divided by undrained shear strength, $S_u$. Lower bound and upper bound numerical analyses are done by using the geometry described previously. The absolute relative error is the error calculated as mentioned in Section 4.3.2.

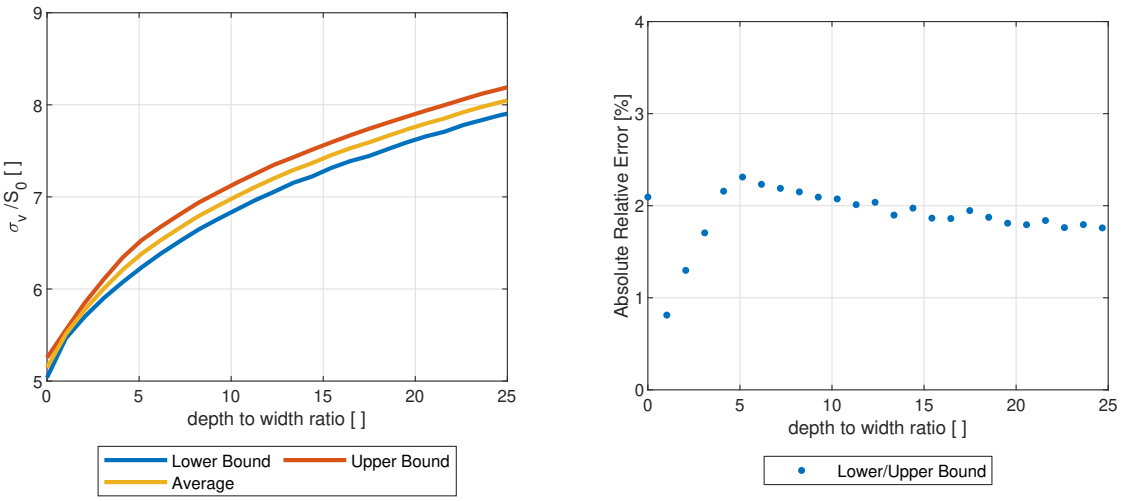


(a) Bearing capacity (b) Absolute Relative Error

Figure 5.21: Results of computation for adaptive meshing with 25.000 meshes

Based on the results of these simulations, a new formula is proposed for depth factor for $^{D}/_{B}$ in a range of $0 \leq {}^{D}/_{B} \leq 25$. The depth factor, $d_c$ is Incorporated in the bearing capacity formula as follows:

$$\sigma_v = d_c \cdot N_c \cdot S_u + p \tag{5.5}$$

The proposed formula for depth factor was found by using the Curve Fitting tool in MATLAB

by fitting the formula to the average of lower and upper bounds. The fitting has a coefficient of determination, R, equal to 0.9996, SSE equal to 0.0065, RMSE equal to 0.0057, and a maximum relative error of 0.1% compared to the average of bounds. The equation is as follows:

$$d_c = exp\left(\frac{0.3654 \cdot (D/B)^{1.224}}{D/B + 0.7743}\right) \tag{5.6}$$

The new formula corresponds well with simulation results and its relative position to lower and upper bounds, as shown in Figure 5.22. Results are plotted with dots and the figure shows how tightly packed the results are.

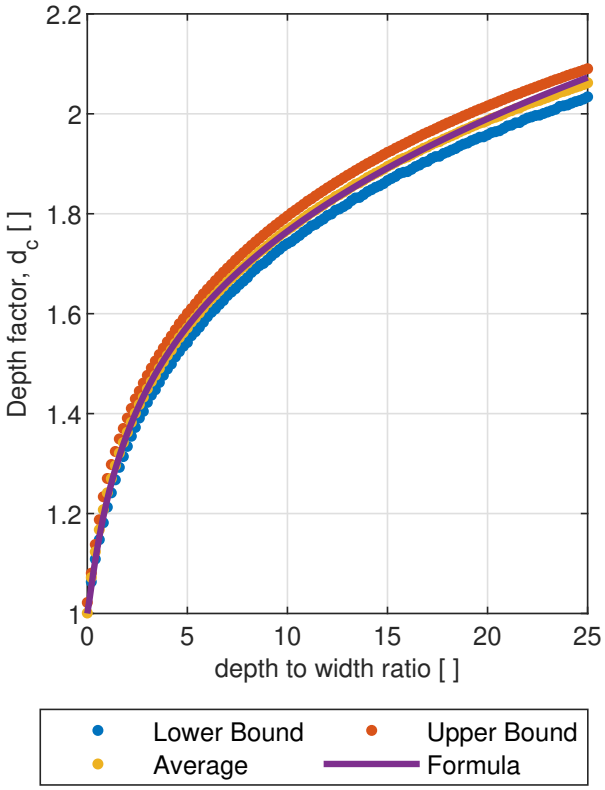


Figure 5.22: Proposed formula compared to Simulation of results

Figure 5.23 displays a comparison of this formula and previous methods, namely formulas suggested by Meyerhof [1951], Hansen [1970], and Gourvenec and Barnett [2011].

The figure shows the incapability of the previous works with the lower and upper bound solution and their considerable difference. The formula suggested by Meyerhof [1951] gives the worst results and the other formulas are underestimating for some depth to width ratio and overestimating for some others. Underestimating is not in itself a bad thing since this factor increases the ultimate bearing capacity, the problem, of course, is in overestimating which causes reporting more bearing capacity than what the soil can actually tolerate.

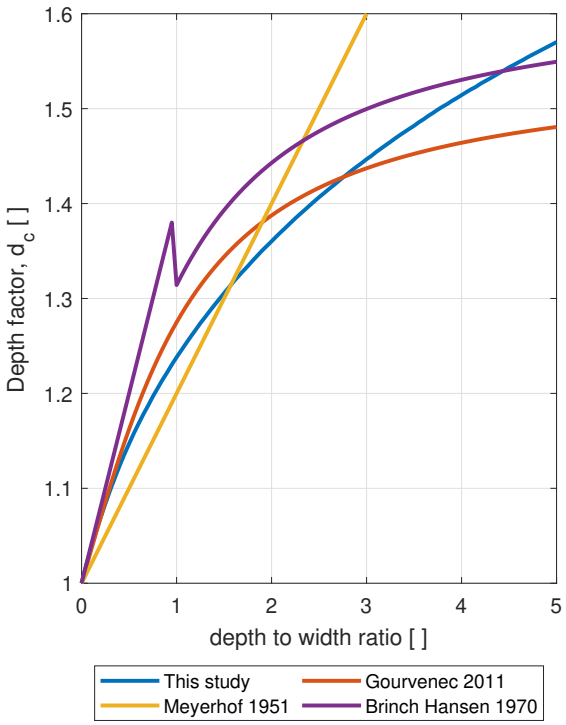


Figure 5.23: Comparison of proposed formula and previous works

## 5.5 Case 5: Vertical loading on Tresca soil with different footing shape

In this case, ultimate bearing capacity of rectangular foundations on Tresca soil will be investigated.

### 5.5.1 Theoretical Solution

There is no rigorous lower and upper bound solution for the effect of footing shape on undrained soil. Several authors have suggested the following formula for shape factor in undrained soils:

$$s_c = 1 + F \cdot \frac{B}{L} \tag{5.7}$$

Meyerhof [1963] and Grande et al. [2016] has suggested F=0.2 and Vesić [1973] and Hansen [1961] have suggested $F = \frac{1}{N_c}$. Gourvenec et al. [2006] has suggested the following formula based on results of finite element analyses:

$$s_c = 1 + 0.214 \cdot \frac{B}{L} - 0.067 \cdot \frac{B}{L}^2 \tag{5.8}$$

### 5.5.2 Computational Results of OptumG3

In this case, three types of meshes, namely lower, upper, and mixed, were used in the 3D version of Optum to run the analyses. Foundation width (B) to length (L) ratio, from here on $\frac{B}{L}$, was increased incrementally from 1 to 10, with 0.5 increments, totaling to 21 analyses. $^1/_4$ of the problem was modeled for reducing computation cost/time.

#### 5.5.2.1 Geometry and Meshing

Figure 5.24 shows the geometry and meshing used for this case. A soil body with dimensions of 6×15×5 (B×L×H) was used where a 1 m tall foundation with 1 m width and varying length, changing as the ratio of $\frac{B}{L}$ changes, is resting on the soil mass. The figure also shows the meshing used for this case ($\frac{B}{L}$=1). Adaptive meshing with a start number of elements equal to 10.000 building up to 25.000 with 3 iterative adaptive meshing was used.

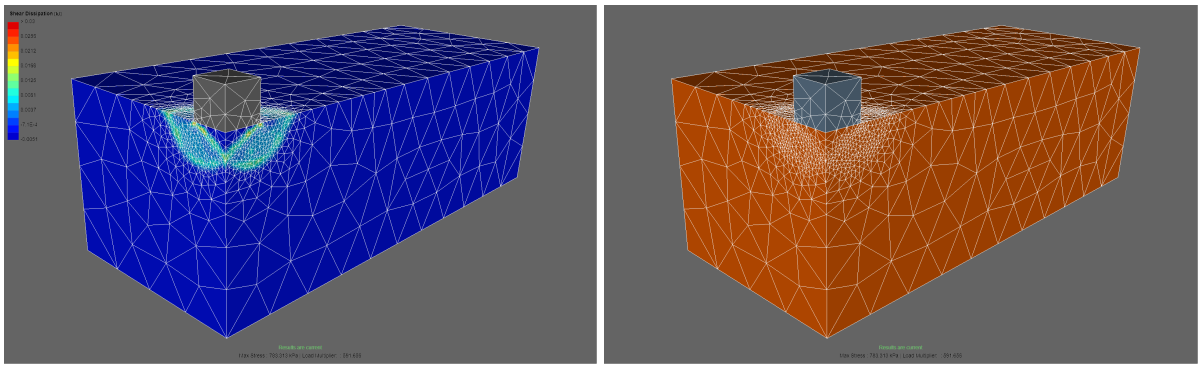

(a) Geometry (b) Meshing

Figure 5.24: Geometry and meshing for Case 5 ($\frac{B}{L}$=1)

#### 5.5.2.2 Results for Adaptive Meshing

Figure 5.25 shows the results of the simulation for different shape ratios. The average of the lower and upper bounds is also depicted alongside the results of mixed meshing. As can be seen, the mixed mesh gives quite similar results to the average of two bounds. The absolute relative error is somewhat higher than before, and this is mainly because of the complexity of 3D analyses. A new formula is suggested to represent the effect of the foundation shape ratios.

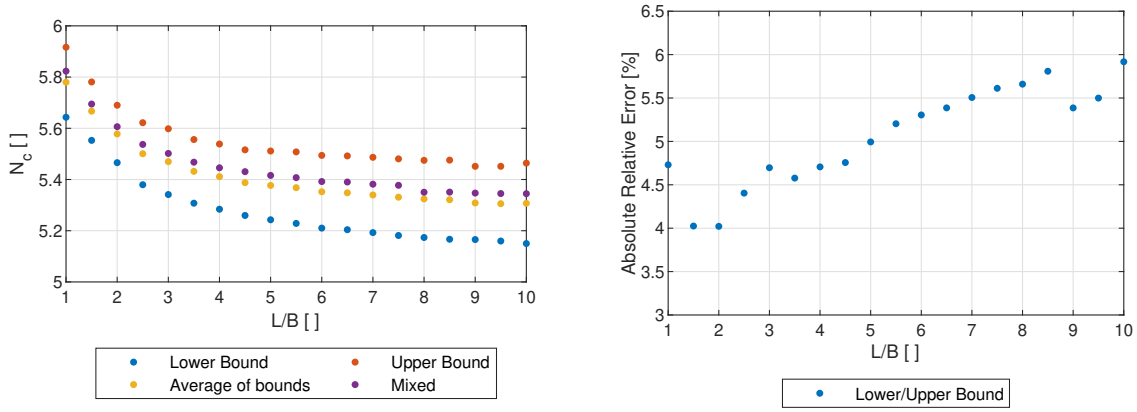


(a) Geometry (b) Meshing

Figure 5.25: Results of simulation for case 5

The formula is correlated to the average of two bounds. The correlation has an R of 0.9961, SSE of $4.5 \cdot 10^{-5}$ and RMSE of 0.0016. The formula is as follows:

$$s_c = 1 + 0.1262 \cdot \frac{L}{B}^{-0.6165} \tag{5.9}$$

For rectangular shaped foundations, the bearing capacity can be given as follows:

$$\sigma_v = s_c \cdot N_c \cdot S_u + q \tag{5.10}$$

The formula matches well with the results, as can be seen in Figure 5.26.

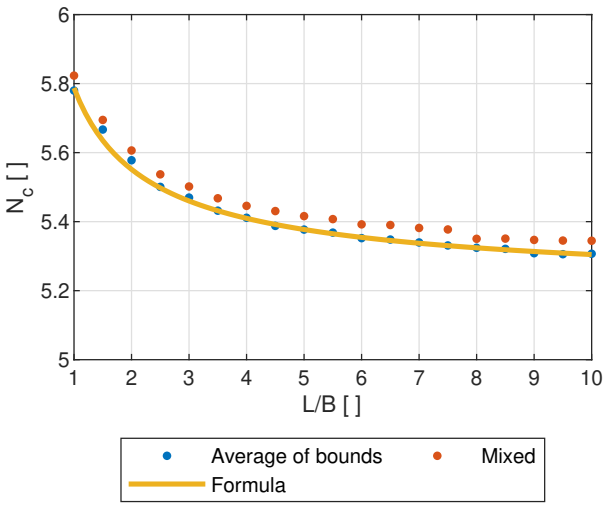


Figure 5.26: Geometry and meshing for Case 5 ($\frac{B}{L}$=1)

Figure 5.27 shows a comparison of previously proposed formulas, mentioned in the theoretical solution, and the proposed formula in this thesis.

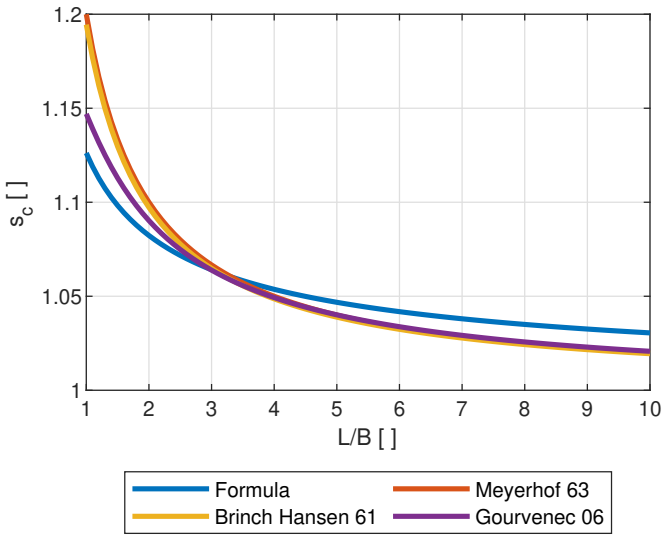


Figure 5.27: Comparison of proposed relation and other authors

It can be seen that the other relations for $s_c$ are overestimating the factor for lower ratios and underestimating it for larger ratios.

## 5.6 Case 6 : Inclined loading on Tresca soil with different footing shape

In this case, the ultimate bearing capacity of rectangular foundations with an inclined load on Tresca soil will be investigated.

### 5.6.1 Theoretical Solution

There is no rigorous theoretical solution proposed for inclined loading on a rectangular foundation. Grande et al. [2016] suggest the following formula for the inclined loading of square foundations:

$$N_{c,\ square} = (1 + 0.2 \cdot (1 - r)) \cdot N_c \tag{5.11}$$

where the $N_c$ is following the equation given in Section 3.3. This shape factor was shown in the previous case to overestimate the shape effect for lower L/B factor and underestimate for higher ratios.

### 5.6.2 Computational Results of OptumG3

For this case, inclined loading of a foundation with 5 different L/B ratios was analyzed using lower, upper, and mixed meshing type. Inclined loading on a foundation with L/B ratio equal to 1, 2, 3, 4, and 10 was analyzed, where the load inclination angle (V/H ratio) was increased incrementally from vertical (0°) to 20° degrees with 1° increment.

#### 5.6.2.1 Geometry and Meshing

Figure 5.28 shows the geometry and meshing for a special ratio of $^{L}/_{B}$=4. Besides, the figure shows how the elements are denser around the failure line, which is depicted by the shear dissipation counters. Soil body has a dimension of $7 \times 7 \times 5$ (B×L×H). The foundation element, which was resting in the middle, was varying for different L/B ratios. Adaptive meshing with a start element of 10.000 building up to 25.000 with three iterative adaptive meshings were used for analyses.

#### 5.6.2.2 Results for Adaptive Meshing

Figure 5.29 shows the results of simulations for the mentioned L/B ratios. The figure shows the results of three types of meshing, in addition to the average of the lower and upper bound.

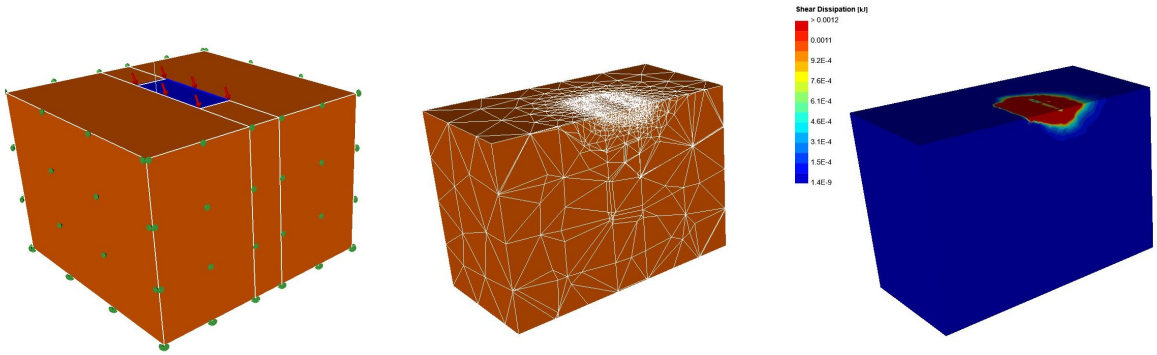


(a) Geometry (b) Meshing (c) Shear dissipation

Figure 5.28: Geometry and meshing for $^{L}/_{B}$=4 and inclined load of $^{H}/_{V}$=tan(16°) (25.000 triangular elements)

Plane strain $N_c$ is plotted as a reference. The figure also shows the absolute relative error of the analyses, which is varying between 0 to 12%. As mentioned in the previous case, the error does not drop to a very small amount as it does for two-dimensional analyses.

In the previous case, Equation 5.9 was proposed to represent the shape factor for rectangular foundations under vertical loading. This formula should be able to be combined with the $N_c$ formula proposed by Grande et al. [2016]. This combination is resulting in slightly conservative value predictions, as can be seen in Figure 5.30. The idea is to extend the Equation 5.9, in a way to include the effect of inclination of the load. The new equation is extended to the following:

$$s_c = \left(1 + 0.1262 \cdot \frac{L}{B}^{-0.6165}\right) \cdot \left[1.0 \cdot \exp\left(0.1 \cdot r\right) + 0.0001 \cdot \exp\left(6.5 \cdot r\right)\right] \tag{5.12}$$

This formula is able to show a better correlation with the average of lower and upper bounds. The correlation for different $^{L}/_{B}$ ratios can be seen in Figure 5.31.

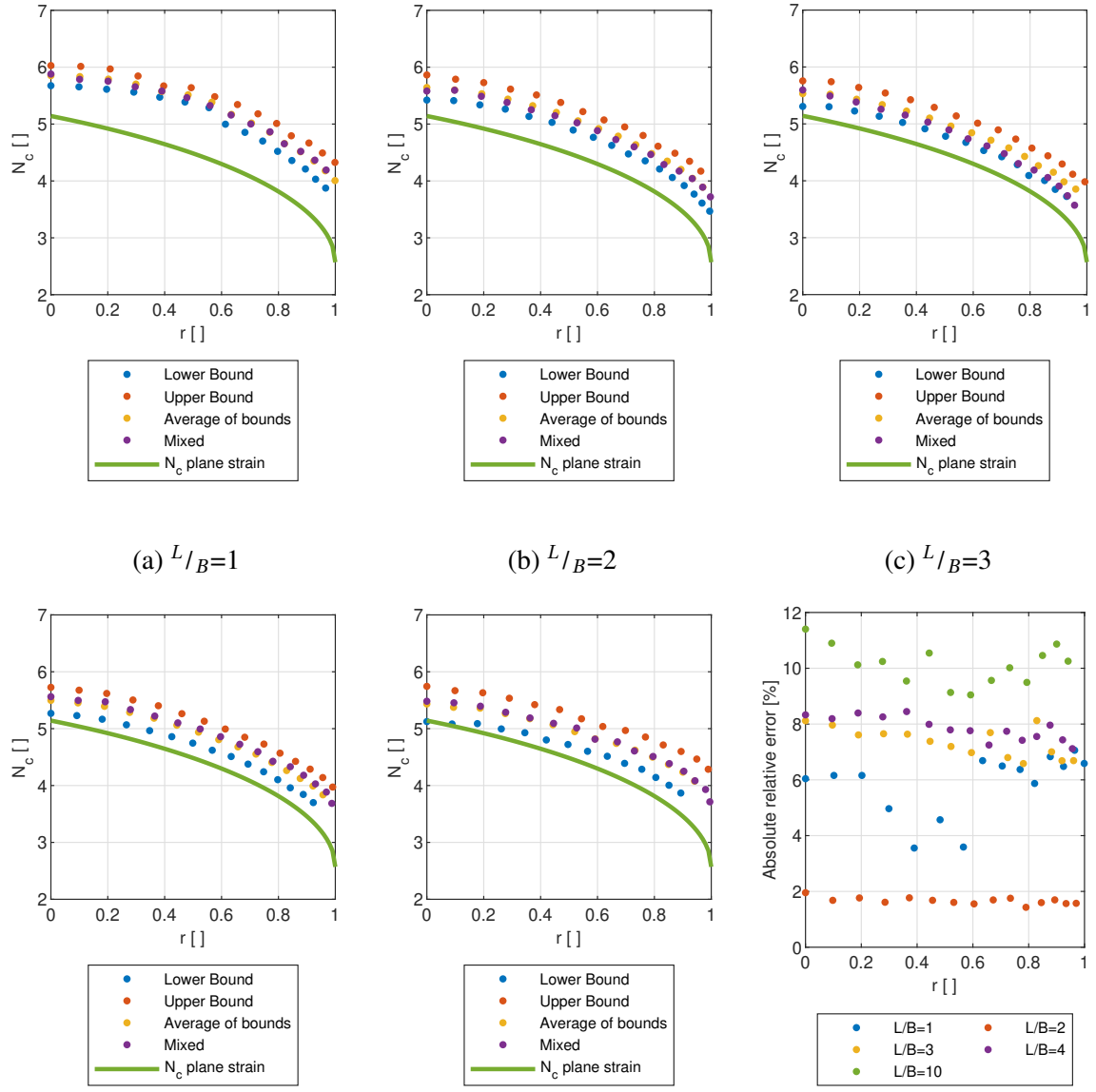


(a) $^{L}/_{B}$=1 (b) $^{L}/_{B}$=2 (c) $^{L}/_{B}$=3

(d) $^{L}/_{B}$=4 (e) $^{L}/_{B}$=10 (f) Absolute relative error

Figure 5.29: Results of analyses for case 6

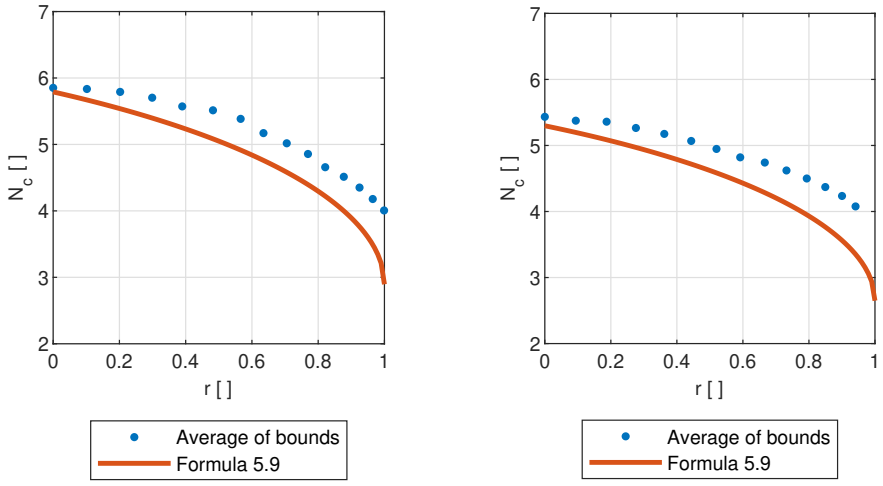


(a) $^{L}/_{B}$=1 (b) $^{L}/_{B}$=10

Figure 5.30: Comparison of average of lower and upper bounds of inclined loading with combination of $N_c$ formula and Equation 5.9

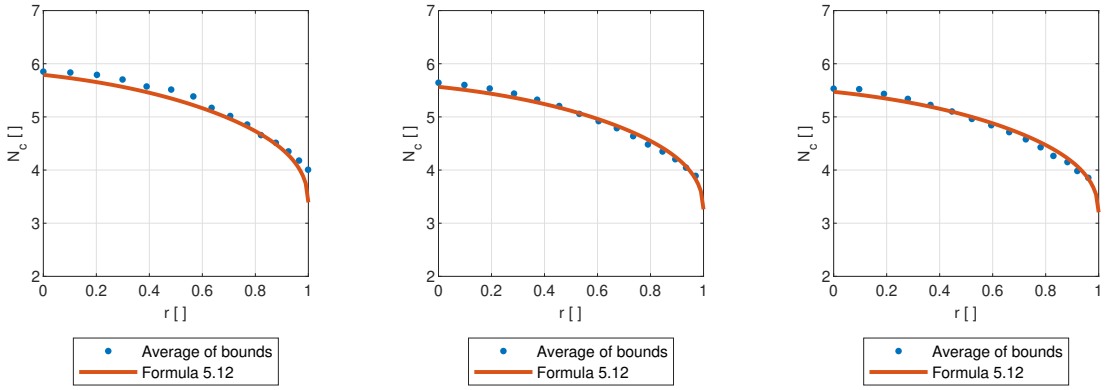


(a) $^{L}/_{B}$=1 (b) $^{L}/_{B}$=2 (c) $^{L}/_{B}$=3

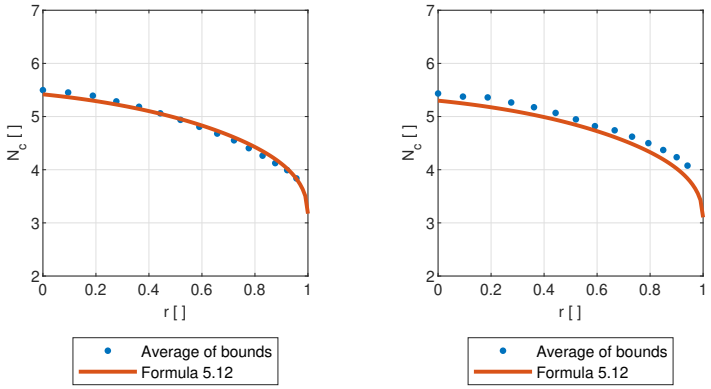


(d) $^{L}/_{B}$=4 (e) $^{L}/_{B}$=10

Figure 5.31: Comparison of average of lower and upper bounds of inclined loading with combination of $N_c$ formula and Equation 5.12

## 5.7 case 7: Vertical loading on Tresca soil with increasing Strength

In this case, the ultimate bearing capacity of Tresca soil with linearly increasing strength with depth will be investigated.

### 5.7.1 Proposed Solution by other authors

By using the theory of plasticity, Davis and Booker [1973] have developed lower and upper bound solutions for bearing capacity of a foundation with geometry and shear strength heterogeneity shown in Figure 5.32.

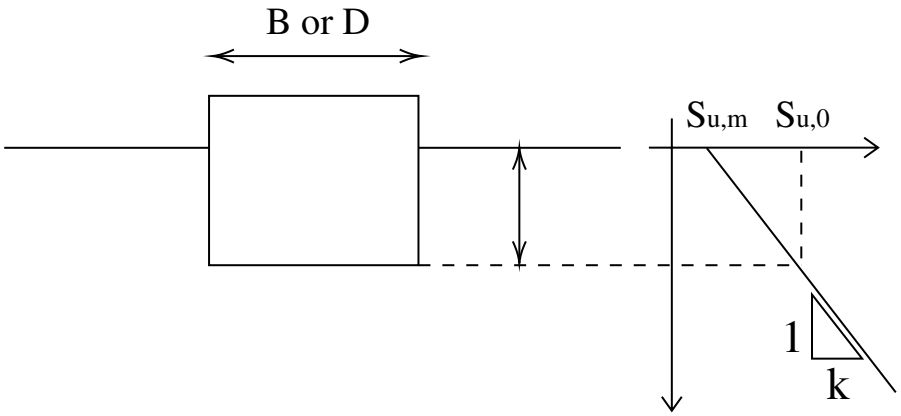


Figure 5.32: Variation of shear strength with depth (redrawn from Davis and Booker [1973])

The proposed formula is as follows:

$$\sigma_v = F \cdot \left( N_c \cdot S_{u,0} + \frac{k \cdot B}{4} \cdot S_{u,0} \right) \tag{5.13}$$

where $F$ is the correction factor, which is depicted in Figure 5.33 for rough footing, called $F_s$, and for smooth footing, $F_r$.

### 5.7.2 Computational Results of OptumG2

For this case, lower and upper bound analyses with adaptive meshing were used. A dimensionless ratio, $\kappa$ is used to show the strength heterogeneity, which is described as follows:

$$\kappa = \frac{k \cdot B}{S_{u,0}} \tag{5.14}$$

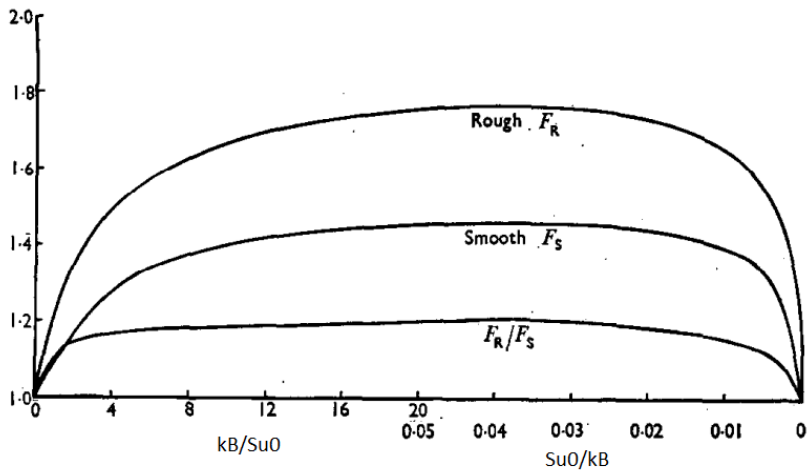


Figure 5.33: Correction factor for smooth footing, $F_s$, and rough footing, $F_r$ (Davis and Booker [1973])

$\kappa$ was increased incrementally from 0 to 20, with 0.1 increments. $\kappa$ would not increase to such a large value in practice, but larger ratios were examined on a theoretical basis, to get a curve to compare to the Davis and Booker [1973] work.

#### 5.7.2.1 Geometry and Meshing

Figure 5.34 shows the geometry of the problem. Soil body has 10 m width and 4 m height. There is a 1m wide rigid shell foundation resting on the top of the foundation. A start mesh equal to 10.000 building up to 25.000 was used in this case. Meshing for a case of $\frac{k \cdot B}{S_u}$)=5 is shown.

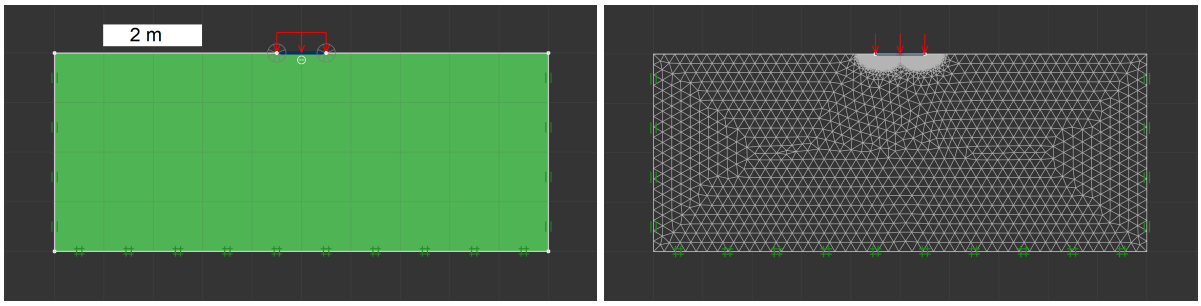


(a) Geometry (b) Meshing

Figure 5.34: Geometry and meshing for case 7

#### 5.7.2.2 Results for Adaptive Meshing

Figure 5.35 shows the results of the simulations. Lower and upper bound numerical analyses are computed as well as the average of two bounds. Furthermore, the absolute relative error is shown to illustrate robustness of the analyses. Based on the results of these simulations, a

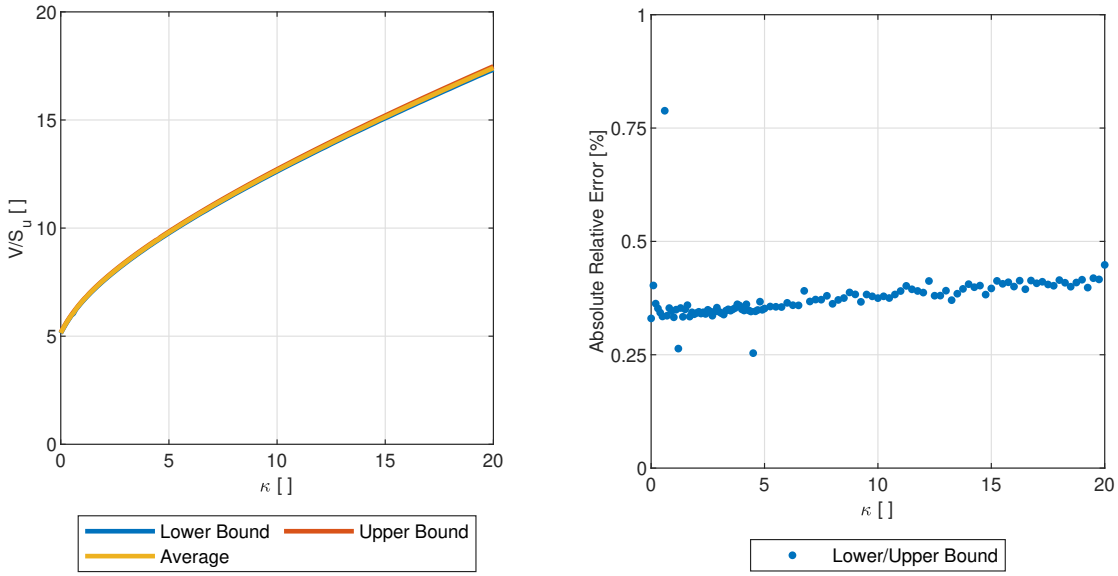


(a) Normalized bearing capacity

(b) Absolute Relative Error

Figure 5.35: Results of computations for 3 iterative adaptive meshing

formula can be proposed for $F_R$ for varying $\kappa$ ratios. This formula will be compatible with how Davis and Booker [1973] have formulated their equation (see Equation 5.13). By using Equation 5.13, an equation for $F_R$ is proposed. The proposed formula is:

$$F_R = \frac{1239 \cdot \kappa + 2181}{\kappa^2 + 655.5 \cdot \kappa + 2147} \tag{5.15}$$

The fitting has an adjusted coefficient of determination, R equal to 0.9996; error sum of squares, SSE equal to 0.0014, and root mean square error, RMSE, equal to 0.0036. Figure 5.36 shows how the proposed equation compares to the computation results. Figure 5.37 shows a comparison between the proposed equation, Equation 4.11, and the $F_R$ suggested by Davis and Booker [1973]. There is a good correlation between theses two correlation factors up til $\kappa$ ratios of 8. After that, the correlation factor proposed by Davis and Booker [1973] is overestimating the factor.

### 5.7.3 Computation Results for inclined loading

As stated in Equation 5.13, the ultimate bearing capacity is proposed as a function of $N_c$, which in itself is a function of the roughness ratio. In this part, it was intended to see behavior of soil under an inclined load on a soil with linearly increasing strength with depth. Geometry and meshing are as before. $\kappa$ was increased incrementally from 0 to 5, with 0.1 increments for two roughness ratios, r=0.2 and r=0.4. As before, both lower and upper bound was run to get a correct picture of the problem.

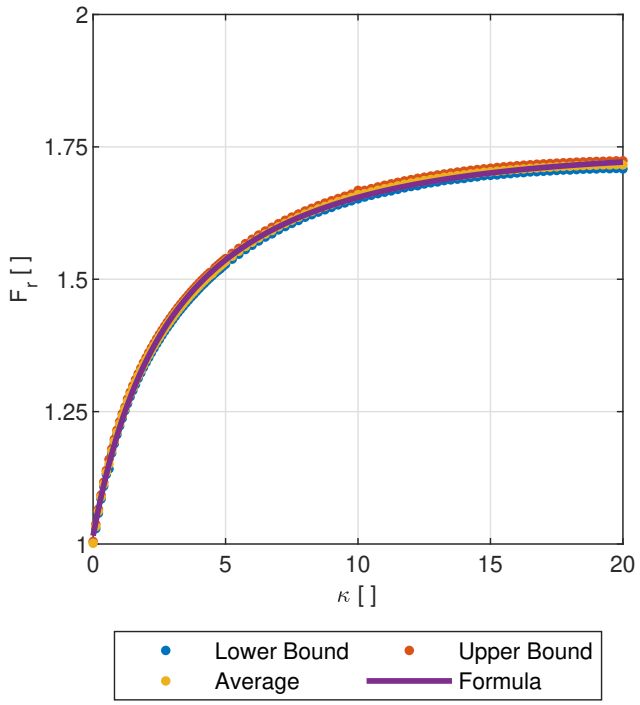


Figure 5.36: Proposed formula compared to the simulation results

#### 5.7.3.1 Results of simulations

Figure 5.38 shows the results of the lower and upper bound analyses for the mentioned roughness ratios. Besides, it shows how Equation 5.13, combined with the suggested correlation factor in Equation 5.15, compares to the simulation results (named $F_r$ *formula* in the legend). As can be seen, the formula is slightly overestimating for roughness ratio of 0.2, but it is clearly over the upper bound solution for roughness ration of 0.4. This is most probably because of how Davis and Booker [1973] have set up their equations, where $N_c$, which is a function of roughness is summed with $\frac{k}{4}$ and then multiplied with $F_R$. This means that $N_c$ is being added with something which is not a function of roughness ratio. As the roughness ratio varies, the $N_c$ changes accordingly, but not $\frac{k}{4}$. The Equation 5.13 combined with Equation 5.15 is a good predictor for vertical loads, but the following set up is a better solution for inclined loading, where the bearing capacity can be defined as:

$$\sigma_v = F'_R \cdot N_c \cdot S_{u,0} \tag{5.16}$$

where $F'_R$ is defined as:

$$F'_R = 1 - 0.719 \cdot \kappa^{1.021} + \kappa^{0.9506} \tag{5.17}$$

This formula can be seen in Figure 5.38 ($F'_r$ *formula* in the legend). It can be seen that it has a better correlation with the simulation results.

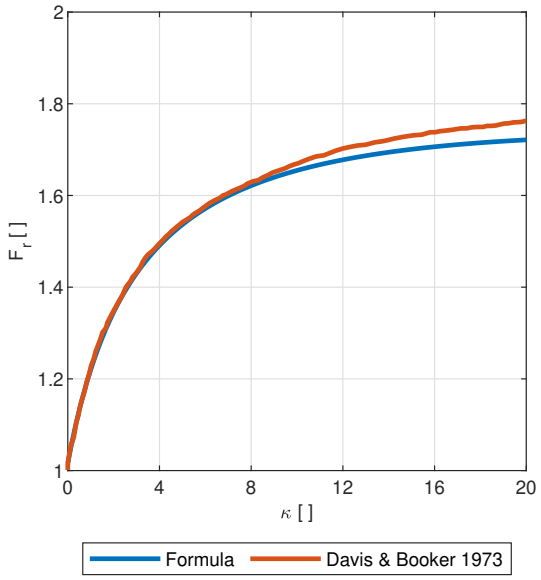


Figure 5.37: Proposed formula compared to the $F_R$ proposed by Davis and Booker [1973]

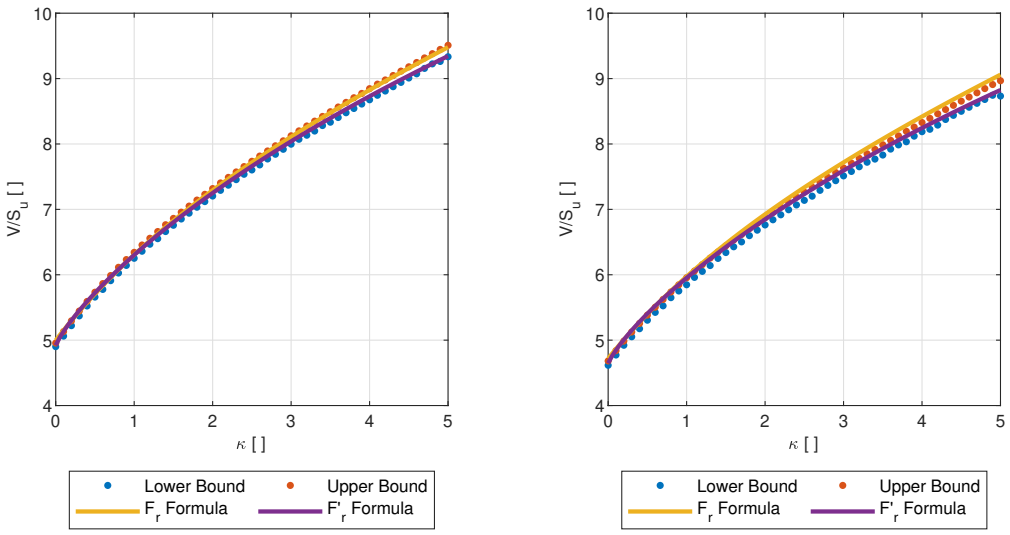


(a) r=0.2 (b) r=0.4

Figure 5.38: Comparison of proposed formula to the results of computation of inclined loading on the soil with increasing strength with depth

## 5.8 Case 8: Combined HMV loading on Tresca soil (full tension)

In this case, the ultimate bearing capacity of Tresca soil with combined horizontal, vertical and moment loading will be investigated. It will be assumed full shear strength under the planar surface, which is the situation for a foundation with suction beneath the foundation. This can be the case for a skirted foundation.

### 5.8.1 Theoretical Solution

There is no rigorous solution for this type of loading, however, there are some solutions proposed by different authors, as some of the solutions mentioned by Randolph and Gourvenec [2011].

Case 3 was a specific example of this case, where the moment was zero. By adding moment as a third axis, a comprehensive failure surface can be found. For this case, soil can fail under any type of combination of horizontal, vertical, and moment loading. The idea is to find a failure surface that can represent this 3D surface.

### 5.8.2 Computational Results

Loading of a shallow foundation with horizontal, vertical, and moment components will result in complex stress paths and changes in the soil. Interaction of these three components, horizontal, vertical, and moment loading components has to be taken to account explicitly, rather than using factors. Sign convention shown in Figure 5.39 is assumed in this case.

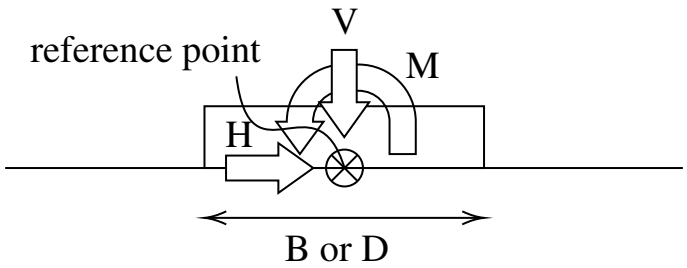


Figure 5.39: A conventional loading for a shallow foundation (redrawn from Randolph and Gourvenec [2011])

The analyses were run in a way to represent the failure surface which is composed of vertical, horizontal, and moment loads using the 2D version of the program. By keeping one of these loads, namely vertical, horizontal, and moment, at a constant level, analyses were done

by changing the other two loads. This creates a sort of a cross-section which cuts through each of these three axes. Then several unique loading paths were run to get a picture of the failure surface of each cross-section. This leads to three types of cross-sections, namely H-M, M-V, and H-V. Table 5.1 shows an overview of the cross-sections which passes through axes. Each of these are on a fixed ratio of that load to maximum allowed load.

Table 5.1: Analysis types run with Optum

| cross-sections through H, M and V axis | | | | | | |
|---|---|---|---|---|---|---|
| $H/H_{ult}$ | 0 | 0.25 | 0.5 | 0.75 | 0.9 | 0.95 |
| $M/M_{ult}$ | 0 | 0.25 | 0.5 | 0.75 | 0.9 | 0.95 |
| $V/V_{ult}$ | 0 | 0.25 | 0.5 | 0.75 | 0.9 | 0.95 |

It is assumed that $M_{ult}$ is 0.69 times $S_u$. The exact multiplier is slightly higher, but whenever the term $M_{ult}$ is used, it means $0.69 \cdot S_u$.

#### 5.8.2.1 Geometry and Meshing

Figure 5.40 shows the geometry and meshing of the problem. Soil body is 10 m wide and 4 m tall. There is a rigid shell element with 1 m width resting on top of the soil mass. There is a constant load acting over the whole shell and a multiplier load is acting with varying inclination on the center of the shell. The figure shows a special case of the loading path, where $H/H_{ult}$=25% and $^{M}/_{V}$=$\sqrt{3}$.

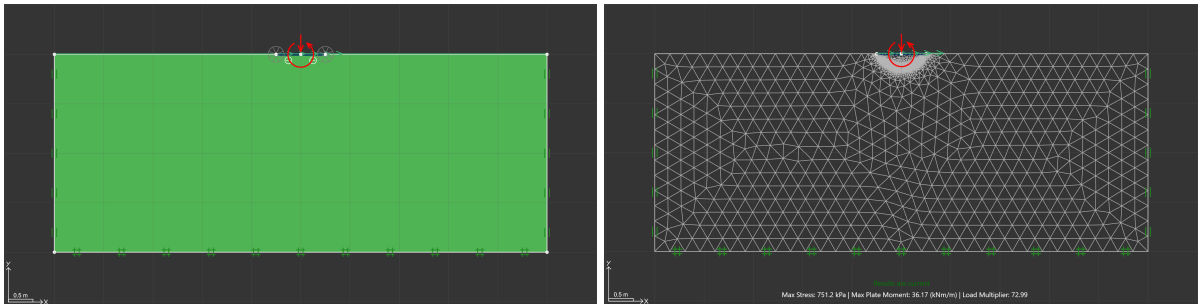

(a) Geometry (b) Meshing

Figure 5.40: Geometry and meshing for a specific loading path ($H/H_{ult}$=25%, $^{M}/_{V}$=$\sqrt{3}$)

For this case, lower and upper bound analyses with adaptive meshing were run with OptumG2. Meshing for this case was generated with a start number of elements equal to 5.000 and building up to 25.000 through 3 adaptive iterations. A total of 181 pair of loading were done for each cross-section.

#### 5.8.2.2 Results for Adaptive Meshing

As stated in Table 5.1, three types of cross-sections across failure surfaces were drawn, where while one of three loading types (vertical loading, horizontal loading and moment) is being fixed, the other two were changed to get different loading paths, hereby called H-M, M-V, and H-V spaces. The results of lower and upper bound analyses for H-M, M-V, and H-V spaces are shown in Figure 5.41, Figure 5.42 and Figure 5.43, subsequently. Error of computation are not depicted here, but it is varying from 1% to 7%.

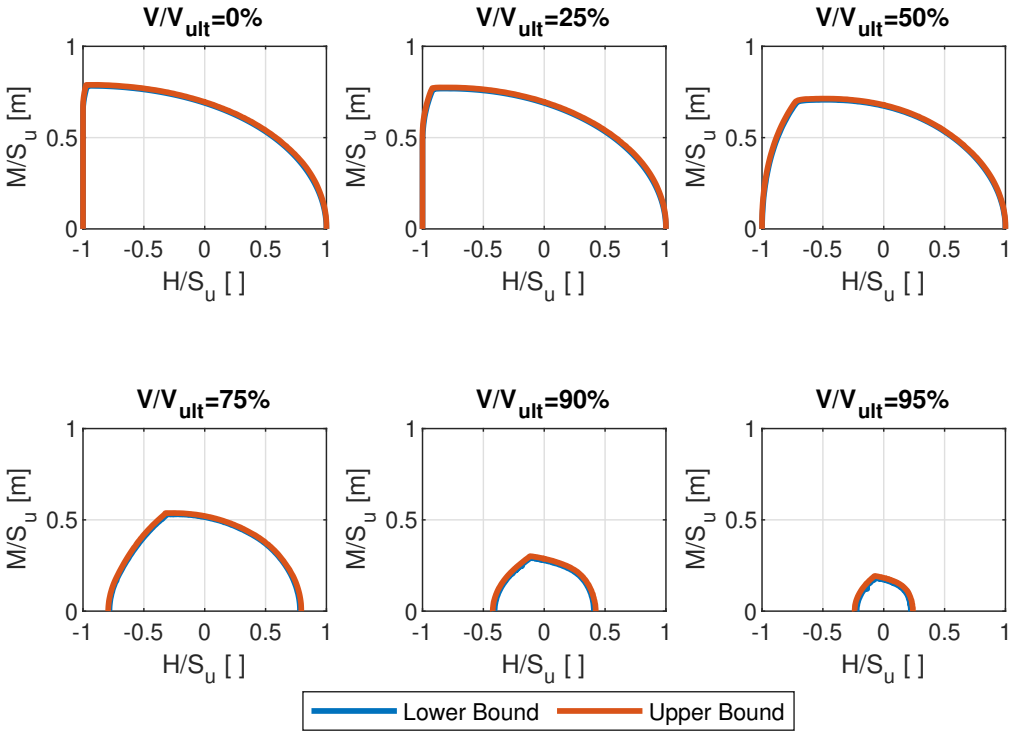


Figure 5.41: Results of lower and upper bound analyses for H-M space

It can be observed that when signs of the moment and horizontal loading are not the same, they are working against each other and the soil mass is able to take higher values of the moment and/or horizontal load than the situation where their signs are the same. This can be seen clearly in Figure 5.41. The failure line grows outward when the signs are not the same.

In H-M space, it can be seen how the maximum moment increases as the horizontal load is a counteracting moment, which means increasing moment capacity. This can be very clearly seen in low $V/V_{ult}$ ratios and the effect of horizontal stress dampens as this ratio increases.

In H-V space, as the moment is increasing, horizontal stress in which the foundation would slide across the soil surface (sliding failure) is decreasing. It can be seen that the failure line when $M/M_{ult}$=25% is relatively similar in shape to case with no moment. Increasing of moment consequently decreases the vertical loading capacity as well. On the other side of the

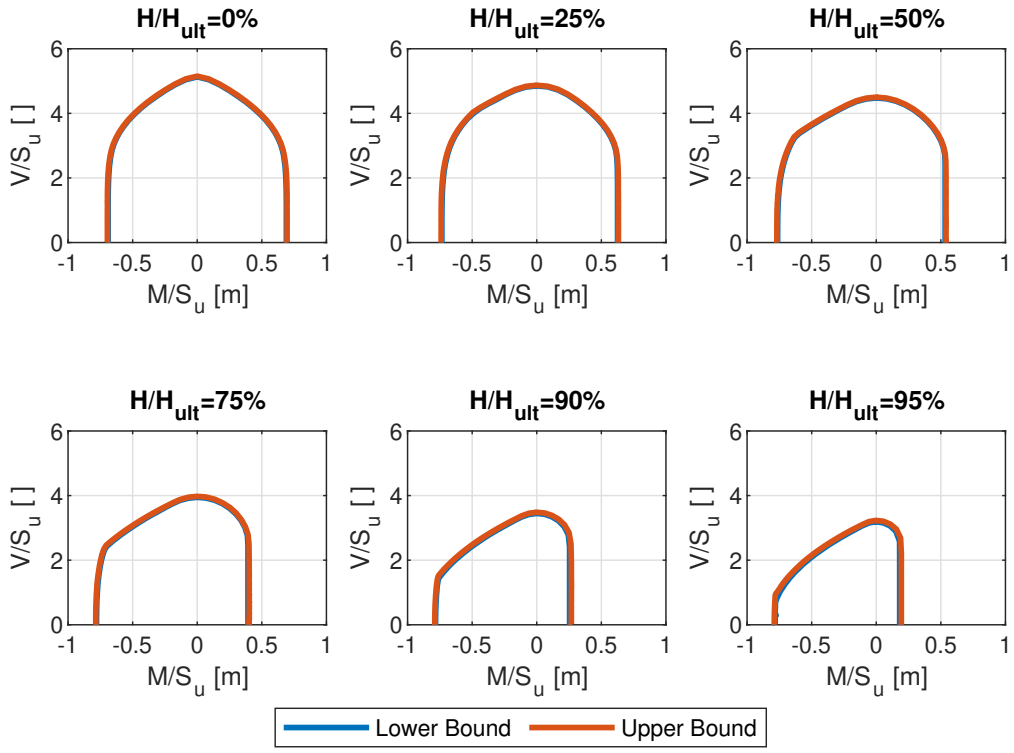


Figure 5.42: Results of lower and upper bound analyses for M-V space

chart, where horizontal stress is negative, soil mass is able to sustain higher amounts of horizontal stress and the failure line outgrows in comparison to the right side.

To show a continuous and coherent view of these cross-sections, the average of two bounds are drawn for each of the ratios in each of three spaces. This can be seen in Figure 5.44. These figures show clearly how the failure surface changes and shrinks as the ratio of the constant load increases.

#### 5.8.2.3 Macro Model

The idea of the cross-sections is, as said, to find distributed points on the failure surface in a way that a clear and representative picture of failure surface can be constructed. Figure 5.45 shows how these three cross-sections are in a 3D space. There are 3258 points overall and they show the average of lower and upper bound analyses. It can be seen how tightly the points are in a 3D space.

It has already shown how the idea of the roughness ratio can produce an exact solution. Furthermore, the roughness ratio takes into account the sliding failure by putting an upper bound to allowed horizontal stress and acts as an automatic check for sliding failure. This concept will be used to compose the macro model.

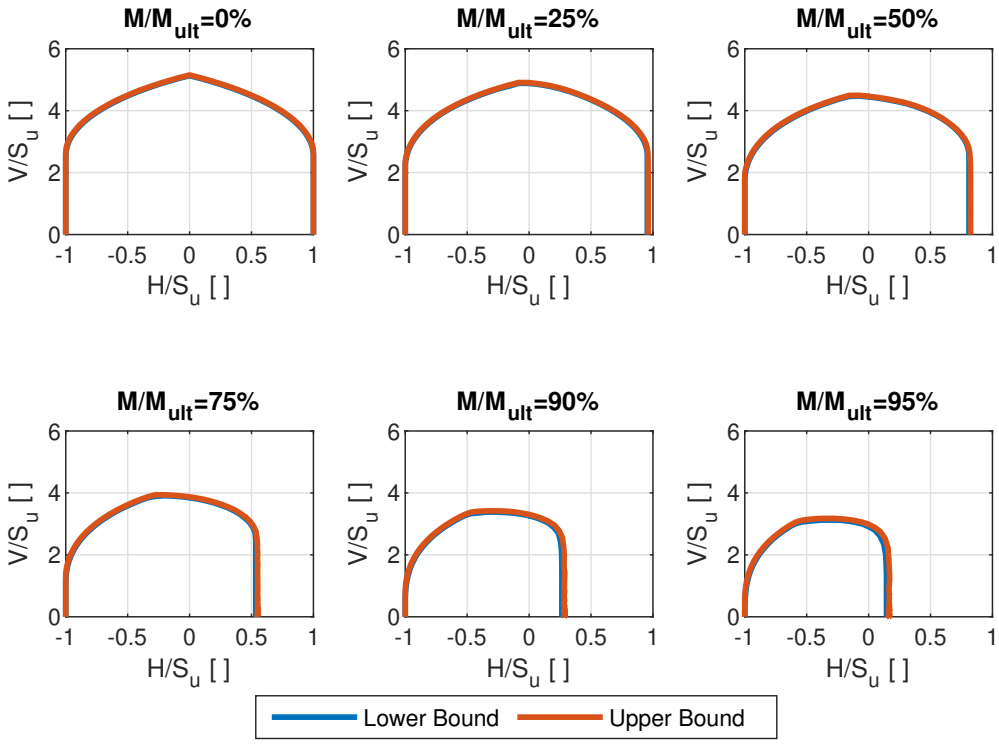


Figure 5.43: Results of lower and upper bound analyses for H-V space

The idea of composing a macro model is to propose a formula which can represent the failure surface, as it is visualized in Figure 5.45. The macro model was attempted built on the same premises as the solution proposed by Grande et al. [2016]. A macro model is found which represents acceptably the first quadrant (right side) of the failure surface, where horizontal stress and moment have similar signs. The model is defined as follow:

$$\sigma_{v,max} = 1 + \pi - \arcsin r + \sqrt{1 - r^2} - (1 - \tau_h)^{1.9} \cdot m^{0.62} \tag{5.18}$$

where:

$$\tau_h = \frac{H}{S_u} \qquad m = \frac{M}{S_u} \qquad r = \tau_h + 1 - \tau_{max} \tag{5.19}$$

Maximum allowed horizontal stress, $\tau_{max}$, is a function of the applied moment and is defined as follows:

$$\tau_{max} = \exp(a \cdot m) \cdot \cos(b \cdot m) - c \cdot \exp(d \cdot m) \tag{5.20}$$

where coefficients are as follows:

$$a = 0.0691 \qquad b = 1.768 \qquad c = 0.00152 \qquad d = 7.864 \tag{5.21}$$

The macro model can represent the right side of the problem relatively well. Figure 5.46 shows how the model is able to do this. The model, however, is underestimating the left side the of curve, but it is still on the safe side.

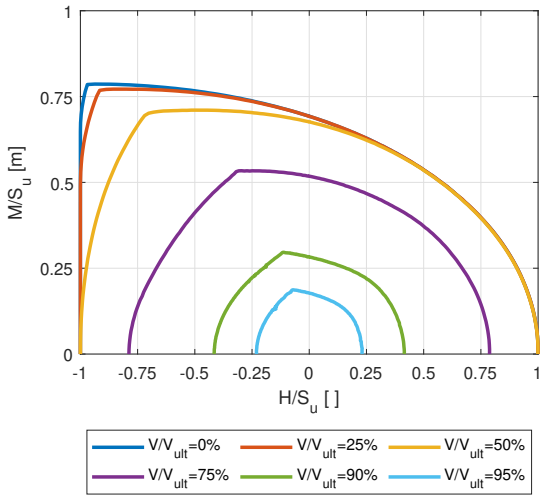


(a) HM space

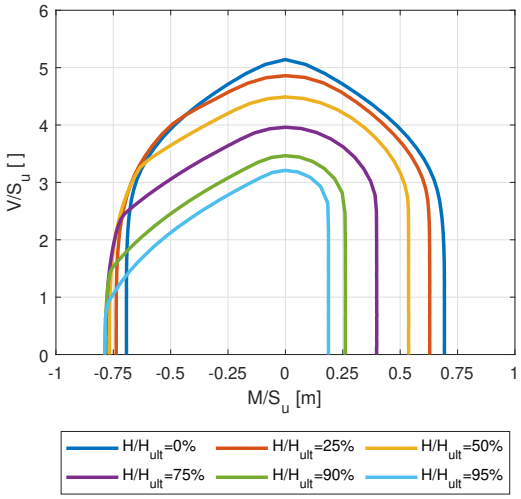


(b) MV space

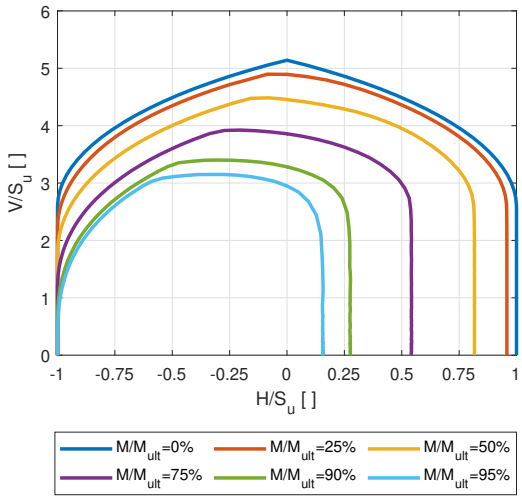


(c) HV space

Figure 5.44: Cross-sections

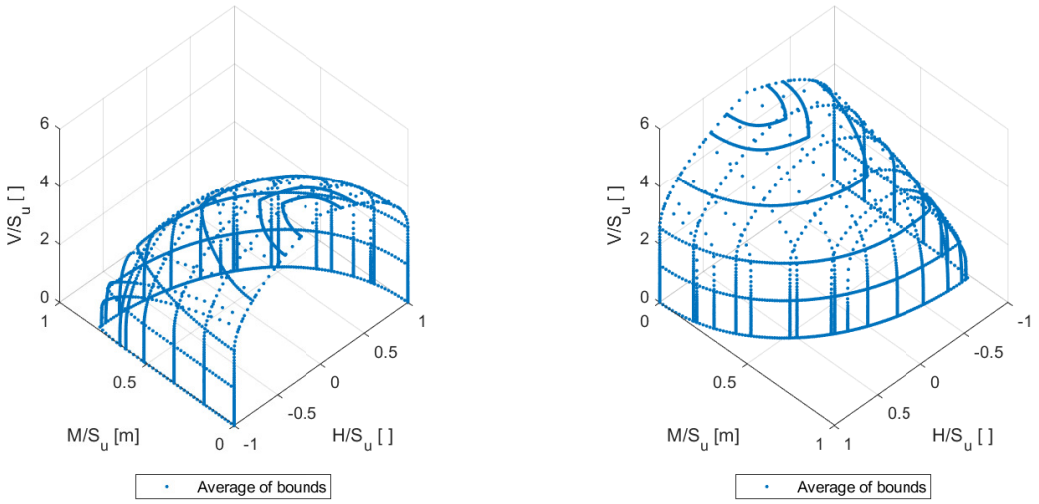


(a) forward view (b) backward view

Figure 5.45: Three dimensional representation of the executed analyses

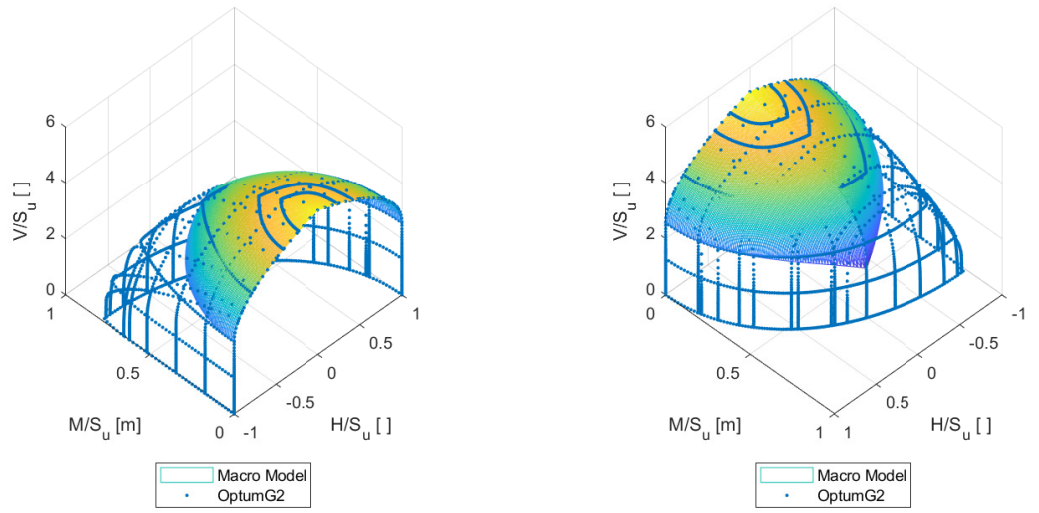


(a) forward view (b) backward view

Figure 5.46: Three dimensional representation of the macro model with executed analyses

Chapter 6

# Numerical Limit Analysis in MC Soil

In this chapter, 5 different cases of bearing capacity using Mohr-Coulomb soil will be investigated. The analyses are run with two-dimensional and three-dimensional versions of Optum and Matlab. For all of the cases, more than a dozen analyses were done by utilizing the computational unit of Optum without interacting with the graphical user interface. This is done by running Optum by using Matlab API. The codes used for this are summarized in Appendix C.

## 6.1 Case 1: Vertical loading on Weightless MC soil

In this case, the ultimate limit bearing capacity of a weightless soil under plane strain situation with overburden pressure equal to 20 kPa, and attraction, a=0 kPa, and varying friction angles will be investigated.

### 6.1.1 Theoretical Solution

As shown in Section 2.2, a bearing capacity formula for a weightless soil with vertical load is equal to:

$$q_{ult.} = N_q \cdot (p' + a) - a \tag{6.1}$$

where p' is the effective overburden pressure and $N_q$ is equal to:

$$N_q = \frac{1 + sin\varphi}{1 - sin\varphi} \cdot e^{\pi \cdot \tan\varphi} \tag{6.2}$$

For this case, where p'=20 kPa, ultimate limit bearing capacity is shown for varying friction angles, $\varphi$ in Figure 6.1.

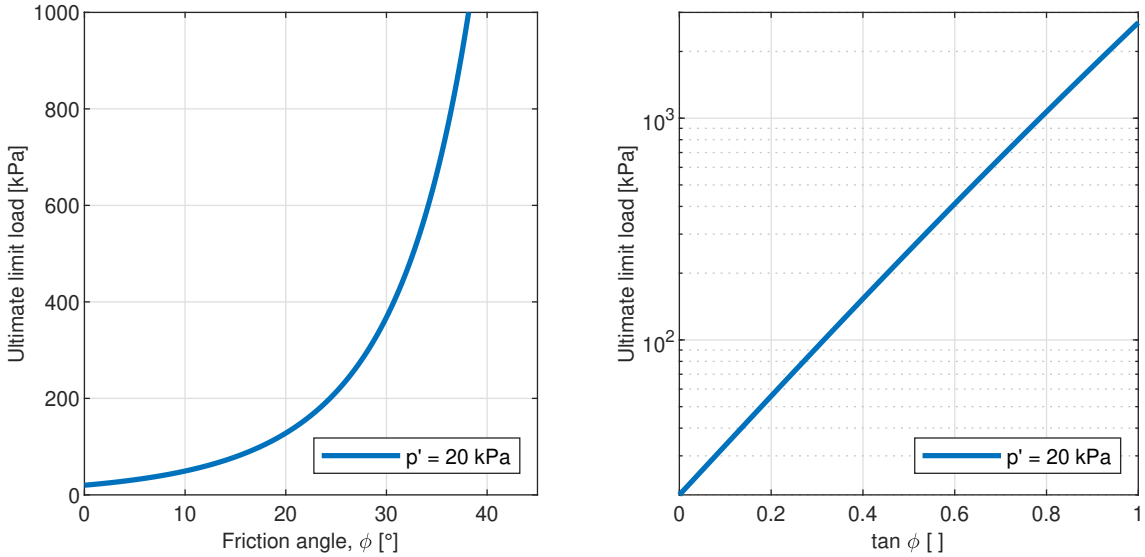


(a) 2D plot

(b) Logarithmic 2D plot

Figure 6.1: Exact Solution for ultimate limit bearing capacity for a weightless soil with p'= 20 kPa

### 6.1.2 Computation Results of *OptumG2* Runs

For this case, two sets of computations, with and without adaptive mesh, with a 10.000 triangular elements were run. Friction angle was increased incrementally from 15° to 45°, with 0.25° increments and the result of lower and upper simulations for each of these angles were recorded.

#### 6.1.2.1 Geometry and Meshing

Figure 6.2 shows the geometry and meshing generated by the program. The figure also depicts adaptive meshing for two friction angles. By using the adaptive meshing, the program generates finer meshing along wherever shear dissipation is high. It can be seen that when $\varphi$=45°, the failure line penetrates deeper than for case of $\varphi$=25°.

The soil body has 30 m width, 6 m height and a footing 1 m in width is resting on it. There is an overburden pressure equal to 20 kPa on each side of the foundation.

Figure 6.3, shows how the failure mechanism predicted by the program is corresponding to the failure surface suggested by Janbu (see Section 3.3 and Grande et al. [2016]). It should be noted that the failure surface penetrates deeper as the friction angle increases. It should also be noted that since the area covered by shear band increases as the friction angle increases, the shear dissipation for $\varphi = 45°$ has lower accuracy.

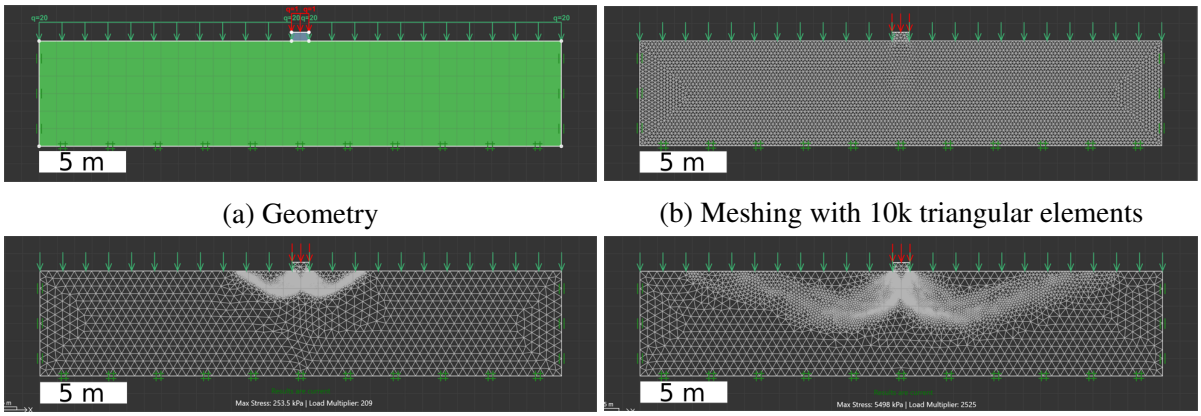


(a) Geometry

(b) Meshing with 10k triangular elements

(c) Adaptive meshing for $\varphi = 25°$

(d) Adaptive meshing for $\varphi = 45°$

Figure 6.2: Geometry and meshing of case 1

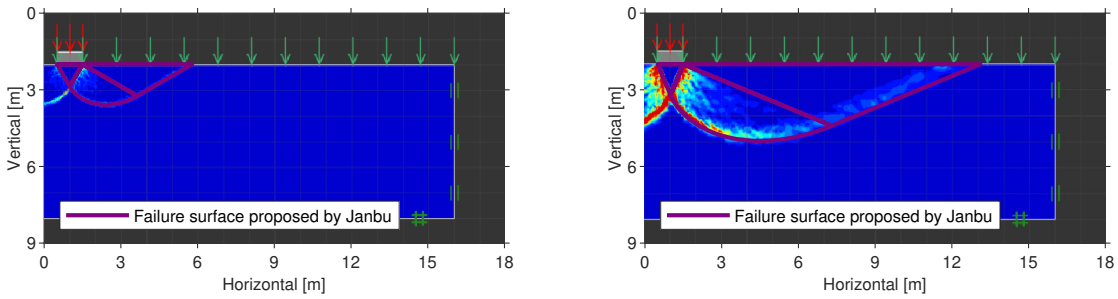


(a) $\varphi$=30°

(b) $\varphi$=45°

Figure 6.3: Comparison of failure envelope developed by theoretical solutions and obtained results

#### 6.1.2.2 Results for regular meshing

In this set of runs, ultimate limit bearing capacity was computed by running both lower and upper bound analyses for friction angles between 15° and 45°. Result can be seen in Figure 6.4. The exact solution, depicted in Figure 6.1, is drawn as well for comparison. The Figure also depicts the average of two bounds.

It also depicts the absolute relative error of lower bound, upper bound, and their average with regarding the exact solution. The error of analysis increases by increasing friction angle in general but the error of lower bound analysis increases sharper than upper bound analysis.

#### 6.1.2.3 Results for meshing with adaptive meshing

In this set of runs everything was unchanged, except adaptive meshes that were used using three iterative adaptive meshings. The results of this set of simulations can be seen in Figure 6.5. The results of lower/upper bound and their average are shown. Just like before, error increases by

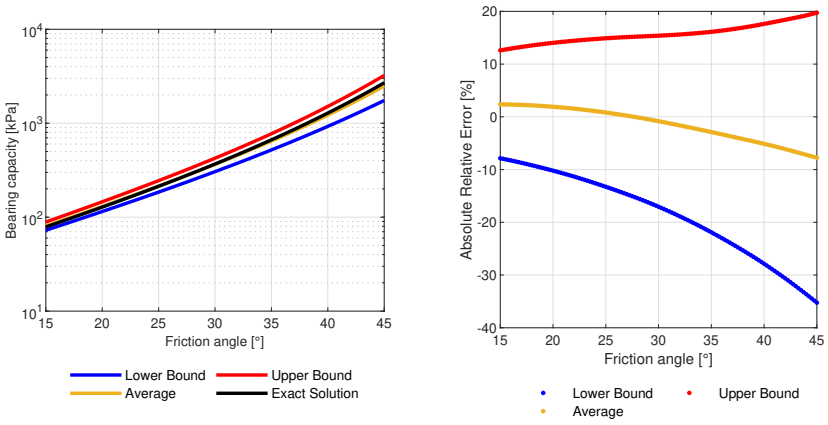


(a) Bearing capacity (log scale) (b) Absolute relative error

Figure 6.4: Result of computations for meshing with 10k triangular meshes

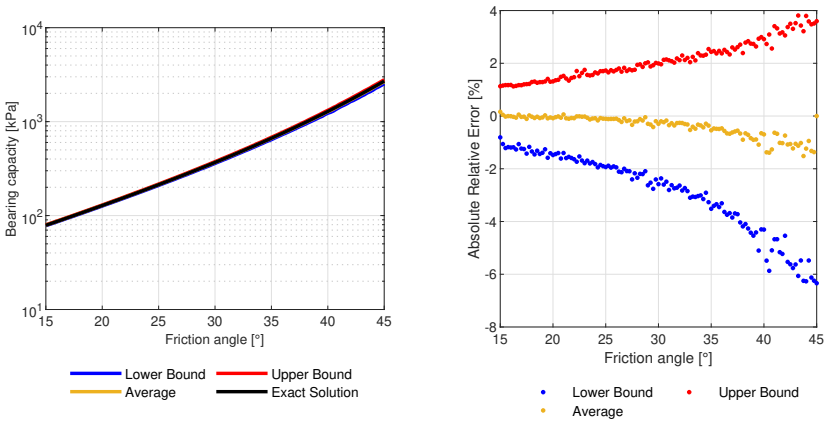


(a) Bearing capacity (log scale) (b) Absolute relative error

Figure 6.5: Result of computations for meshing with 10k adaptive triangular meshes

the increase of friction angle. The error of the average of two bounds is maximum 1%, which is acceptable.

## 6.2 Case 2: Combined Horizontal and Vertical loading on weightless MC soil

In this case, an inclined, centric load with different inclination was applied on a footing under a plane strain situation to find the ultimate limit bearing capacity of a weightless soil with overburden pressure equal to 20 kPa, and attraction, a=0 kPa and varying friction angle.

### 6.2.1 Theoretical Solution

As shown in Section 3.3, the bearing capacity formula for a weightless soil with centric, inclined load is equal to:

$$q_{ult.} = N_q \cdot p' \tag{6.3}$$

where bearing capacity factor, $N_q$ can be calculated from Equation 3.14. As shown in Section 3.3, the proposed formulas for bearing capacity factor uses the idea of a roughness ratio. For a MC soil, it is defined as:

$$r = \frac{\tau_h}{\sigma_v \cdot \tan\varphi} \tag{6.4}$$

Bearing capacity factor, $N_q$, is shown for varying roughness ratios in Figure 6.6.

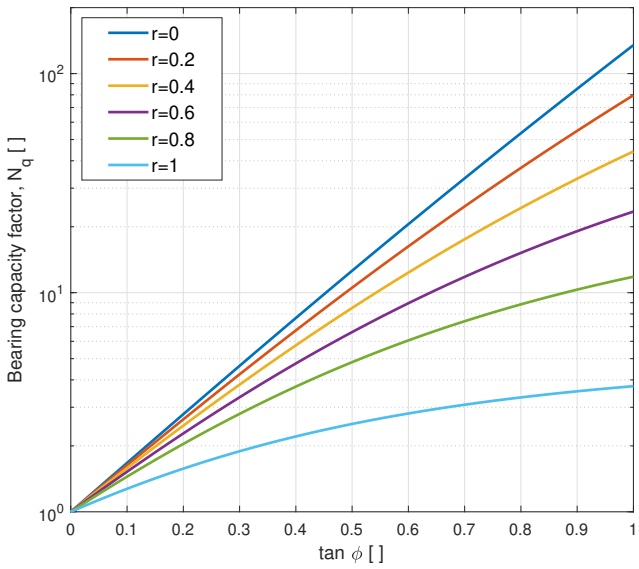


Figure 6.6: Exact Solution of $N_q$ for different roughness ratio, r (redrawn after Grande et al. [2016])

### 6.2.2 Computation Results of *OptumG2* Runs

For this case, the bearing capacity for 4 sets of different roughness ratios, namely r=0, r=0.2, r=0.6, and r=0.95, with 10.000 adaptive meshes were computed. Each set of analyzes is comprised of 60 single runs (upper bound analyses and lower bound analyses). The friction angle was increased from 15° to 45°, with a 0.5° increment, and the result of each of these angles were recorded.

#### 6.2.2.1 Geometry and Meshing

Figure 6.7 shows the geometry and meshing generated by the program. The figure also depicts adaptive meshing for three combinations of friction angles and roughness ratios.

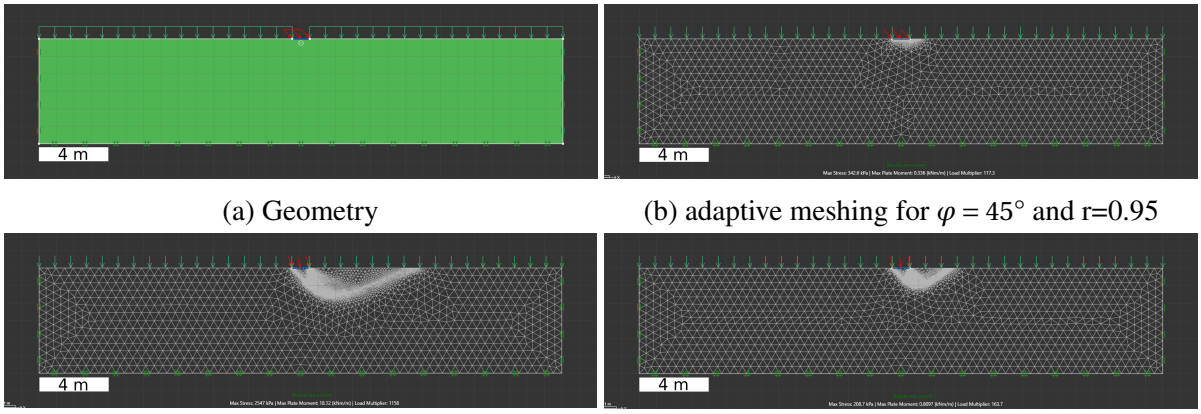


(a) Geometry

(b) adaptive meshing for $\varphi = 45°$ and r=0.95

(c) Adaptive meshing for $\varphi = 45°$ and r=0.3

(d) Adaptive meshing for $\varphi = 25°$ and r=0.3

Figure 6.7: Geometry and meshing of case 2

The soil body, in this case, is 30 m width, 6 m height and a foundation with 1 m width is resting on it while an overburden pressure equal to 20 kPa is resting on the soil adjacent to the foundations. The inclination of the load changes with the friction angle to keep a constant roughness ratio.

Figure 6.8, shows how a failure envelope changes by change of roughness ratio. Failure surface suggested by Janbu is drawn on the figures as well, to show how the failure mechanism predicted by the program is corresponding with the theoretical solution.

#### 6.2.2.2 Results for meshing with adaptive meshing

$N_q$ was calculated from the result of simulating four different roughness ratios. Figure 6.9 shows the bearing capacity factor, $N_q$, computed for roughness ratio, r=0.2. Both lower bound and upper bound are drawn a well. The absolute error is drawn and shows a maximum 4% for both bounds and error of less than 1% for the average of two bounds.

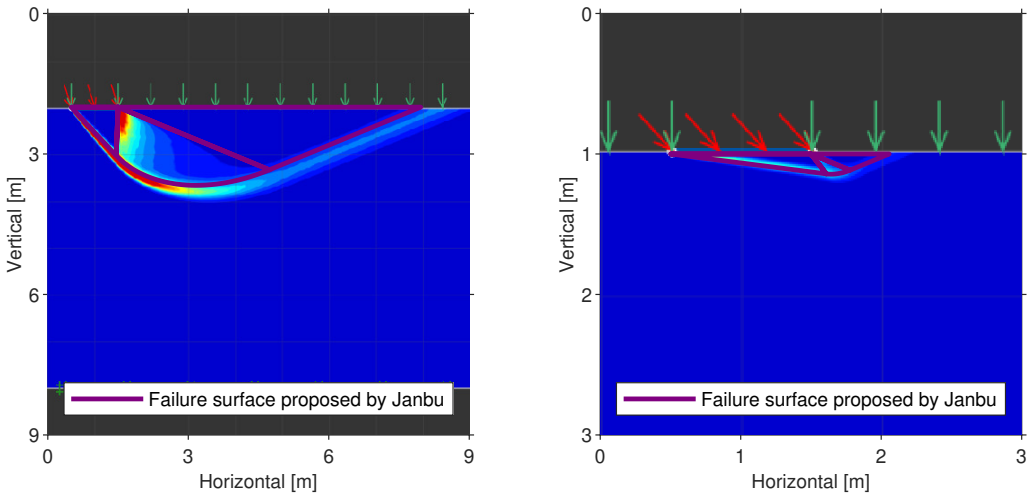


(a) $\varphi$=45° and r=0.3

(b) $\varphi$=45° and r=0.95

Figure 6.8: Comparison of failure envelope developed by theoretical solutions and obtained results for $\varphi = 45°$

Figure 6.10a shows the roughness ratio, $N_q$ versus $\tan\varphi$ for all four roughness ratios. The dotted line is the lower bound simulation, the dash-dot line is the upper bound simulation and the solid line is the exact solution as discussed previously (see Section 3.3). Finally, Figure 6.10b shows the error of the average of lower and upper bound for these 4 roughness ratios. It can be seen that the error is generally under 1% which is generally acceptable. It should be noted that r=0.95 is the highest roughness ratio which was possible to use with reasonable error margins.

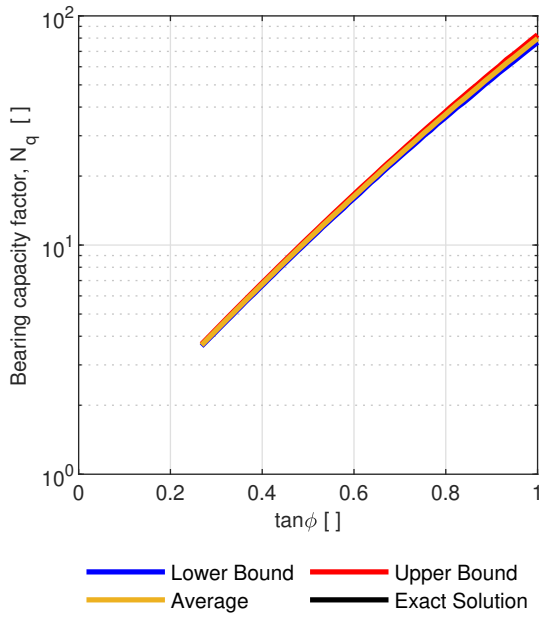


(a) $N_q$-tan$\varphi$ plot

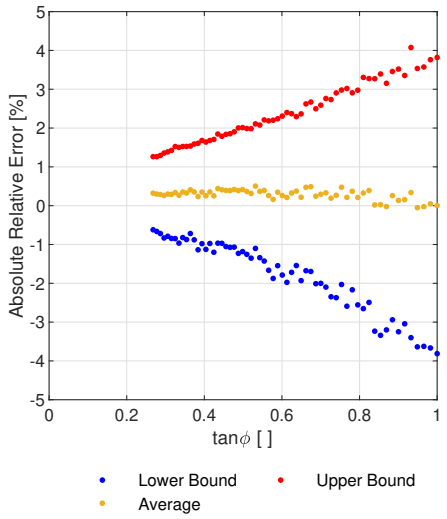


(b) Absolute relative error

Figure 6.9: Results of computation for roughness ratio r=0.2

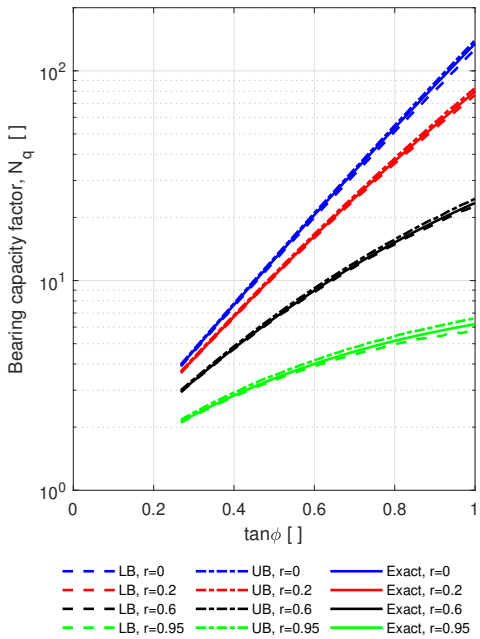


(a) $N_q$-tan$\varphi$ plot

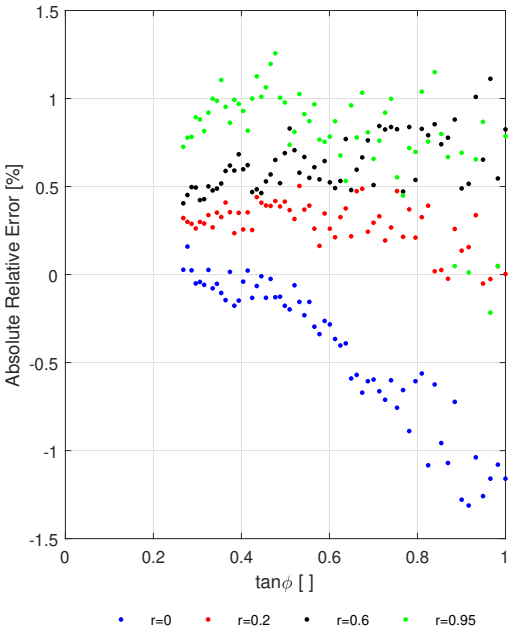


(b) Error of average of two bounds

Figure 6.10: Results of adaptive meshing for different roughness ratios

## 6.3 Case 3: Vertical loading on ponderable MC soil

In this case, it is attempted to calculate the ultimate limit bearing capacity under a plane-strain situation on a soil without overburden pressure, and attraction, a=0 kPa, unit weight, $\gamma$=20 $\frac{kN}{m^3}$ and varying friction angles.

### 6.3.1 Theoretical Solution

As discussed in Chapter 2, bearing capacity for a ponderable soil ($\gamma \neq 0$), without overburden pressure and attraction, under a vertical centric loading is equal to:

$$q_{ult} = \frac{1}{2} \cdot N_\gamma \cdot \gamma \cdot B \tag{6.5}$$

The solution developed by Martin [2004] gives an exact solution for $N_\gamma$, and it will be referred to as the exact solution (seen in Figure 6.11).

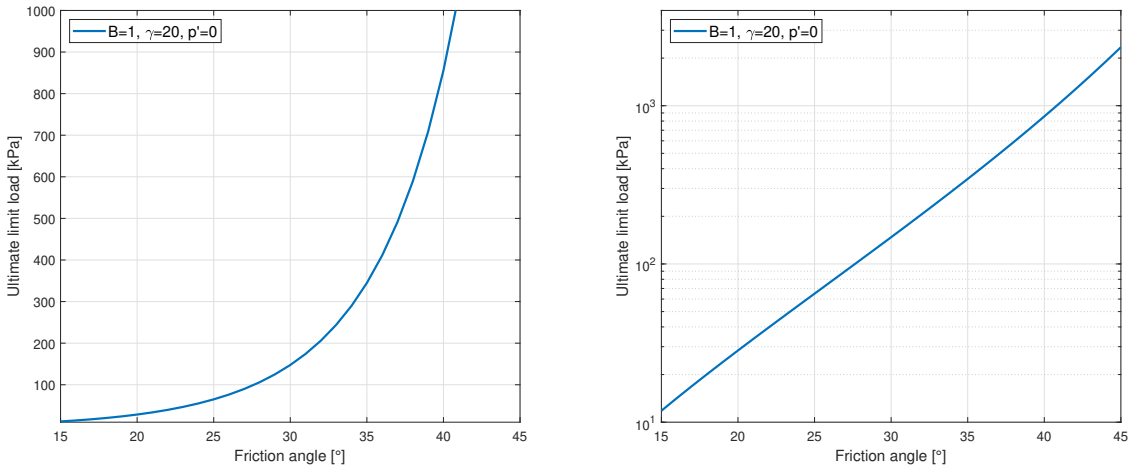


(a) 2D plot

(b) Logarthimic 2D plot

Figure 6.11: Exact solution for ultimate limit bearing capacity (redrawn form Martin [2004])

### 6.3.2 Computation Results of *OptumG2* Runs

For this case, two sets of computations, with and without adaptive mesh, with a 10.000 triangular elements were run. Each set of analyzes is comprised of 121 single runs (upper bound analyses and lower bound analyses). The friction angle was increased incrementally from 15° to 45° with 0.25° increments and the result of each of these angles were recorded.

#### 6.3.2.1 Geometry and Meshing

Figure 6.12 shows the geometry and meshing generated by the program. The figure also depicts adaptive meshing for $\varphi$=45°. Same as with case 3, as friction angle increases, the failure line penetrates deeper. Soil body has 30 m width, 6 m height, without overburden pressure and a

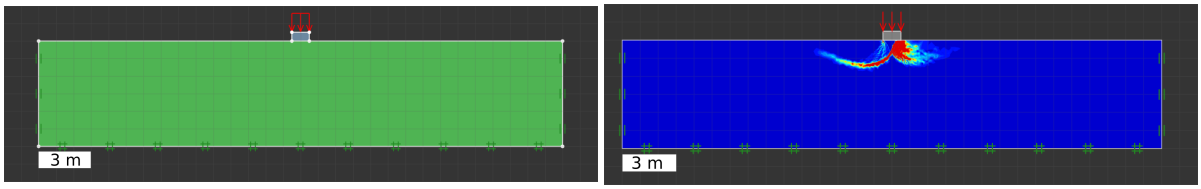


(a) Geometry (b) Shear dissipation with adaptive meshing

Figure 6.12: Geometry and meshing of case 3

foundation with 1 m width is resting on it.

#### 6.3.2.2 Results for regular meshing

In this set of runs, bearing capacity was computed by running both lower and upper bound analyses for friction angles between 15° and 45°. Figure 6.13 shows the relationship between friction angle and ultimate limit bearing capacity for this case. The average of lower and upper bounds is depicted as well as the solution developed by Martin [2004], which is the exact solution. The figure also depicts the error of lower and upper bounds and their average, with varying friction angles. The error of analysis increases by increasing friction angle in general, but the error of the average of two bounds decreases. This is because of how the error of lower bound solutions are increasing more and this is pushing the average closer to the exact solution.

#### 6.3.2.3 Results for meshing with adaptive meshing

In this set of runs, everything was unchanged except adaptive meshing was used. The results of this set of simulations can be seen in Figure 6.14. Absolute relative error increases by the increase of friction angle. Absolute relative error of the average of two bounds is around 2% to 7%, which can get better by using more refined meshing and/or by using mesh fans.

As can be seen in the figure, the result of the lower bound is showing scattering behavior and this is because of numerical difficulties near the corner of foundation and soil.

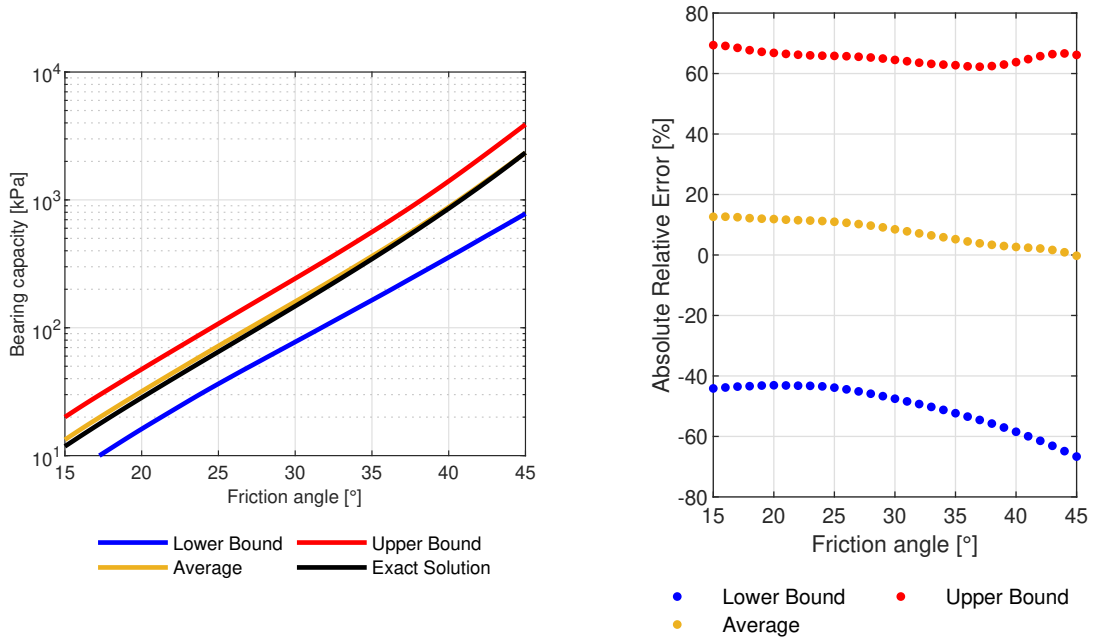


(a) Bearing capacity (log scale)

(b) Absolute relative error

Figure 6.13: Result of computations for meshing with 10k triangular elements

#### 6.3.2.4 Comparison of results

Average of upper bound and lower bound can give a good estimate of the real answer. The average of two bounds for regular meshing and adaptive meshing are calculated and the results can be seen in Figure 6.15.

The figure also shows the error of each of these meshings. Adaptive meshing is generally predicting a more accurate result. However, the error of regular meshing is lower than adaptive meshing after a point which is a coincidence, especially considering a larger gap between the lower bound and upper bound for the case of regular meshing.

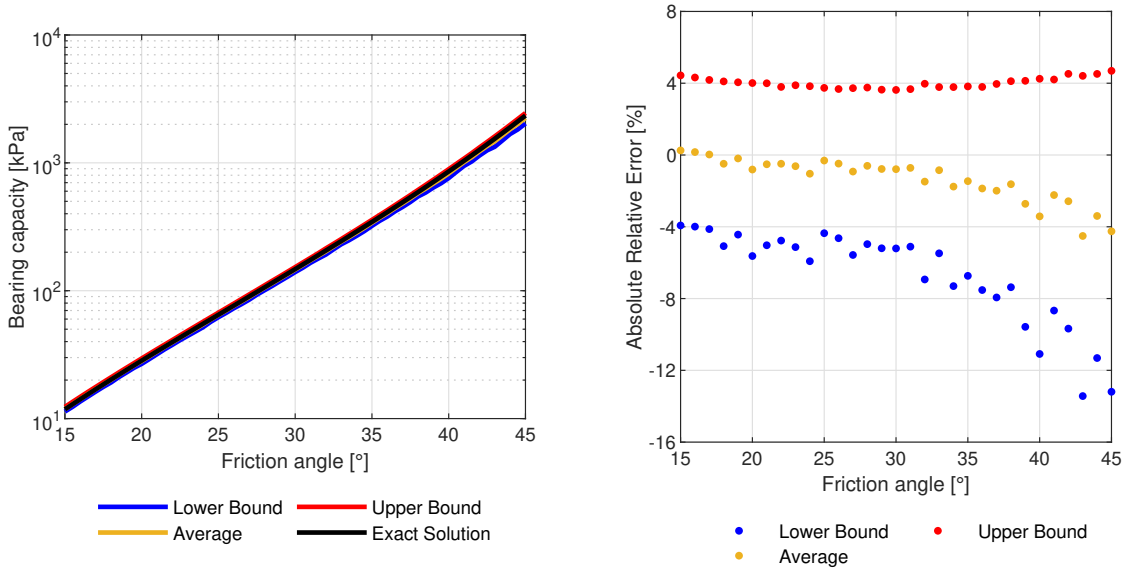


(a) Bearing capacity (log scale)

(b) Absolute relative error

Figure 6.14: Result of computations for adaptive meshing with 10k elements

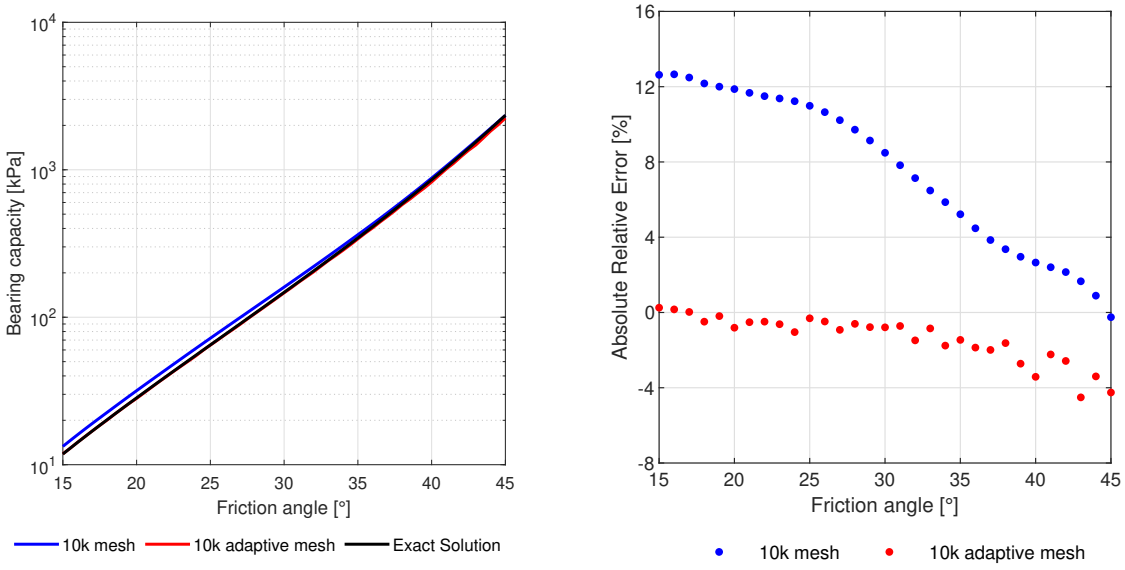


(a) Bearing Capacity

(b) Absolute relative error

Figure 6.15: Comparison of average of two bound for regular meshing vs adaptive meshing

## 6.4 Case 4: Vertical loading of a circular foundation on ponderable MC soil

In this case, the ultimate limit bearing capacity of a ponderable, cohesionless soil with varying friction angles under a circular footing will be investigated.

### 6.4.1 Theoretical Solution

There is no rigorous solution for the shape factor of circular foundations. There are, however, some solutions suggested by some authors, which are mentioned in Chapter 3. The solution proposed by Meyerhof [1963] is as follows:

$$s_\gamma = 1 + 0.1 \tan^2\left(\frac{\pi}{2} + \frac{\varphi}{2}\right) \tag{6.6}$$

This shape factor is over 1. On the other hand, Vesić [1973] suggests a shape factor equal to $s_\gamma$=0.6, and Norsk Standard [2016] suggests a factor equal to 0.7. This contrasting incompatibility will be discussed in Chapter 8.

### 6.4.2 Computation Results of OptumG2 Runs

For this case, bearing capacity of circular foundation was computed for a ponderable, cohesionless soil with varying friction angles. The two-dimensional version of the Optum, by using axisymmetry, was used to run lower and upper bound analyses. The friction angle was increased incrementally from 15° to 45°, with 0.5° increments, totaling 61 analyses.

#### 6.4.2.1 Geometry and Meshing

Figure 6.16 shows the geometry and meshing used in this case. The soil body has 18 m width and 6 m height. There is a foundation with a 0.5 m radius resting on the top of the soil mass. 45.000 triangular elements were rearranged through 3 iterations of adaptive meshing for this case. Meshing for a special case of $\varphi = 45°$ is shown in the figure.

#### 6.4.2.2 Results of simulation with adaptive meshing

Figure 6.17 shows the results of the simulations for this case. Bearing capacity factor, $N_\gamma$, was calculated as

$$\frac{q_u}{0.5 \cdot \gamma \cdot B} \tag{6.7}$$

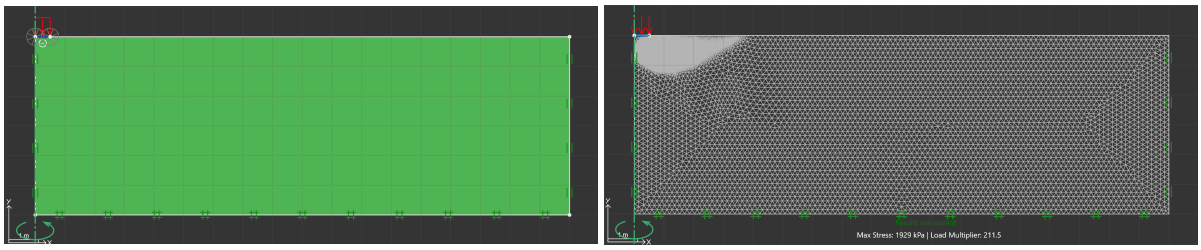

(a) Geometry (b) Meshing

Figure 6.16: Geometry and meshing for circular foundation on a MC soil with $\varphi = 45°$ (45.000 triangular elements)

The figure shows a plot of $N_\gamma$ versus $\tan\varphi$ to illustrate the effect of increasing friction angle.

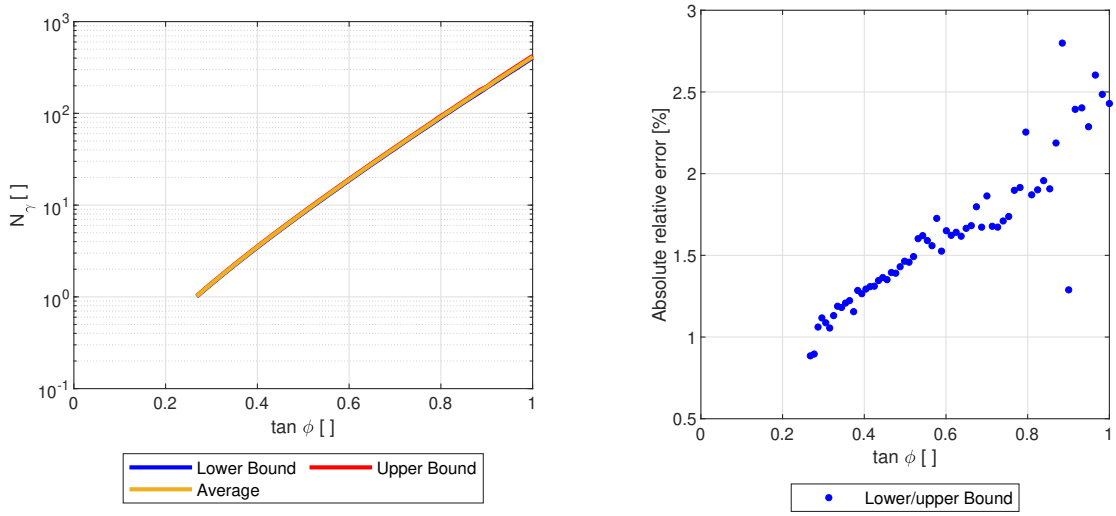


(a) $N_\gamma$-$\tan\varphi$ plot (b) Absolute relative error

Figure 6.17: Results of computation for case 4 using axisymmetry in OptumG2

The figure also shows the absolute relative error of the analyses. Since there is no exact solution, the absolute relative error was calculated as mentioned in Section 4.3.2.

### 6.4.3 Computation Results of OptumG3 Runs

For this case, bearing capacity of a circular foundation resting on a cohesionless, ponderable MC soil was analyzed using lower, upper, and mixed element type. By using the Mohr-Coulomb soil model, the bearing capacity of the soil was computed by using the three-dimensional version of Optum. The friction angle was increased incrementally from 15° to 45°, with a 1° increment, totaling 31 analyses. Only $^1/_4$ of the problem was modeled for reducing computation cost/time.

#### 6.4.3.1 Geometry and Meshing

Figure 6.18 shows the geometry and meshing used for this case. A soil body with dimensions of 10×10×6 (B×L×H) was used where a foundation with 1 m radius is resting on the soil mass.

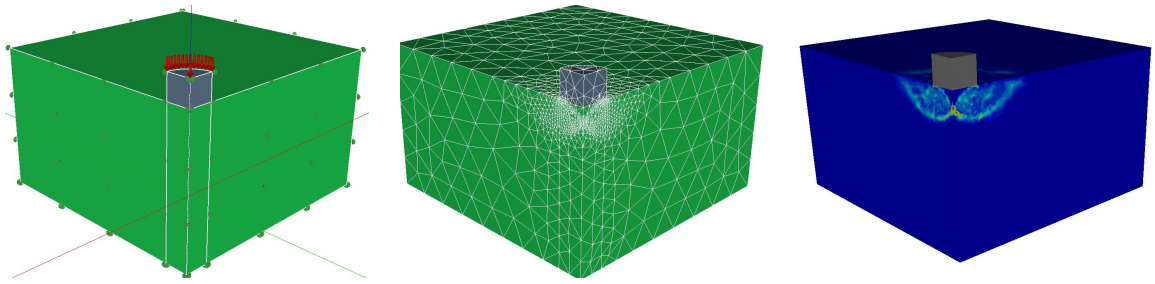

(a) Geometry (b) Meshing (c) Shear dissipation

Figure 6.18: Geometry and meshing for circular foundation on a MC soil with $\varphi = 30°$ (25.000 triangular elements)

The case shown in Figure 6.18 is for a soil mass with $\varphi = 30°$. Adaptive meshing with 25.000 elements was used. Elements were rearranged through 3 iterative adaptive meshing for decreasing the so-called gap between lower and upper bound analyses (see 4.3.2).Three types of elements, namely lower, upper, and mixed type of meshing were used in this case.

#### 6.4.3.2 Results of simulation with adaptive meshing

Figure 6.19 shows the results of simulation. Bearing capacity factor, $N_\gamma$, is calculated as described in the 2D subsection. The figure shows the results of computation for different friction angles.

The figure also depicts the absolute relative error of the lower/upper solution. It can be seen that absolute relative error increases dramatically as the friction angle increases. The error for 3D analysis is generally higher than the similar simulation with the two-dimensional version of Optum.

### 6.4.4 Comparison of results

Based on the simulation results, it is possible to propose a formula for $N_\gamma$. The average of lower and upper bound simulation from the two-dimensional simulations were used to form a new formula. The data point of average of lower and upper bounds can be described with the following formula (for the interval of 15° to 45°):

$$N_\gamma = \exp\left(9.254 \cdot \tan\varphi^{0.7893} - 3.242\right) \tag{6.8}$$

This formula gives a maximum 1.4 % absolute relative error, which is satisfactory.

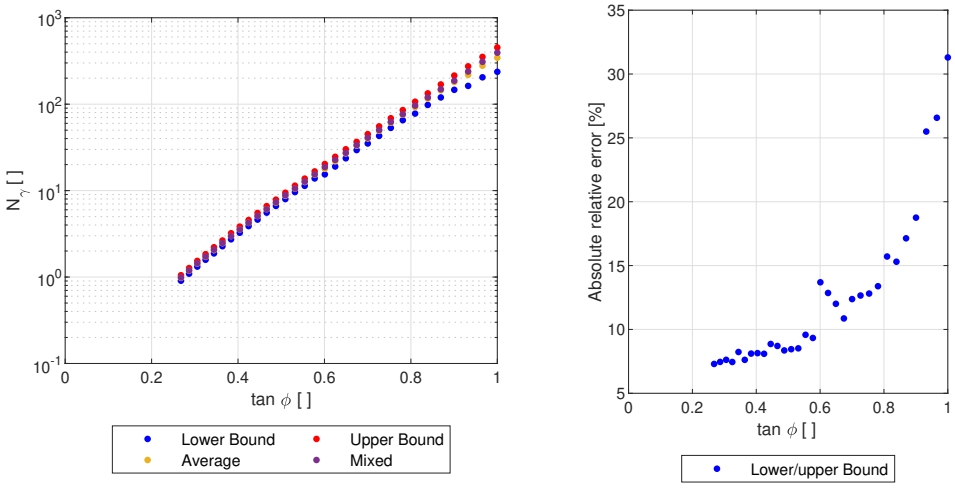


(a) $N_\gamma$-tan$\varphi$ plot (b) Absolute relative error

Figure 6.19: Results of computation for case 4 using OptumG3

Figure 6.20 shows a comparison between the results of two-dimensional and three-dimensional analyses with the proposed formula.

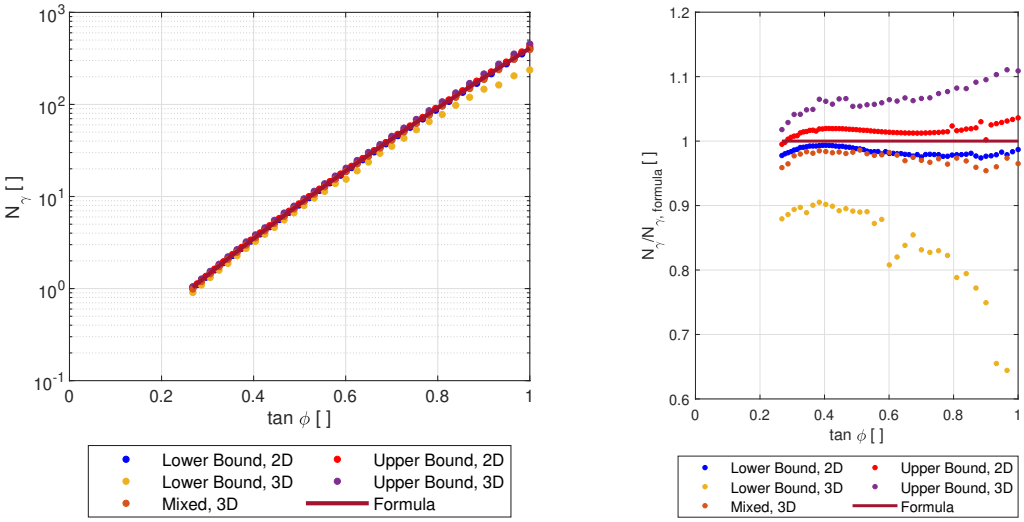


(a) $N_\gamma$-tan$\varphi$ plot (b) Normalized $N_\gamma$-tan$\varphi$ plot

Figure 6.20: Comparison of proposed formula and the results of computation for case 4

The figure also shows the comparison in a normalized plot, where the $N_\gamma$ calculated from the simulation is divided by the $N_\gamma$ proposed by Equation 6.8. It can be seen that the simulation results of three-dimensional modeling are less precise than two-dimensional modeling.

## 6.5 Case 5: Combined Horizontal and Vertical loading on ponderable MC soil

In this case, the objective is to find the bearing capacity factor, $N_\gamma$, under inclined loading for different inclinations. Ultimate limit bearing capacity is computed for an inclined load on soil without overburden pressure, q=0, and no attraction, a=0 kPa, and with unit weight, $\gamma$=20 $\frac{kN}{m^3}$, and varying friction angle. The analyses were run under a plane strain situation.

### 6.5.1 Theoretical Solution

As discussed in Chapter 2, bearing capacity for a ponderable soil, without overburden pressure and attraction, under an inclined centric loading is equal to:

$$q_{ult} = \frac{1}{2} \cdot i_\gamma \cdot N_\gamma \cdot \gamma \cdot B \tag{6.9}$$

As discussed in Section 3.5, the solution developed by Martin [2004] gives exact answers for $N_\gamma$ for vertical loading. This solution will be a guide in this chapter to see how accurate the calculated $N_\gamma$ is. The solution developed by Janbu [1976] for $N_\gamma$ under inclined loading, described in Section 3.3, defines $N_\gamma$ as a function of roughness ratio, r, instead of using inclination factor, $i_c$. Janbu [1976] uses the roughness ratio for developing a solution for $N_q$ as well and as seen in Section 6.2, this solution gives similar results to the simulation results, which means it is the exact solution. The idea of roughness ratio will be used here as well to represent the inclined loading instead of the inclination factor. Roughness ratio, r is defined as:

$$r = \frac{\tau_h}{\sigma'_v \cdot \tan\varphi}$$

### 6.5.2 Computation Results of *OptumG2* Runs

For this case, lower bound and upper bound simulations were run for roughness ratio from 0 to 0.8 with 0.1 interval (9 unique values of r). For each of these 9 roughness ratios, friction angle was increased incrementally from 15° to 45° with 0.5° increments (totaling 549 unique analyses).

#### 6.5.2.1 Geometry and Meshing

The soil body, in this case, has 20 m width, 6 m height, without overburden pressure and a foundation with 1 m width is resting on it. A start element of 50.000 building up to 150.000 through three iterative adaptive meshing was used in this case. Fan mesh is used on two edges

of the foundation for increasing the accuracy of the simulation. Figure 6.21 shows the geometry and meshing generated by the program.

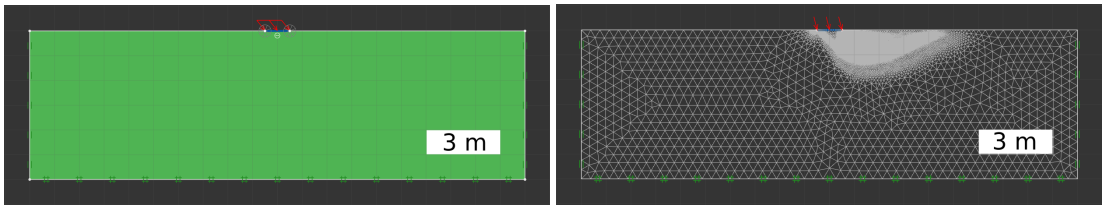


(a) Geometry (b) Meshing and mesh figuration for r=0.25

Figure 6.21: Geometry and meshing of case 5 ($\varphi$=45° and r=0.8)

Figure 6.22 shows a zoomed view of the generated meshing for a special case of r=0.2. The figure shows how fine the meshing is. Although it is not shown here, the elements along the failure line were as small as 1 mm.

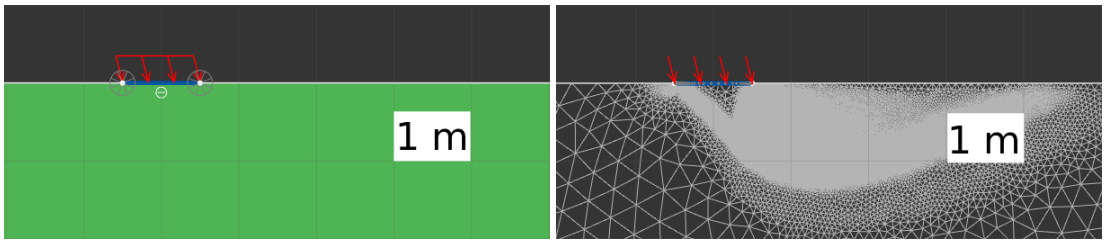


(a) Geometry with mesh fan in corners (b) Meshing and mesh figuration

Figure 6.22: Geometry and meshing for $\varphi$=45° and r=0.25

#### 6.5.2.2 Simulation results (vertical loading)

As seen in Section 6.3, the case for vertical loading on ponderable soil, the model was able to find relatively good results with comparison to the exact solution, which is the solution proposed by Martin [2004]. For the previous case, Section 6.3, the absolute relative error for the average of two bounds is between 0-4%. To reduce the error to less than 2%, the number of meshes were increased as well as utilizing a mesh fan in this case. The solution proposed by Martin [2004] for bearing capacity factor, $N_\gamma$, was used to assess the special case of r=0 or vertical loading. Figure 6.23 shows the results for r=0. The absolute relative error for the average of bounds is less than 2%.

Average of two bounds and solution proposed by Martin [2005] can be described with the following formula (for the interval of 10° to 60°):

$$N_\gamma = \exp\left(8.822 \cdot \tan\varphi^{0.7002} - 3.335\right) \tag{6.10}$$

This formula has a R equal to 0.9999, RMSE equal to 0.0309 and SSE equal to 0.0448.

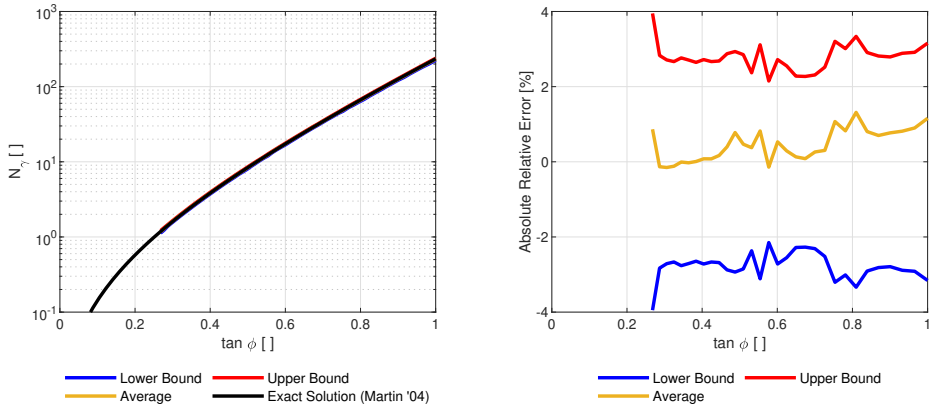


(a) Bearing capacity factor, $N_\gamma$ (log scale) (b) Absolute relative error

Figure 6.23: Result of computations for vertical centric loading

#### 6.5.2.3 Simulation results (inclined loading)

Figure 6.24 shows the results of the simulation for the 9 different roughness ratios. For each of these ratios, $N_\gamma$ of different friction angles is plotted. It can be seen that lower and upper bound results are relatively close to each other.

Figure 6.25 shows the calculated absolute relative error of the simulations, as described in Section 4.3.2, for different roughness ratios. The error is usually around 1.5%, but it occasionally goes above 2% for higher roughness ratios.

The average of lower/upper bounds for 5 roughness ratios with 0.2 intervals is shown in Figure 6.26. The average of two bounds is drawn as to not overcrowd the figure. This figure is similar to the one drawn by Janbu [1976].

Based on the average of two bounds, it has been attempted to find a formula for $N_\gamma$ which would be a function of roughness ratio and friction angle. By using the Curve Fitting Tool in Matlab, a polynomial curve was fitted to simulation results. This fitting has a coefficient of determination, R, equal to 1.000; error sum of squares, SSE, equal to 0.008314, root mean square error, RMSE, equal to 0.003927.

The equation is as follows:

$$\begin{aligned} ln\ N_\gamma = {} & 12.68 \cdot \tan\varphi + 0.3546 \cdot r - 6.968 \cdot \tan\varphi^2 - 2.419 \cdot \tan\varphi \cdot r - 0.02937 \cdot r^2 \\ & + 2.522 \cdot \tan\varphi^3 - 1.569 \cdot \tan\varphi^2 \cdot r - 1.05 \cdot \tan\varphi \cdot r^2 - 0.838 \cdot r^3 - 2.78 \end{aligned} \quad (6.11)$$

The formula with the simulation results is shown in Figure 6.27. As can be seen, the formula matches quite well with simulation results.

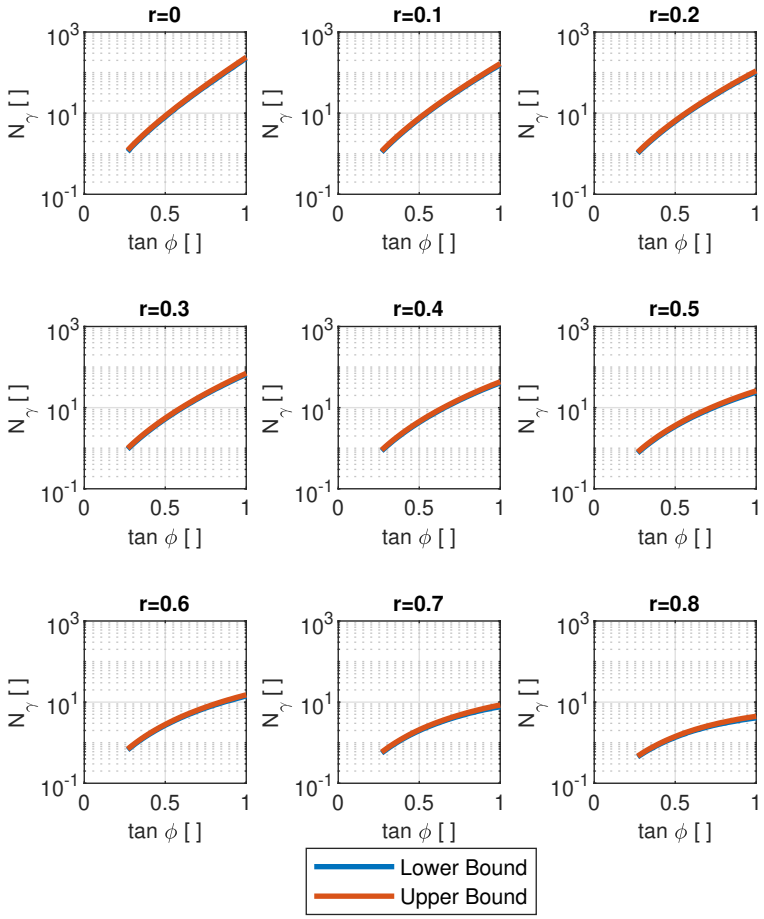


Figure 6.24: Lower/upper bound simulation results for case 5

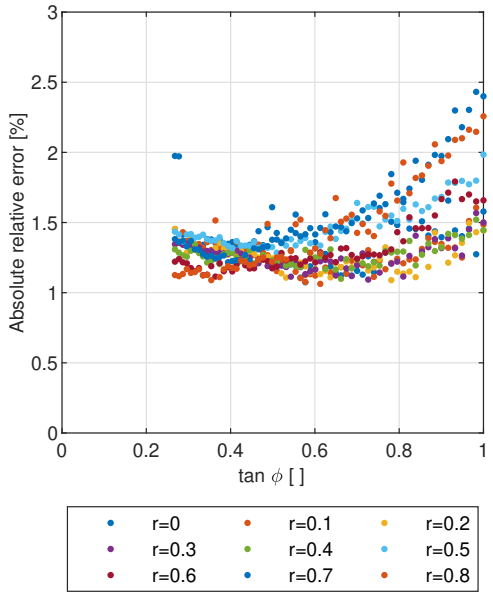


Figure 6.25: Absolute relative error of simulation of case 5

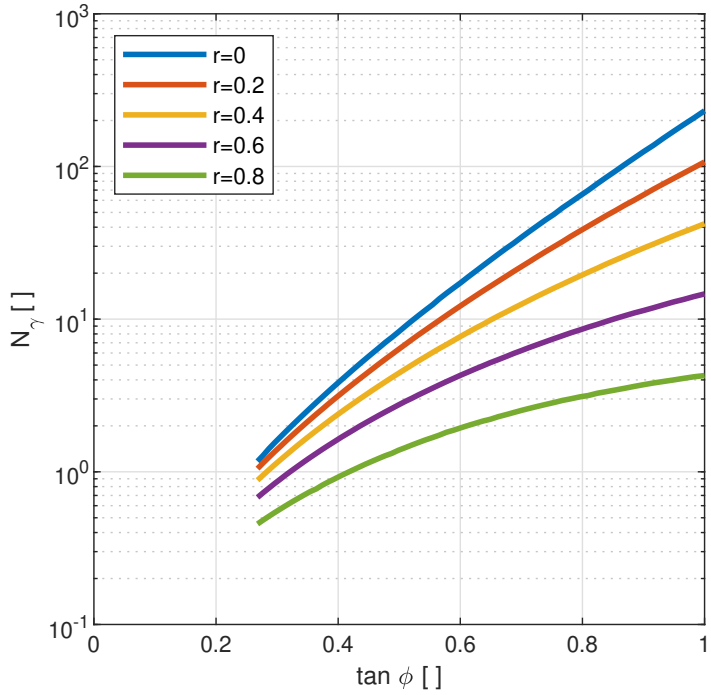


Figure 6.26: Bearing capacity factor, $N_\gamma$ calculated from average of lower and upper bounds for different roughness ratios

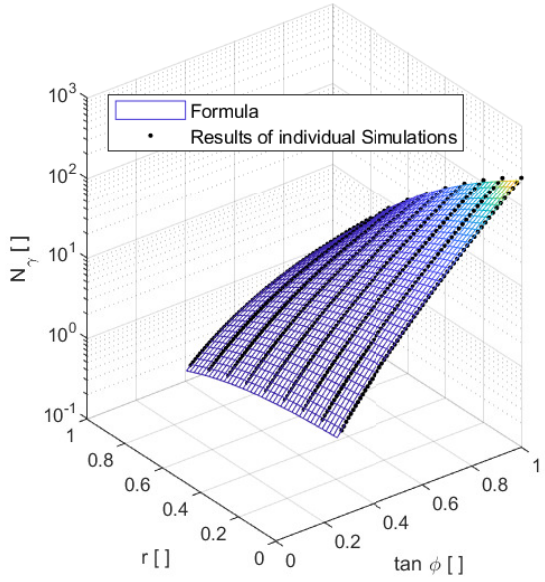


(a) $\tan\varphi - r - N_\gamma$ plot

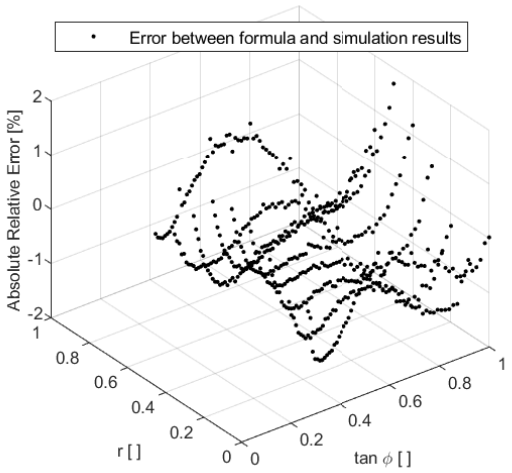


(b) Absolute relative error

Figure 6.27: New formula for bearing capacity factor, $N_\gamma$ in 3D

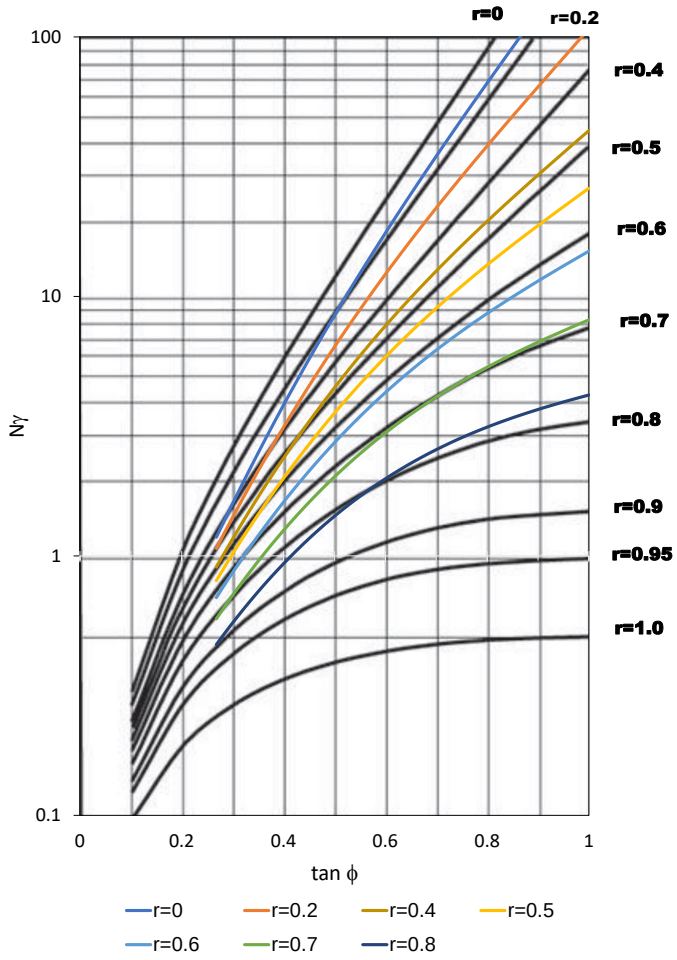


Figure 6.28: Comparison between bearing capacity factor, $N_\gamma$ predicted by Equation 6.11 and Diagram proposed by Janbu (from Aabøe et al. [2018], redrawn from Janbu [1976])

The formula fits well with the simulation results. Figure 6.27b shows the absolute relative error in 3D and 2D. As can be seen, the error is not exceeding 2% and hardly 1%.

#### 6.5.2.4 Comparison of results with Janbu's method

As discussed in Chapter 3, classical methods generally overestimate the value of $N_\gamma$, which is also the case for the solution proposed by Janbu [1976]. The computed results in this thesis are quite different from the values of $N_\gamma$ which Janbu's method proposes (see Section 3.3). Figure 6.28 shows the values of predicted $N_\gamma$ by Janbu and the OptumG2 simulation results for different roughness ratios. The diagram presented by Janbu [1976] is drawn in the background of the plot (shown by black lines and their associated roughness ratio beside them). The solution proposed by Janbu is overestimating the $N_\gamma$ for roughness ratio 0 up to 0.6. As the roughness ratio increases, Janbu's solution starts underestimating the bearing capacity factor.

#### 6.5.2.5 Presentation of Results in H-V plot

It is possible to plot vertical bearing capacity in horizontal stress-vertical bearing capacity figures (H-V plots), as some authors like Hanna and Meyerhof [1981] have done. This can be achieved by changing the roughness ratio from 0 to an allowed maximum value. Then, by using Equation 6.11 and Equation 3.14, $N_\gamma$ and $N_q$ can be found and subsequently allowable vertical bearing capacity for each roughness ratio can be calculated as:

$$\sigma'_v = N_q \cdot (p' + a) + 0.5 \cdot N_\gamma \cdot \gamma' \cdot B_0 - a \tag{6.12}$$

Horizontal stress, $\tau_h$, for each roughness ratio is equal to:

$$\tau_h = r \cdot \tan\varphi \cdot \sigma'_v \tag{6.13}$$

An H-V plot can be drawn by plotting $\sigma'_v$ and $\tau_h$ for every roughness ratios (like Figure 6.29).

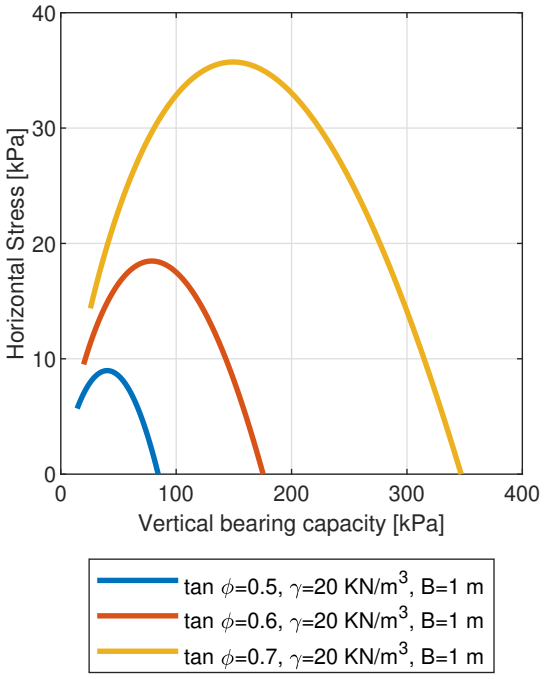


Figure 6.29: H-V plot for three different friction angles

Figure 6.29 shows an H-V plot for three different friction angles for a foundation with no attraction and overburden pressure and a foundation width equal to 1 m and soil density equal to 20 $\frac{kN}{m^3}$.

Chapter 7

# Comparison of Numerical and Experimental Results

## 7.1 Introduction

There is not an agreement on the value of bearing capacity factor $N_\gamma$, as discussed in the previous chapters. Several authors have done laboratory experiments to determine the $N_\gamma$. In this chapter, some of these laboratory experiments are compared to the numerical solution detailed in the previous chapter. Before this, selection of friction angle, which is an important issue, will be discussed.

## 7.2 Selection of Friction angle

Friction angle is assumed to be a constant parameter of soil mass throughout this thesis. This parameter, however, is a construction of how the soil sample is being tested. Several authors, such as Kulhawy and Mayne [1990] and Lade and Duncan [1973], have reported results of laboratory testings where the friction angle is not constant. Friction angle is usually interpreted from a triaxial test where the intermediate and minor stresses are equal. Under true triaxial tests, types of tests where intermediate and minor principal stress are not necessarily the same, the interpreted friction angle can vary from the one interpreted from triaxial tests. Concept of Lode angle is being used to show the influence of intermediate principal stress, which is defined as (from Lade [2016]):

$$b = \frac{\sigma_2 - \sigma_3}{\sigma_1 - \sigma_3} \tag{7.1}$$

The effect of intermediate stress on the interpreted friction angle is seen in both clay and sand. Figure 7.1 shows results of true triaxial testing done by Lade and Duncan [1973]. The inter-

preted friction angle increase as the value of b moves from b=0, triaxial compressive testing, toward plane strain before decreasing again for b=1, triaxial extension testing. The laboratory tests are done using both loose and dense sand samples. Furthermore, the figure depicts failure surfaces on an octahedral plane of three principal stresses, which depicts that Mohr-Coulomb failure criteria is not capturing intermediate stress effect.

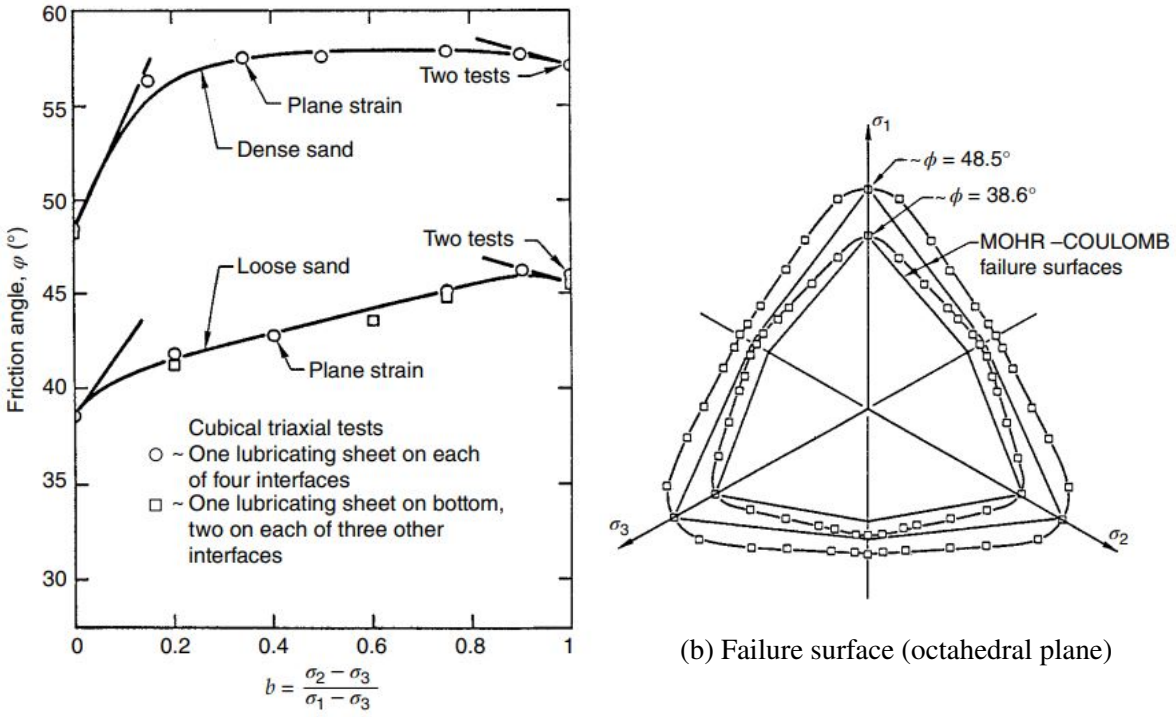


(a) friction angle, $\varphi$ vs. Lode angle, b

(b) Failure surface (octahedral plane)

Figure 7.1: Results from cubical triaxial testing with different intermediate principal stress on Monterey No. 0 sand (from Lade [2016], redrawn from Lade and Duncan [1973])

A similar phenomenon is observed for clay in the work of Lade and Musante [1978]. The results of this work are shown in Figure 7.2.

Hansen [1961] has mentioned a series of plate loading tests for soil with different interpreted friction angles from triaxial tests. Since the bearing capacity factor of the overburden effect, $N_q$ has a theoretical and rigorous solution, the results can be used for comparison. Figure 7.3 shows how using friction angles from triaxial testing, the theoretical $N_q$ (orange line) is lower than the measured values. By using a factor 1.18 for the friction angle, it is possible to get a more realistic agreement. Hansen [1961] concludes that a 10% increase in friction angle under plane strain loading from the measured friction angle from the triaxial test is common practice in Denmark ($\varphi_{ps} = 1.1 \cdot \varphi_{tr}$).

Similarly, Meyerhof [1963] suggested a 10% increase in the friction angle from triaxial loading to plane strain loading. The friction angle of plane strains is suggested to be:

$$\varphi_{ps} = \left(1.1 - 0.1 \cdot \frac{B}{L}\right) \cdot \varphi_{tr} \tag{7.2}$$

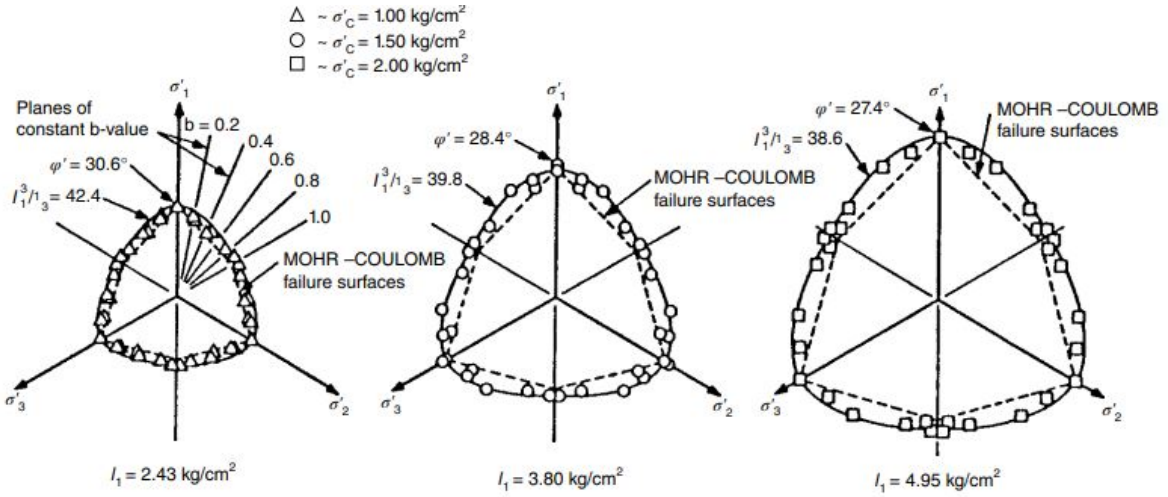


Figure 7.2: Results from cubical triaxial testing with different intermediate principal stress on remolded Grundite clay (from Lade [2016], redrawn from Lade and Musante [1978])

## 7.3 Comparison of numerical results of $N_\gamma$ with experimental results

In this section, experimental results for measuring $N_\gamma$ will be compared to the Equation 6.11, i.e. the numerical simulations.

### 7.3.1 Work of Hanna and Meyerhof, 1981

Hanna and Meyerhof [1981] run laboratory experiments to determine the bearing capacity of two types of sand samples. The experiments were run using a rectangular foundation with 5 cm width under the plane-strain condition with different loading inclinations. They used to run the experiments on the same sand with two levels of relative density, namely loose sand and dense sand. The article states that friction angle under plane strain loading for loose and dense sand is equal to 34° and 47.5°, respectively. Relative density for loose and dense sand was measured to be 0.22 and 0.69, respectively. The used soil was described as "well-graded medium to coarse angular silica sand". The minimum and maximum density of the used soil was not mentioned by Hanna and Meyerhof [1981]. However, Ameratunga et al. [2015] states that for a "well-graded sub-angular sand" the typical values for $e_{max}$ and $e_{min}$ are equal to 0.7 and 0.35, respectively. This means that dry density of loose and dense sand is 16.05 $\frac{kN}{m^3}$ and 21.83 $\frac{kN}{m^3}$, respectively.

By having soil parameters, bearing capacity for these two types of sand can be found based on the formula proposed for $N_\gamma$, Equation 6.11. Since this equation is for friction angles of $15° \leq \varphi \leq 45°$, a lower and upper bound analysis was run for dense sand where $\varphi = 47.5°$. Figure 7.4 shows a comparison of the numerical results and laboratory measured values of vertical limit stress, $\sigma_v$, versus horizontal limit stress, $\tau_h$. It can be seen that the results for dense sand

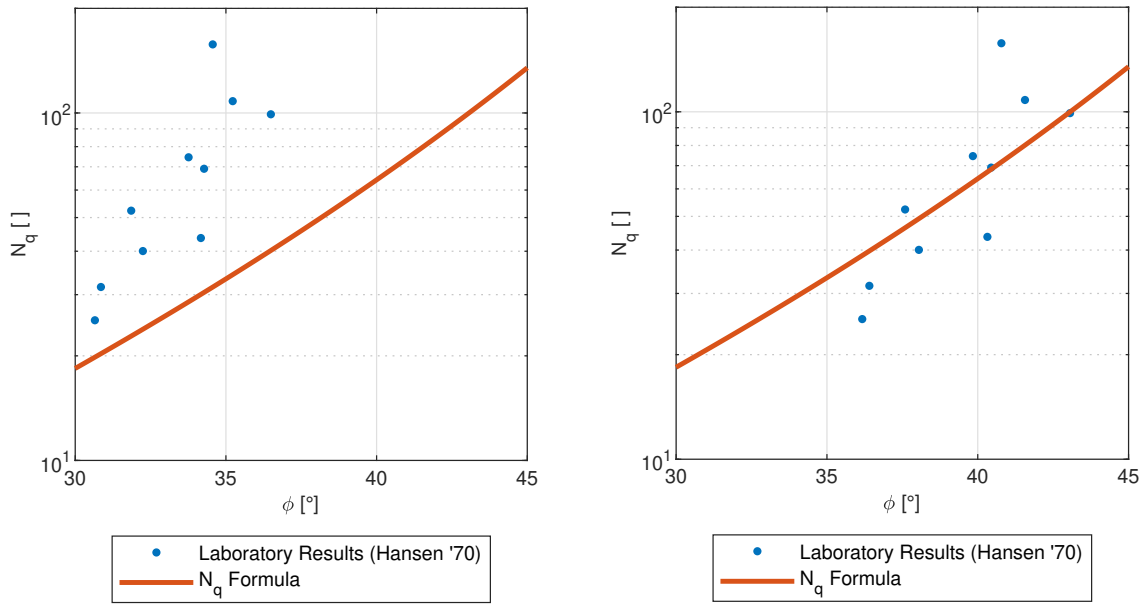


(a) friction angle from triaxial testing

(b) plane strain friction angle ($\varphi_{ps} = 1.18\varphi_{tr}$)

Figure 7.3: Comparison of plate loading tests with computed bearing capacity factor, $N_q$ using friction angle interpreted from different testing methods (redrawn from Hansen [1961])

is corresponding better with the proposed formula than loose sand.

It should be noted that a source of uncertainty is the unit weight of the soil. The proposed formula is underestimating the allowed loading for dense sand, but overestimate it for non-vertical loading of loose sand.

### 7.3.2 Work of Ticof, 1977

Ticof [1978] ran laboratory experiments using a sandbox to determine failure surface under inclined loads. The experiments used plane-strain loading by using a footing with a width equal to 76.2 mm (3 in.). Leighton Buzzard sand was used in these experiments with relative density, $D_R$ equal to 85%. Unfortunately, Ticof [1978] did not mention other properties of the sand, but since the used sand is a standard sand, there are some publications, such as Cavallaro et al. [2001], which have measured them. Cavallaro et al. [2001] have done a series of laboratory experiments on this sand and a summary of some of the results are summarized in Table 7.1.

By using these values, we can conclude that the sand used by Ticof [1978] had a dry unit weight of 17.44 $^{kN}/_{m^3}$ and a friction angle of 48.6°. Ticof [1978] has found the ultimate failure load for different load inclinations. He has summarized the results of his work in a normalised $\sigma_v/\sigma_{v,max}$ vs $\tau_h/\sigma_{v,max}$ plot. Figure 7.5 shows how the measurement of ultimate limit failure for different inclinations in Ticof [1978] compares to the simulation results for $\varphi$=48.6°(it is

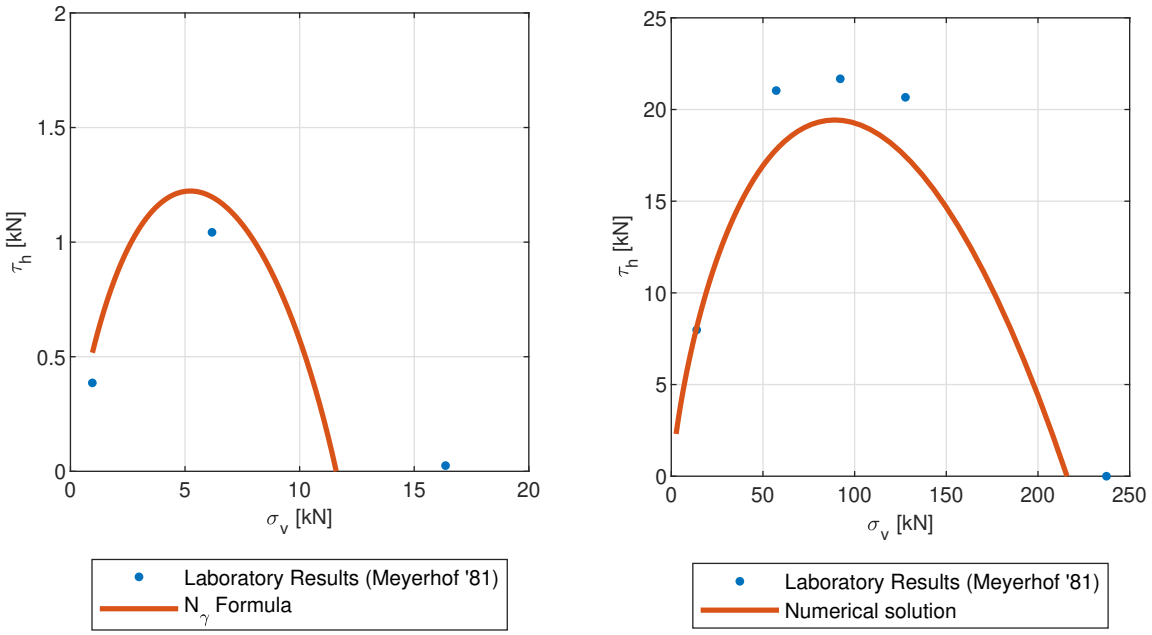


(a) Loose sand

(b) Dense sand

Figure 7.4: Comparison of laboratory tests of plane strain loading and proposed formula, Equation 6.11 (partially redrawn from Hanna and Meyerhof [1981])

Table 7.1: Some of geotechnical parameters of Leighton Buzzard sand reported by Cavallaro et al. [2001]

| Parameter | sign | value | Unit |
|---|---|---|---|
| Maximum dry density | $\gamma_{dry,max}$ | 17.94 | $[^{kN}/_{m^3}]$ |
| Minimum dry density | $\gamma_{dry,min}$ | 15.06 | $[^{kN}/_{m^3}]$ |
| Specific Gravity | $G_s$ | 2.679 | [ ] |
| Friction angle | $\varphi_{tx}$ | $= 0.238 \cdot D_R + 28.4$ | [°] |

out of range of Equation 6.11). Since the $\sigma_{v,max}$ is not mentioned by Ticof [1978], it was not possible to check the $N_\gamma$ value. Therefore, the figure is not showing the laboratory results in a non-normalized plot.

### 7.3.3 Work of Yamaguchi and coauthors, 1976

Yamaguchi et al. [1976] have measured the bearing capacity of a dense sand under plane-strain conditions with different foundation widths using centrifuge testing. The main objective of this work was to study the foundation width effect on the measured $N_\gamma$. Yamaguchi et al. [1976] used different accelerations, namely 10, 20, and 40g to model the different foundation widths. They used Toyoura sand and documented the physical properties of the used sand. Table 7.2 summarizes a list of properties of the used sand.

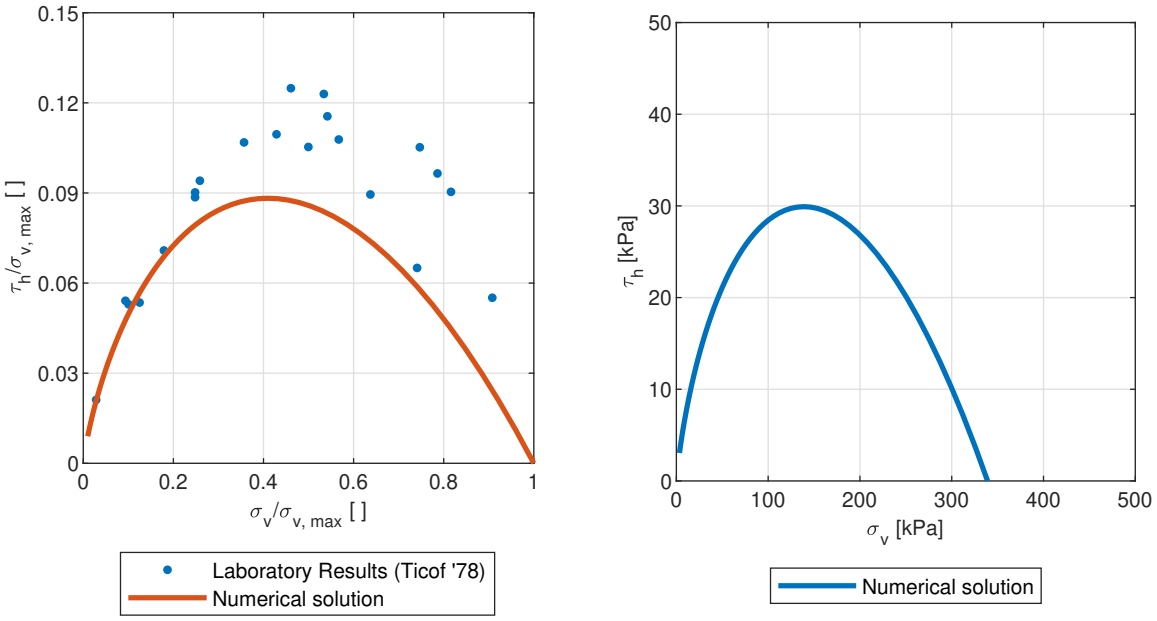


(a) Normalized $\sigma_v$ vs $\tau_h$ plot

(b) $\sigma_v$ vs $\tau_h$ plot

Figure 7.5: Comparison of laboratory tests of plane strain loading and proposed formula, Equation 6.11 (partially redrawn from Hanna and Meyerhof [1981])

Yamaguchi et al. [1976] have reported observed $N_\gamma$ for different foundation width. Their theory is that for bigger foundation footings, mean normal stress along the failure line increases, which consequently decreases friction angle. Figure 7.6 shows the observed laboratory results of $N_\gamma$ by authors and a comparison with the proposed formula for $N_\gamma$ (Equation 6.10). Since the Mohr-Coulomb model used in this thesis does not take this size-effect into account, the proposed formula is showing a constant $N_\gamma$ for different foundation sizes. It can be seen that the formula is doing a better job predicting $N_\gamma$ for higher foundation width, but not for the smaller foundations.

Table 7.2: Some of geotechnical parameters of Toyoura sand reported by Yamaguchi et al. [1976]

| Parameter | sign | value | Unit |
|---|---|---|---|
| Maximum porosity | $n_{max}$ | 49.9% | [ ] |
| Minimum porosity | $n_{min}$ | 37.9% | [ ] |
| Relative density | $D_R$ | 87.0% | [ ] |
| Average unit weight | $\gamma$ | 15.69 | $[^{kN}/_{m^3}]$ |
| Specific Gravity | $G_s$ | 2.66 | [ ] |
| Friction angle, plane strain | $\varphi_{ps}$ | 46 | [°] |
| Friction angle, triaxial | $\varphi_{tx}$ | 41 | [°] |

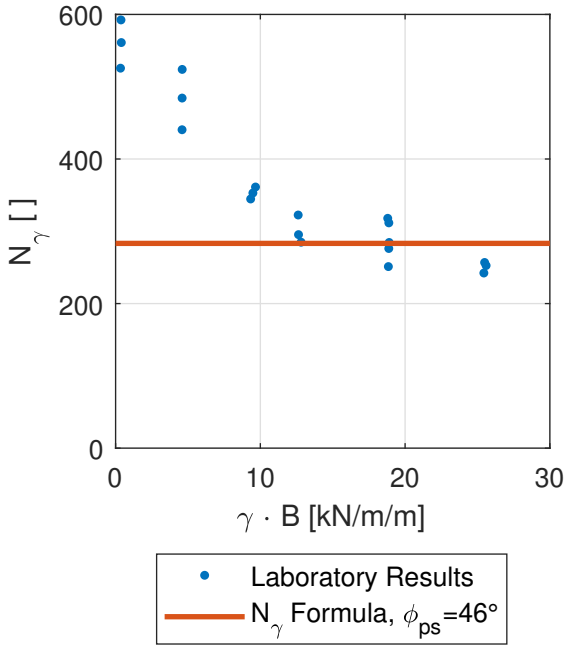


Figure 7.6: Comparison of laboratory experiments and $N_\gamma$ formula (Equation 6.10) (partially redrawn from Yamaguchi et al. [1976])

### 7.3.4 Work of Aiban and Znidarcic 1995

Aiban and Znidarčić [1995] have studied the bearing capacity of sand under plane-strain conditions with centrifuge modeling. They used fine silica sand with a relative density of 88%. The experiments were done in a 15g centrifuge using a foundation with a width equal to 38 mm, which represents a prototype of a 1.14 m foundation. A friction angle of 42° was measured through three triaxial tests. The unit weight of the soil is not mentioned by the authors. However, Ghayoomi et al. [2017] state that for standard F-75 sand, minimum and maximum dry unit for this sand is 14.69 $\frac{kN}{m^3}$ and 17.8 $\frac{kN}{m^3}$, respectively. This means that the dry unit weight of the soil is equal to 17.44 $\frac{kN}{m^3}$.

Since the authors have only measured the triaxial friction angle, not the plane strain triaxial friction angle, the ultimate bearing capacity is computed for two cases, one case where plane strain friction angle, $\varphi_{ps}$, is equal to triaxial friction angle, $\varphi_{tx}$, and one case where $\varphi_{ps}$=1.07·$\varphi_{tx}$.

Figure 7.7a shows the load-displacement curve from experiments. As discussed previously, the limit analysis only gives the limit load, not the load-deformation curve. Calculated ultimate bearing capacity is shown for two friction angles. Figure 7.7b shows the measured and calculated bearing capacity for different load inclinations. As can be seen, the Equation 6.11 is not showing a similar behavior as the measured laboratory results. This can be due to how the loading was done. Instead of applying an inclined load, the authors applied a constant horizontal

load on the footing and then applied a vertical load until it failed.

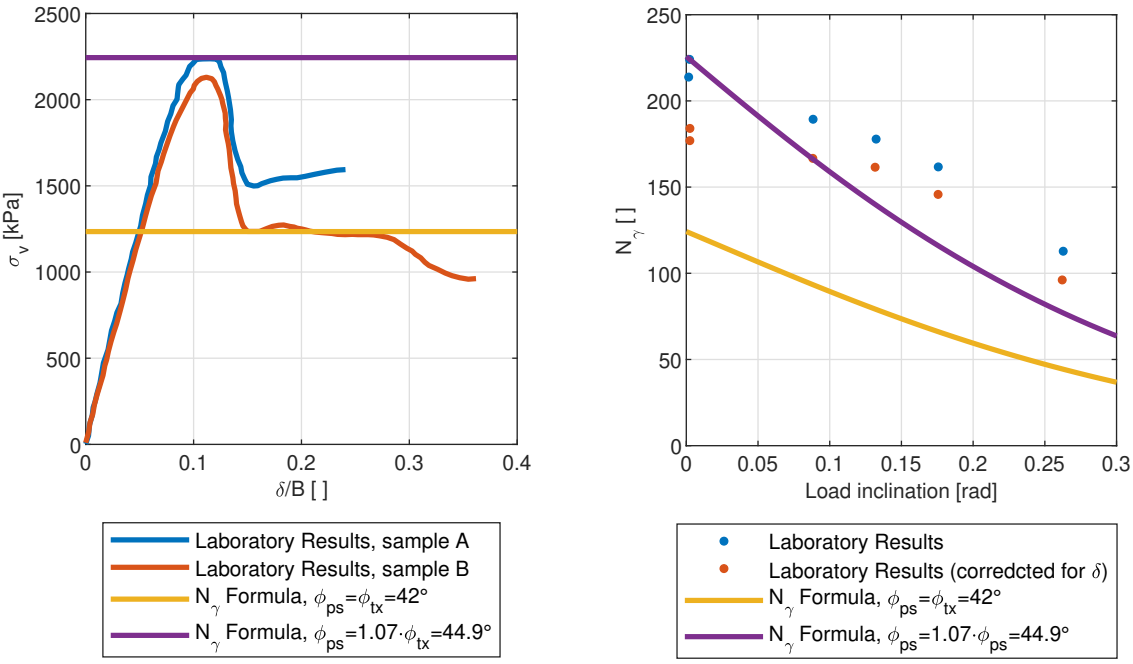


(a) Load-displacement plot

(b) $N_\gamma$-load inclination plot

Figure 7.7: Comparison of results of centrifuge testing and proposed formula, Equation 6.11 (partially redrawn from Aiban and Znidarčić [1995])

The authors have attempted to measure the $N_q$ by giving the foundation some overburden. This method of measuring $N_q$ means that the failure line can go through the overburden, which is not the same assumption made in classical bearing capacity theories (see Chapter 2). Aiban and Znidarčić [1995] have measured significantly higher $N_q$ values than what theories have suggested and this is mainly because of this effect.

### 7.3.5 Work of Leshchinsky and Marcozzi 1990

Leshchinsky and Marcozzi [1990] have done laboratory experiments using a sandbox to find bearing capacity factor $N_\gamma$ for a flexible and rigid foundation. They used a soft geotextile wrapped sand under the foundation to simulate the flexible foundation. Two foundation types, one with 50 mm and one with 38.1 mm width was used, which totals 4 types of tests. The authors used Ottawa dry sand in their experiments. The properties of the sand reported by the authors are summarized in Table 7.3.

Figure 7.8 shows a comparison of the measured $N_\gamma$ with the proposed formula, Equation 6.11. $N_\gamma$ is shown for two friction angles, one for friction angle of triaxial and one for plane strain friction angle. It can be seen that the friction angle of plane strain is corresponding better with the laboratory results.

Table 7.3: Some of geotechnical parameters of Ottawa sand reported by Leshchinsky and Marcozzi [1990]

| Parameter | sign | value | Unit |
|---|---|---|---|
| Relative density | $D_R$ | 70% | [ ] |
| Maximum density | $\gamma_{dry,min}$ | 15.2 | $[^{kN}/_{m^3}]$ |
| Minimum density | $\gamma_{dry,max}$ | 17.2 | $[^{kN}/_{m^3}]$ |
| Specific Gravity | $G_s$ | 2.67 | [ ] |
| Friction angle, plane strain | $\varphi_{ps}$ | 44 | [°] |
| Friction angle, triaxial | $\varphi_{tx}$ | 37 | [°] |

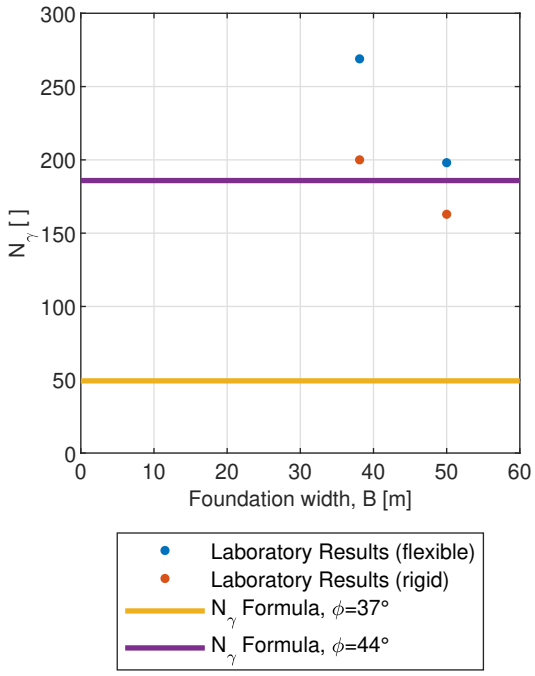


Figure 7.8: Comparison of results of laboratory testing and proposed formula, Equation 6.11 (partially redrawn from Leshchinsky and Marcozzi [1990])

Chapter 8

# Summary and Discussion

## 8.1 Discussion

Here, a summary and discussion of the work will be presented.

### 8.1.1 Superposition

Classical soil mechanics have suggested that the bearing capacity of the soil is comprised of three components, namely cohesion, surcharge, and soil density. The contribution of each of these three components can be analyzed individually and summed up to get the total bearing capacity (superposition theory according to Terzaghi et al. [1996]). This assumption is, however, quite conservative. This can be shown with an example where bearing capacity can be calculated with bearing capacity equations and finite element modeling. Since bearing capacity factors for each of these three components, cohesion, surcharge, and soil density are calculated/verified beforehand, hand calculation with formulas has to give the same results as the numerical solution.

Bearing capacity of a soil mass under vertical loading and no overburden with soil parameters and geometry given in Table 8.1 will be investigated.

Table 8.1: Soil parameters and geometry

| Parameter | Foundation width | surcharge | cohesion | friction angle | Soil density |
|---|---|---|---|---|---|
| Symbol | B | q | c | $\varphi$ | $\gamma$ |
| Unit | [m] | [kPa] | [kPa] | [°] | $[^{kN}/_{m^3}]$ |
| Value | 1 | 20 | 5 | 30 | 20 |

Bearing capacity of an MC soil under a vertical load, as mentioned in previous chapters, is

as follows:

$$\sigma'_v = (N_q - 1) \cdot (p' + a) + \frac{1}{2} \cdot \gamma \cdot N_\gamma \cdot B_0 \tag{8.1}$$

where the bearing capacity factors, $N_q$, and $N_\gamma$ are defined in Equation 3.14 and Equation 6.10, respectively. Bearing capacity for the geometry and soil parameters mentioned in Table 8.1 are:

$$\sin\varphi = 0.5 \quad \tan\varphi = 0.577$$
$$N_q = \frac{1 + sin\varphi}{1 - sin\varphi} \cdot e^{\pi \cdot \tan\varphi} = \frac{1 + 0.5}{1 - 0.5} \cdot e^{\pi \cdot 0.577} = 18.40$$
$$N_\gamma = \exp\left(8.222 \cdot \tan\varphi^{0.7002} - 3.335\right) = \exp\left(8.222 \cdot 0.577^{0.7002} - 3.335\right) = 14.44$$
$$\sigma'_v = (18.40 - 1) \cdot (20 + \frac{5}{0.577}) + \frac{1}{2} \cdot 20 \cdot 14.44 \cdot 1 = 643.18 kPa$$

Numerical simulation shows something quite different. Table 8.2 shows the results of numerical simulation for the given geometry and soil parameters (Table 8.1).

Table 8.2: Results of numerical simulation

| | Lower Bound | Upper Bound | Average | Error |
|---|---|---|---|---|
| Unit | kPa | kPa | kPa | % |
| Value | 749.4 | 784.5 | 766.95 | 2.3 |

The numerical simulation is showing a 19% increase in comparison to the formulas. As shown before, each bearing capacity factor is calculated/verified to be the exact solution, but when they are summed up as suggested by superposition theory, the results do not necessarily match. This can partly be explained by how failure surfaces and bearing capacity factors are constructed. Classical soil mechanics divides bearing capacity into three components, cohesion, surcharge, and soil weight. Failure surface and bearing capacity factors were verified/constructed under pure conditions, where each of these three components were present, one at a time. Failure surfaces can be drawn for the geometry shown in Table 8.1 for each of the three components individually (see Figure 8.1a). This shows that these three failure lines are not coinciding, where the failure line from the cohesion effect is the smallest and surcharge is largest. When a soil/geometry is modeled where these three components are acting at the same time, a new failure line, which is an amalgamation of these three lines, can be observed (see Figure 8.1b).

The failure line from Figure 8.1b is not coinciding with any of the three failure lines in Figure 8.1a. The 19% difference between the bearing capacity calculated from the formula and the numerical solution (Table 8.2) can be explained with this difference in failure lines. The failure line in Figure 8.1b is about 15% smaller than the failure line for the surcharge effect. This reduces the bearing capacity but the failure line for cohesion and soil weight (from Figure 8.1a) is quite smaller than the failure line in Figure 8.1b. This means that the failure line in Figure 8.1b is penetrating deeper and this increases the bearing capacity significantly. This phenomenon is believed to be the reason for the 19% difference between the formula and the the numerical solution.

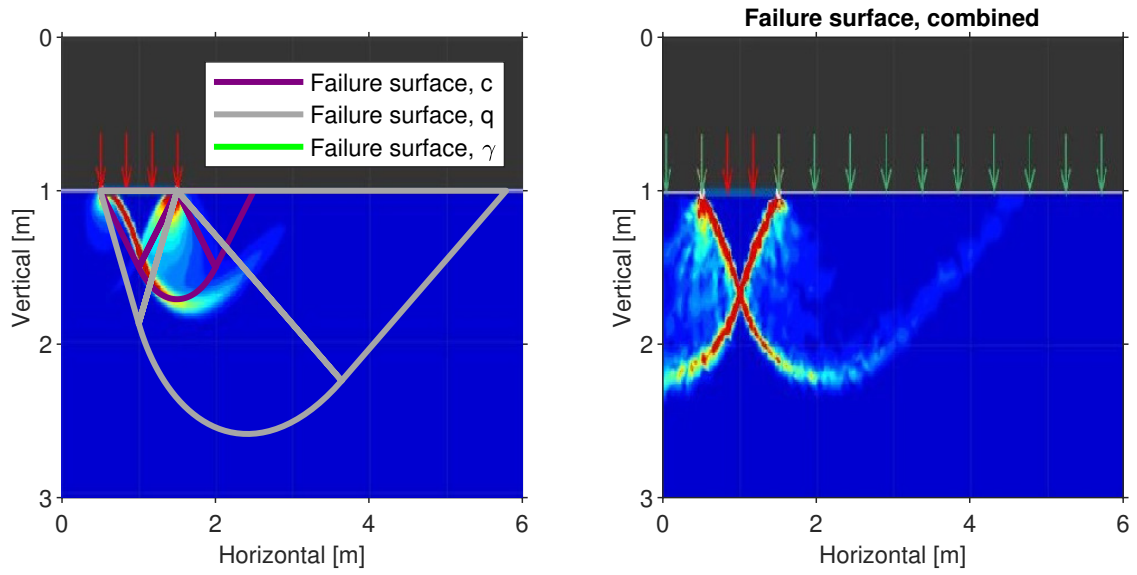


(a) Single

(b) Combined

Figure 8.1: Failure line for the example in Table 8.1

### 8.1.2 Undrained analysis

A total of 8 cases with different geometry and loading was investigated in Chapter 5. A summary and discussion will be presented here.

Case 1 was the vertical loading of a Tresca soil under plane-strain situation. The numerical solution was quite close to the theoretical solution $(2+pi)$. The idea here was to showcase the robustness of the program and adaptive meshing.

Case 2 was the vertical loading of a circular foundation on a Tresca soil. The theoretical solution for $N_c$ is 6.05. Analyses with the 2D program and axisymmetry showed that results are converging rather toward 6.03. On the other hand, analyses with the 3D program were converging toward 6.08. Even though the difference is less than 1%, this is believed to be caused by a difference in mesh refinement between two cases. This author believes that 6.03 is a better value based on the refinement of 2D analyses.

Case 3 was inclined loading of a Tresca soil under plane-strain situation. Equation 3.20 seems to correspond fairly well with numerical solutions for bearing capacity factor, $N_c$. The analyses were done with and without adaptive meshing to show the robustness of this type of meshing. Later in case 5, the inclined loading of rectangular footings was investigated but not circular footings.

In case 4, the embedment effect for a foundation on a Tresca soil was investigated for depth to width ratio up to 25. However, the results did not reach a plateau. Grande et al. [2016]

mentioned that for a deep foundation $N_c$ reaches $N_c$=2 $\cdot \pi$+2. Shallow foundation with high depth to width ratios is not something used in practical engineering. This thesis did not go into detail on the deep foundation and its bearing capacity. It was decided to limit the scope of the thesis to the shallow foundation.

A depth factor, $d_c$, was suggested to represent the results of the simulations. The proposed depth factor, Equation 5.6, is showing different results than some of the formulas suggested in the literature. This can be in explained, in part, by how previous authors have set up their formulas. This author believes that the effect of surcharge and skin resistance should not be taken into account when one sets up the depth factor. This is an unknown part of the previous works. Hence, this is a potential source of difference.

In case 5, shape effect for rectangular footings under vertical loads were investigated. With use of the 3D version of Optum, vertical bearing capacity of foundations with different width to length ratios were investigated. A shape factor, $s_c$ was suggested based on the results of the simulations.

Following that, in case 6, bearing capacity of inclined loading of rectangular foundations with different width to length ratios were analyzed. The idea was to find out if combining shape factor and $N_c$ for inclined loading is able to produce sufficient results. It was observed that the shape factor has to be a function roughness ratio as well. Based on the analyses of inclined loading of rectangular foundations, the shape factor was updated in way in which it can capture the simulation results.

In the next case, case 7, the ultimate bearing capacity of Tresca soil with linearly increasing strength with depth was investigated. Similar results with the solution suggested by Davis and Booker [1973] were obtained for vertical loading. For inclined loading, it was argued and concluded that the way Davis and Booker [1973] set up their bearing capacity formula is introducing error to the bearing capacity formula. It is concluded to formulate the bearing capacity formula for undrained analysis in the following manner:

$$\sigma_v = d_c \cdot s_c \cdot F'_R \cdot N_c \cdot S_u + p \tag{8.2}$$

where $d_c$ is depth factor (Equation 5.6), $s_c$ is shape factor (Equation 5.12), $F'_R$ is strength anisotropy factor (Equation 5.16), $N_c$ is bearing capacity factor (Equation 3.20) and p is surcharge.

Finally, in case 8, a macro model was proposed for a special case of shallow foundations with suction beneath the foundation (as a case for skirted foundations). The macro model was built on the theoretical foundation outlined in Section 3.3. Several hundreds of simulations, with relevant spatial distribution, were run to find a representative failure surface. This surface was used to find the macro model. The model is using the idea of roughness ratio, but with a difference where it is also a function of applied moment. The influence of the moment reduces the amount of horizontal stress soil can take. The macro model is constructed to represent

the first quadrant, where vertical, horizontal and moment are all positive. The macro model is outlined in Equation 5.18.

### 8.1.3 Selection of representative undrained shear strength

Clay usually displays a shear strength heterogeneity where shear strength can change based on the direction of sampling. This heterogeneity is usually expressed as three values of shear strength, namely active, direct, and passive shear strength. Representative shear strength can be expressed as:

$$S_u = \frac{S_{u,A} + S_{u,P} + S_{u,D}}{3} \tag{8.3}$$

where $S_{u,A}$, $S_{u,P}$ and $S_{u,P}$ are active, direct and passive shear strength, respectively. This idea was checked for a couple of shear strength values and it was seen to produce relatively good results. It was decided not to analyze this further in this thesis.

### 8.1.4 Drained analysis

In case 1, vertical, centric loading of a foundation on weightless soil with plane-strain condition was investigated. It shows how numerical simulations are corresponding quite well with the theoretical solution. Besides, robustness and effectiveness of adaptive meshing was shown here for a cohesionless, weightless, frictional material.

Further, inclined, centric loading of a foundation on a weightless soil with plane-strain condition was investigated. The idea of roughness ratio for developing a theoretical solution for $N_q$ was tested here. Results shows how the Janbu's solution is corresponding for four different roughness ratios. It was decided not to check other ratios as these four ratios were representative enough of possible spectrum of roughness ratios. This case showed the robustness and usefulness of the roughness ratio, which acts as an internal check for sliding.

Although the solution proposed by Martin [2005] is the exact solution for $N_\gamma$, it has not received the acknowledgment it deserves. In case 3, vertical loading of shallow foundation on ponderable soil ($\gamma \neq 0$) was investigated with plane-strain conditions and it is shown that numerical solutions are giving similar results to the solution proposed by Martin [2005]. These analyses were done with and without adaptive meshing. The difference and error between these two meshing types were more pronounced for cohesionless soil. Hence, it is suggested to use finer meshing for modeling of frictional soil. Later in case 5, vertical loading was computed with a higher number of elements to decrease the error. Based on the results of simulations and the results from Martin [2005], Equation 6.10 was suggested which can represent $N_\gamma$ for friction angles between 10° and 60°.

In the next case, case 4, bearing capacity factor, $N_\gamma$, was computed for a circular foundation.

Analyses were done using axisymmetry in the 2D program, and 3D program. It was decided to use the results of the 2D program since it had a lower error in comparison to 3D results. Based on the results, Equation 6.8 was proposed which gives $N_\gamma$ values for friction angles between 15° and 45°.

As seen in Chapter 7, the selection of a representative friction angle is not as easy as it seems to be. For a strip footing, the friction angle that should be used is the plane-strain friction angle. A representative friction angle for the circular and rectangular foundation is more complicated. Directly beneath the foundation, the stress condition is similar to triaxial testing, while around that, there is a complicated stress distribution that is closer to the non-triaxial friction angle. Hence, it can be argued both ways which friction angle, triaxial or plane-strain, should be used as the input friction angle. Either way, a correction factor has to be introduced to the bearing capacity. This factor has to be greater than 1 (like Meyerhof [1963]) if the triaxial friction angle is intended to be used and should be lower than 1 (like Norsk Standard [2016] and Vesić [1973]) if non-triaxial friction angle is intended to be used. This explains this obvious dichotomy.

A conservative way of constructing the shape factor, $s_\gamma$, for circular foundation is to use the following methodology:

$$s_\gamma = \frac{N_{\gamma,\ circular}\ (\varphi = \varphi_{tx})}{N_{\gamma,\ ps}\ (\varphi = \varphi_{ps})} \tag{8.4}$$

where $N_{\gamma,\ circular}$, and $N_{\gamma,\ ps}$ is summarized by Equation 6.8 and Equation 6.11, respectively. Based on this formula, it is possible to construct a shape factor for circular foundations. This is shown in Figure 8.2 for three different $\frac{\varphi_{ps}}{\varphi_{tx}}$ ratios. As seen in Chapter 7, this ratio can vary based on the soil type.

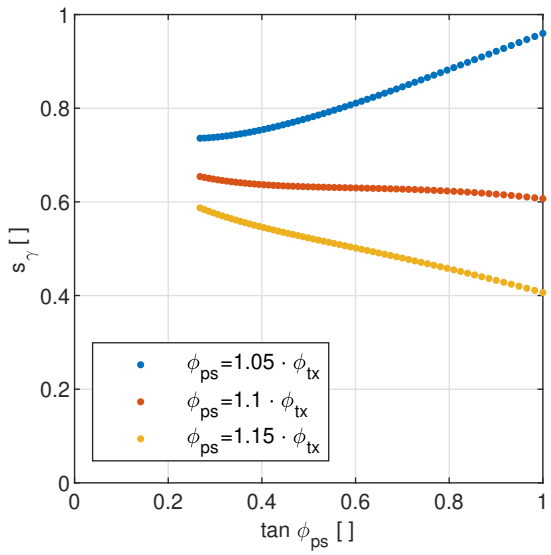


Figure 8.2: Shape factor, $s_\gamma$ for circular foundations

A shape factor equal to 0.6, suggested by Vesić [1973], seems a better choice. However, it should be noted that this gives a somewhat conservative solution since a uniform friction angle is

being selected rather than considering the effect of stress distribution on the friction angle. One way to solve this is to use a soil model which assigns triaxial friction angles for stress conditions similar to triaxial testing and assign non-triaxial friction angles to other stress conditions. FASD soil model (Friction Angle Stress State Dependent) tries to do this (see Krabbenhøft [2020]). This model was not used in this thesis, but it is recommended to be utilized in future research works for development of a more precise shape factor.

Finally, in case 5, it was attempted to create a $N_\gamma$ chart which can predict $N_\gamma$ for different friction angles and roughness ratio in the same manner as $N_q$ chart (see Figure 3.5). $N_\gamma$ was computed for friction angles from 15° to 45° for 9 different roughness ratios ( from r=0 to r=0.8). Based on the results of more than 500 simulations, a new formula, Equation 6.11, is suggested which predicts $N_\gamma$ for the mentioned intervals.

The formula is compared to the $N_\gamma$ chart proposed by Janbu [1976], which is used in common geotechnical practice in Norway. Janbu [1976] predicts higher $N_\gamma$ values for the most friction angles but not for low friction angles and higher roughness ratios.

### 8.1.5 Selection of friction angle

In Chapter 7, a comparison of the proposed formula for $N_\gamma$ and experimental results is presented. There is a disagreement between the results of different experimental work. Since shortcoming(s) and possible source(s) of error are not mentioned in any of these works, it was hard to find a way to dismiss the ones which might not be accurate. The proposed formula for $N_\gamma$ is compared to some of these experimental works. Numerical simulations are showing some agreement with the experimental results. This author believes that more experimental work has to be done to fill the void.

### 8.1.6 Roughness ratio

Throughout this thesis, the roughness ratio was used to represent the inclination of the load, instead of using inclination factors. Roughness ratio, even though it is a theoretical ratio, can help for a better set up of bearing capacity formulas. Since roughness ratio can not exceed 1,0 theoretically, it acts as a upper bound for sliding failure. Although the allowed roughness ratio is theoretically 1.0, Norwegian practice sets a lower maximum allowed roughness ratio for different soil types (see Table 8.3). In procedures set up by some of the researchers, where they use inclination factors, one has to check for the sliding failure separately. Hence, the idea of the roughness ratio was preferred and is suggested to be used.

For weightless soil and cohesive soil, it has been shown that the failure line suggested and outlined in Grande et al. [2016] is corresponding with the FELA analyses. This author encourages practitioners in the field of geotechnical engineering to draw failure lines when they

Table 8.3: Maximum allowed roughness ratio in Norwegian practice (from Aabøe et al. [2018])

| Horizontal terrain | | Sloping terrain | |
|---|---|---|---|
| r | soil type | r | soil type |
| ≥ 0.9 | frictional materials | ≥ 0.8 | frictional materials |
| ≥ 0.8 | cohesive materials | ≥ 0.7 | cohesive materials |

design bearing capacity, especially for inclined loading. For maximum allowed roughness ratios in cohesive soils, 0.8, penetration of the failure line for undrained analysis is relatively shallow (maximum penetration depth is 0.32 times width).

### 8.1.7 Adaptive meshing

The robustness of adaptive meshing was shown in case 1 to 3 in Chapter 5 and cases 1 and 3 in Chapter 6. It was observed that the absolute relative error of simulation results dropped significantly for the same number of elements when adaptive meshing was used. The author suggests using this tool when it is available. This idea of using finer meshing where shear dissipation is high can be reproduced artificially. One can run the FEA with relatively coarse meshing, and after observing the results and observing where the failure goes, one can try to introduce finer mesh along the failure line.

### 8.1.8 Shortcomings and simplifications

The most important shortcoming in all of the cases in Chapter 6 is the fact that associated flow was used. This assumption is not necessarily correct, but as discussed in Chapter 2 and 3, this assumption is made implicitly in all of the classical bearing capacity theories.

## 8.2 Recommendations for Further Work

Recommendation for further work are summarized as follow:

- Developing a new theory for representing the interaction of cohesion, surcharge and soil weight (replacing superposition theory)
- Development of a macro model to include soil heterogeneity
- Development of a macro model for shallow foundation without tension beneath the foundation sole
- Development of $N_q$ and $N_\gamma$ bearing capacity for the circular and rectangular foundation with FASD soil model

- Investigation of the effect of dilation angle on $N_q$ and $N_\gamma$
- Laboratory experiments for $N_\gamma$ (vertical and inclined)
- Introducing spatial heterogeneity to the bearing capacity formulas
- Including soil-structure interface roughness

Appendix A

# Acronyms

**MC** Mohr-Coulomb

**FEA** Finite Element Analysis

**FEM** Finite Element Methods

**NTNU** Norwegian University of Science and Technology

**ODE** Ordinary Differential Equitation

**FD/FE** Finite Difference / Finite Element

**FELA** Finite Element limit analysis

**SSE** Error sum of squares

**RMSE** Root mean square error

Appendix B

# Introduction to OptumG2

## B.1 Introduction

OptumG2 is a finite element program for geotechnical boundary value problems. The program has some features very similar to widely available programs, but it has some unique features as well. It can run traditional incremental elastoplastic analysis, seepage, and consolidation. Moreover, it is capable of computing limit load, upper bound, and lower bound to the limit load, without having to run an incremental elastoplastic loading. This method, known as numerical limit analysis, is executed by increasing external load(s) or reducing material strength (c-$\varphi$ analysis) up until failure point. The limit analysis is the unique feature of this program which separates the program from other programs.

### B.1.1 Starting interface

OptumG2 has a user-friendly interface. A full-screen view of the program upon start can be seen in Figure B.1. The different components of the program are named in the figure.

Program has following ribbons:

- Geometry
- Materials
- Features
- Results

These ribbons are shown in the Figure B.2, Figure B.3, Figure B.4 and Figure B.5, respectively.

Concisely, the geometry of the problem in hand is going to be drawn in *Geometry* ribbon, then in *Material* ribbon, the desired material model will be assigned to the drawn geometries.

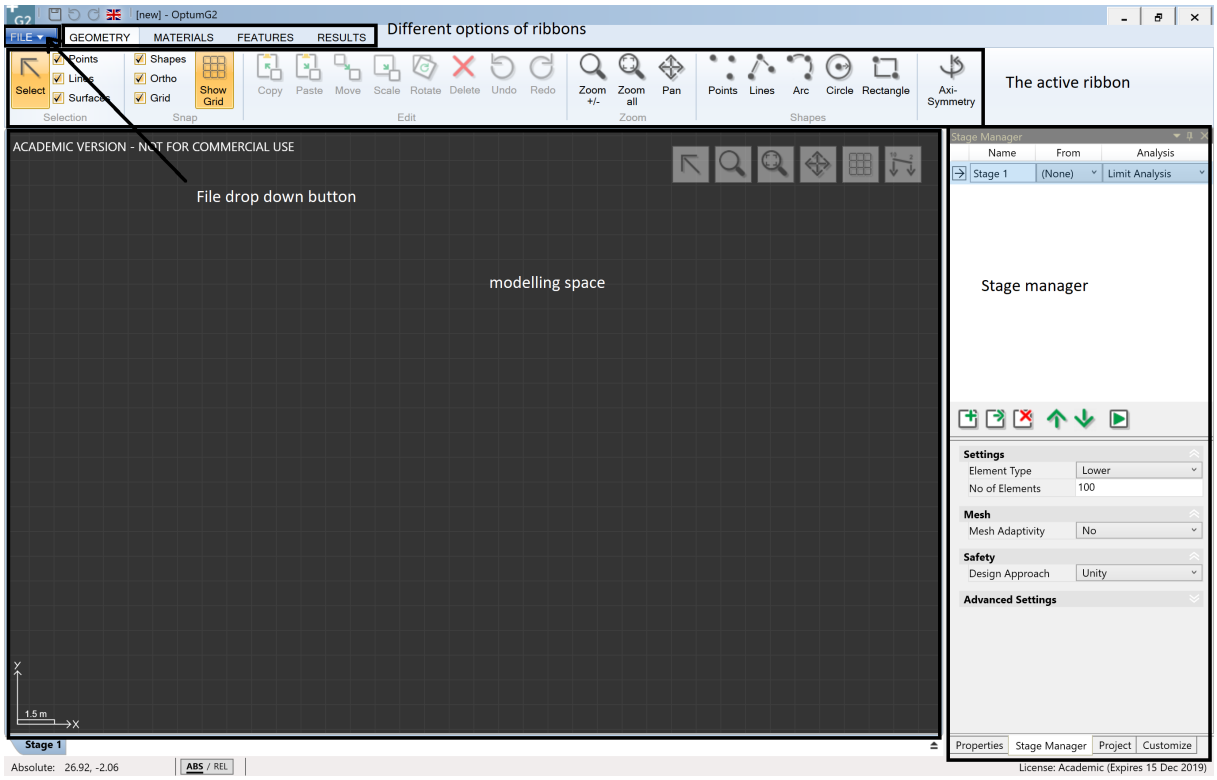


Figure B.1: A full screen view of OptumG2 graphic interface

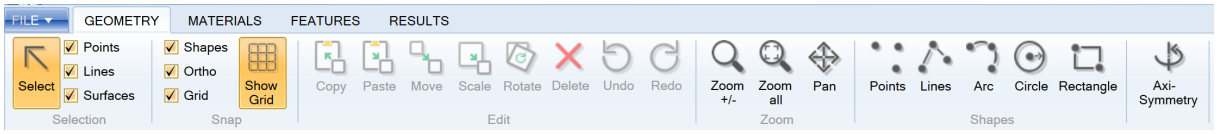


Figure B.2: Geometry ribbon in OptumG2

In the *Features* ribbon, features such as load, plate, and alike can be assigned to the drawn geometry and the *Results* ribbon shows the results of the calculation. In the stage manager, it is possible to create and manage the different stages of the simulation.

In the following subsection, each of these ribbons and what they do will be explained.

## B.1.2 Geometry

In this ribbon, one can start drawing the desired geometry of a boundary value problem. Following options are available for drawing the desired geometry:

- Points
- Lines
- Arc
- Circle
- Rectangle

There is also the option of importing *DXF* for drawing the geometry. It is also possible to import a picture with a specifying height and width for drawing geometry from that. The

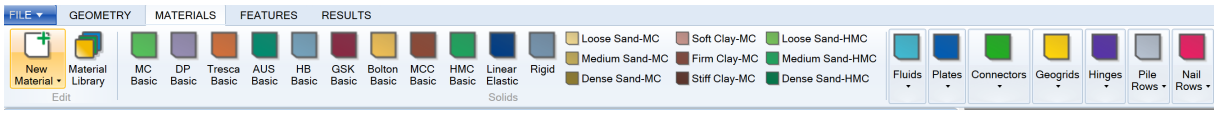


Figure B.3: Material ribbon in OptumG2

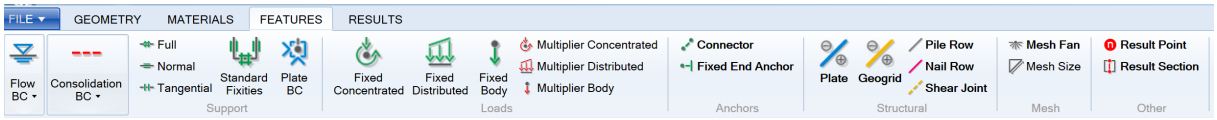


Figure B.4: Features ribbon in OptumG2

program can do both plane strain analysis and axisymmetry analysis and this can be specified in this ribbon.

### B.1.3 Features

Loads, boundary condition and structural elements are placed in "Features" ribbon. Each of these can be applied to any line (or point) upon clicking on the line and clicking on the desired item. In the "Features" ribbon, following features can be seen:

- Flow BC
- Consolidation BC
- Support
- Loads
- Anchors
- Structural
- Mesh
- Other

Features such as support, loads, and others which are relevant here will be explained.

#### B.1.3.1 Support

This category contains the following features:

- Full: This option constrains displacement in all directions along the selected line.
- Normal: Displacement normal to the selected line is assigned to zero.
- Tangential: Displacements along the line is set to zero.
- Standard fixities: This option applies "Normal support" to all vertical lines and "Full support" to horizontal lines.
- Plate BC: This feature assigns vertical, horizontal, and moment fixities to a given point. Displacement can be either fixed, free, or have a given value.

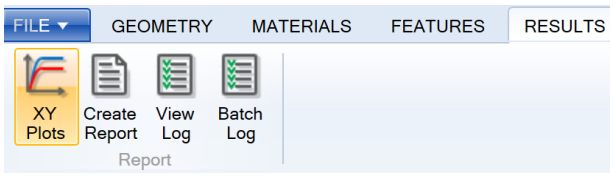


Figure B.5: Results ribbon in OptumG2

Line support (Normal, Tangential, Full) functions also as an impermeable boundary. It is recommended to use *Standard fixities* for usual boundary value problems, such as the one used in this study.

### B.1.3.2 Loads

OptumG2 has six different features which can be categorized into two categories: Fixed loads (shown in green) and Multiplier loads (shown in red). Multiplier loads have significance in the Limit Analysis where they are magnified to reach a limit load. The Fixed load exerts a fixed load in all types of analyses. Three types of load within each of these two categories are as follows:

- Concentrated load ($kN/m$): This a point load that can be applied only to plated and geogrids.
- distributed load ($kN/m^2$): these are line loads that can be applied to any line.
- Body load ($kN/m^3$ or $\times g$): This type of load can be applied to solids and plates. It can be given as a force (in $kN/m^3$) or a fraction of the unit weight (a multiplication of $\times g$) of the solid which is applying to.

Figure B.6 is showing these three different loading types. These loads can be given magnitude and direction. It is possible to use the local coordinate system or one can decide to use the global coordinate system.

Apart from magnitude and direction, “Load Type” and “Load Category” is assigned to all loads. By assigning different “Design Approaches” to the running stage, different partial factors can be assigned to material parameters and loads in Limit Analysis and Strength Reduction analyses. These partial factors are predefined for each *design approach*. They can be assigned through Project/Design Approach. The window of Design Approach can be seen in Figure B.7.

By using the user-defined option of “User X”, one can implement, for example, the Norwegian standard (seen in Table B.1).

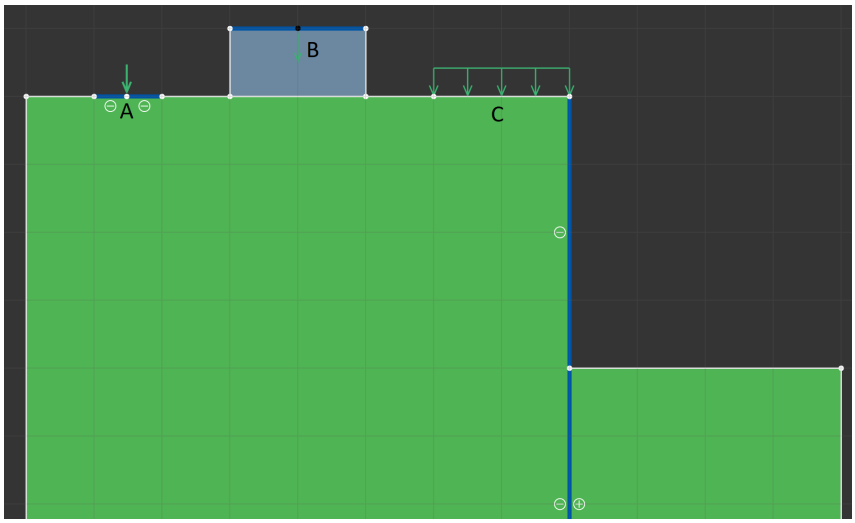


Figure B.6: Different load types: Concentrated load (A), Body load (B), Distributed load (C).

Table B.1: Partial factor used in design approaches common in Norway

| Parameter | | symbol | Factors | |
|---|---|---|---|---|
| | | | method 2 | method 3 |
| Permanent Action (G) | Unfavorable | $\gamma_G$ | 1,35 | 1,35/1,0 [1] |
| | Favorable | $\gamma_{G,fav}$ | 1,0 | 1,0 |
| Variable Action (Q) | Unfavorable | $\gamma_Q$ | 1,5 | 1,5/1,3 |
| | Favorable | - | - | - |
| Shearing Resistance ($tan\phi$) | | $\gamma_\phi$ | 1,0 | 1,25 |
| Effective cohesion (c') | | $\gamma_{c'}$ | 1,0 | 1,25 |
| Undrained Shear Strength ($S_u$) | | $\gamma_{S_u}$ | 1,0 | 1,4 |
| Weigth Density | | $\gamma_\gamma$ | 1,0 | 1,0 |
| Resistance Factor | | $\gamma_R$ | varies [2] | 1,0 |

[1] Note that in method 3, the first factor is applied to structural loads and second one to geotechnical loads.
[2] This factor varies based on the installation method and loading. See Table NA.A.6 to NA.A.8 in the National Annex of Eurocode 7: Geotechnical Design, NS-EN 1997-1+A1:2013+NA:2016.

#### B.1.3.3 Structural

This category has the following features:

- Plates: These are beam elements which are used to model thin structural elements such as sheet piles. Possible material sets available will be presented later.
- Geogrid: This type of truss elements are used to model geogrids and grouted anchors. Possible material sets for modeling av geogrids will be presented later.
- Pile Row: Special elements for accounting for three-dimensionality of the problem.
- Nail Row: This is a similar feature to the Pile Row, but instead of the pile, the nails are defined.

Design Approaches

| | Unity | DA1/1 | DA1/2 | User 1 | User 2 | User 3 | User 4 |
|---|---|---|---|---|---|---|---|
| **Unit Weight - Unfavourable:** | | | | | | | |
| Permanent | 1 | 1.35 | 1 | 1 | 1 | 1 | 1 |
| **Unit Weight - Favourable:** | | | | | | | |
| Permanent | 1 | 1 | 1 | 1 | 1 | 1 | 1 |
| **Loads - Unfavourable:** | | | | | | | |
| Permanent | 1 | 1.35 | 1 | 1 | 1 | 1 | 1 |
| Variable | 1 | 1.5 | 1.3 | 1 | 1 | 1 | 1 |
| Accidental | 1 | 1 | 1 | 1 | 1 | 1 | 1 |
| **Loads - Favourable:** | | | | | | | |
| Permanent | 1 | 1 | 1 | 1 | 1 | 1 | 1 |
| Variable | 1 | 0 | 0 | 1 | 1 | 1 | 1 |
| Accidental | 1 | 0 | 0 | 1 | 1 | 1 | 1 |
| **Materials:** | | | | | | | |
| c | 1 | 1 | 1.25 | 1 | 1 | 1 | 1 |
| $\phi$ | 1 | 1 | 1.25 | 1 | 1 | 1 | 1 |
| $s_u$ (Tresca) | 1 | 1 | 1.4 | 1 | 1 | 1 | 1 |

OK Cancel

Figure B.7: Design approaches and the their partial factors.

- Shear Joint: These are interface elements to model internal discontinuities in the soil or interface between two solid domain. Soil Models can be assigned to them.

#### B.1.3.4 Mesh

The mesh category contains two features:

- Mesh Fan: These features can be applied to points that creates a fan of elements around the point (as seen in Figure B.8).
- Mesh Size: This feature can be applied to any type of geometry where mesh size can be specified beforehand.

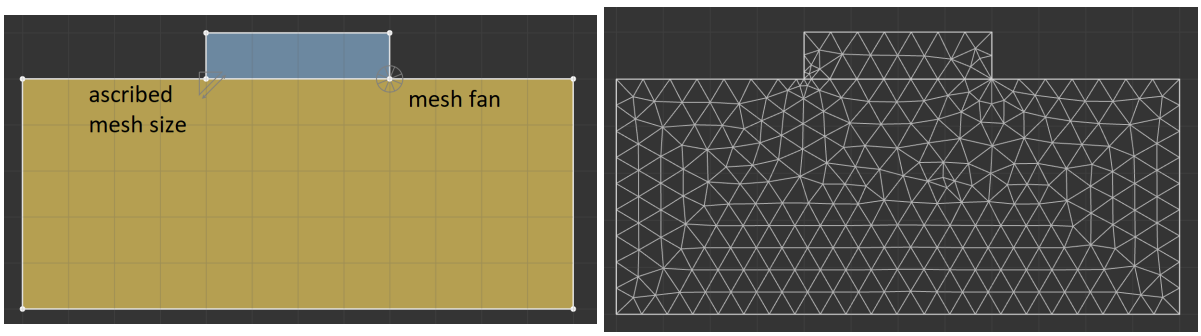


(a) Mesh fan and mesh size feature

(b) Resulting meshing

Figure B.8: Applying mesh size and mesh fan to a direct footing

#### B.1.3.5 Other

This category contains two features:

- Result Point: This feature logs the results in a given point for plotting purposes later.
- Result Section: This feature acts like a virtual plate where the sectional forces on this plate are calculated and can be plotted.

### B.1.4 Stage Manager

In this window, it is possible to manage and run the different stages of analysis (see Figure B.9). The upper part of the window shows different stages and what kind of ascribed analyses to them. The lower half of the window contains the setting of the selected stage. In between these two, control buttons are located which one can add, remove, move, and run the selected analysis.

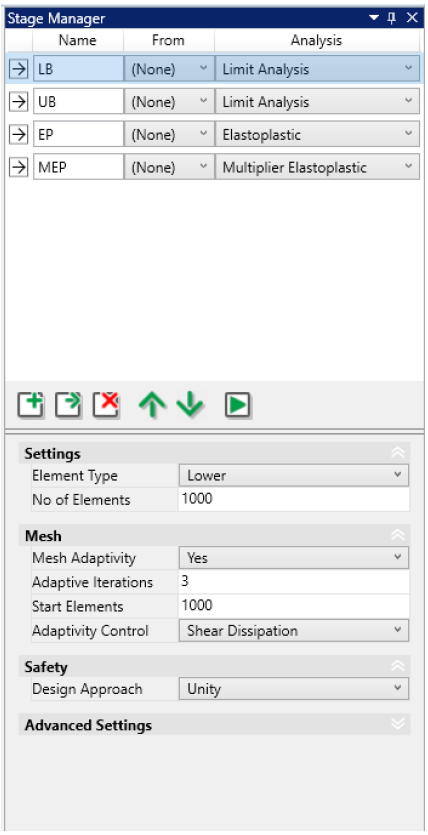


Figure B.9: A view of the stage manager window

Here, one can create different analysis types for different stages. The available analyses are:

- Mesh: a meshing of the boundary value problem would be generated.
- Seepage: a seepage analysis with the assigned seepage boundaries would be performed.

- Initial stress: this step tries to satisfy equilibrium, boundary condition, and yield condition by distributing the stresses in the soil mass. Fixed loads are processed, but not multiplier loads.
- Elastic: yield condition or any form of restriction on stress development is ignored. Fixed loads are processed, but not multiplier loads.
- Limit Analysis: it is a rapid check of stability of the boundary value problem without having to run a step by step load-deformation analysis. Multiplier loads get a factor until the structure goes to failure.
- Strength reduction: By reducing soil parameters, this type of analysis finds the strength necessary to find the have failure with given load(s).
- Elastoplastic: This one is like an elastoplastic analysis of common FE programs.
- Multiplier elastoplastic: This one is a combination of limit analysis and elastoplastic analysis. Here, the maximum multiplier found by running incremental loading.
- Consolidation: Consolidation analysis similar to common FE programs.

In the "setting" window, it is possible to assign element type and the number of elements desired elements. It is possible to use "mesh adaptivity" as well. The mathematical foundation of this feature is explained in Lyamin et al. [2005], but in essence, this feature tries to increase mesh refinement by a control mechanism, shear dissipation, for example. Figure 5.5 shows an example of how this mechanics works.

## B.2 Material Models

The materials available in Optum G2 can be assigned to six different categories of elements:

- Solids: Solid materials such as soil, rock and concrete and interfaces between materials
- Fluids: for modeling of fluids
- plates: for modeling of steel structures
- : Geogrids: for modeling of geogrids
- Connectors: for modeling of fixed-end anchors and plate to plate connectors
- Hinges: for modeling of hinges

A full description of the models and how they behave and the parameter used in each model is described in detail in Krabbenhøft et al. [2016c]. In this work, solids are used more often and will be discussed. Following materials are available in Optum G2 for solids:

- Rigid
- Linear Elastic
- Mohr-Coulomb
- Drucker-Prager
- Tresca
- Anisotropic Undrained Shear (AUS)
- Hoek-Brown
- GSK
- Bolton
- Modified Cam Clay
- Hardening Mohr-Coulomb

In this work, rigid, linear elastic, Mohr-Coulomb, and Tresca model were used more often. A description and the relevant features of these models will be discussed and presented in the following subsections.

### B.2.1 General Model

Every material can be assigned three type of drainage modes, namely:

- Drained
- Drained/undrained
- Non-porous

By choosing “Drained/undrained” type and choosing “short term” analysis in stage manager, it is possible to run undrained analysis.

### B.2.2 Rigid

This type of material describes a perfectly rigid material without any limitation on strength.

### B.2.3 Linear elastic

Linear elastic materials follow Hooke’s law, which defines an indefinitely strong material with a linear relationship between the strain and the effective stress. In the program, it is possible to use two sets of parameters for deformation modulus:

- Set A:
- Young’s modulus, E [MPa]
- Poisson’s ratio []
- Set B:
- Bulk modulus, K [MPa]
- Shear modulus,G [MPa]

### B.2.4 Mohr-Coulomb

Mohr-Coulomb model used in the program follows the conventional MC model, such a described in Nordal [2016]. The model follows an elastic deformation model and yield function defined by friction angle and cohesion. The model supports the non-associated flow rule as well.

#### B.2.4.1 Stiffness

Stiffness parameters which can be used in MC model can be categorised into:

- Linear isotropic elasticity
- Linear anisotropic elasticity
- Nonlinear isotropic elasticity

The linear options are the same as described in Subsection B.2.3. The nonlinear option can act like the hardening model and is a confining pressure-dependent elastic modulus.

#### B.2.4.2 Yield function

Yield function for the Mohr-Coulomb is defined as:

$$F = (\sigma'_1 + a) - N \cdot (\sigma'_3 + a) \tag{B.1}$$

where the inclination, N, is equal to:

$$N = \frac{1 + sin\varphi}{1 - sin\varphi} \tag{B.2}$$

where attraction, a, is equal to $a = \frac{c}{tan\varphi}$.

#### B.2.4.3 Flow Rule

There is two options available for flow rule:

- Associated
- Non-associated

For associated flow, yield function is also the flow potential. The flow potential for non-

associated option is defined as:

$$G = (\sigma'_1 + a) - N_f \cdot (\sigma'_3 + a) \tag{B.3}$$

where the inclination, $N_f$, is equal to:

$$N_f = \frac{1 + sin\psi}{1 - sin\psi} \tag{B.4}$$

Flow rule is defined by the dilation angle, $\psi$. Besides, there is possible to set volumetric and shear dilation caps such that the dilation angle becomes zero after a predefined strain (more details in Krabbenhøft et al. [2016c]).

## B.2.5 Tresca

The Tresca model is one of the simple and known models used in geotechnical engineering. The model utilized in the Optum G2 follows the basic theoretical principles of, as mention, for example, in Grande et al. [2016].

### B.2.5.1 Stiffness

The model operates with a set of simple undrained elastic parameters, namely $E_u$ or $G$.

### B.2.5.2 Yield function

Yield function for Tresca model is defined as:

$$F = |\sigma_1 - \sigma_3| - 2 \cdot S_u \tag{B.5}$$

Appendix C

# Matlab Codes

A Matlab code used for running the OptumG2 automatically and changing desired soil parameter. The code assigns a numeric value to a parameter, and runs the OptumG2 and fetches the result of the simulation. The code is as follow:

```
%OptmG2 via Matlab
inputfile = 'Vertical.g2x'; %your file
runfile = [inputfile(1:length(inputfile)-8) 'RUN.g2x'];
runcommand = ['optumg2cmd ' runfile ' /log:logfile.m/echo'];

var(1) = 'aaa'; %your first variable
varr(1) = 'bbb'; %your second variable

%friction angle changing from 15 to 45
phi =15:0.5:45;
tan_phi=tand(phi);

% for roughness ratio, r, find the appropriate tau_h/Sigma'_v:
r=0.2;
tS=(r*tan_phi);

for i = 1:length(phi)
oldstr = var(1);
    oldstr2 = varr(1);
    newstr = tS(i);
    newstr2= phi(i);
    oldfile = inputfile;
    newfile = runfile;
    newfile2 = runfile;
    replacestr(oldstr,newstr,oldfile,newfile);
    replacestr(oldstr2,newstr2,newfile,newfile2);
    dos(runcommand);
    res = resread('COLLAPSE MULTIPLIER = ','logfile.m');
    UB(i) = res;
end;
```

Replacing function is as follow:

```
%function replacestr(oldstr,newstr,file,newfile)

function replacestr(oldstr,newstr,oldfile,newfile)

if isstr(newstr) == 0
    newstr = num2str(newstr);
end;
A = fileread(oldfile);
I = strfind(A,oldstr);

for i = 1:length(I)
    I = strfind(A,oldstr);
    Ib = I(1);
    Ie = Ib+length(oldstr);
    B = [A(1:Ib-1) newstr A(Ie:length(A))];
    A = B;
end;

fid = fopen(newfile,'w');
fwrite(fid,A);
fclose(fid);
```

Reading function is as follow:

```
%function R = resread(str,file)

function R = resread(str,file)
R = [];

A = fileread(file);
I = strfind(A,str);

a = '';
for i = 1:length(I)
    for j = 1:100
        a(j) = A(I(i)+length(str)+j-1);
        if length(str2num(a(j)))==0 & a(j)~='.' & a(j)~='-'
        if a(j)~='+' & a(j)~='E' & a(j)~='e' %& a(j)~=' '
            R(i,1) = str2num(a(1:j-1));
            a = '';
            break
            end;
        end;
    end;
end;
```

Another Matlab code was used for running the OptumG3 graphical interface automatically. The code assigns a numeric value to a parameter, either in the soil body or in the geometry, and runs the OptumG3 and fetches the result of the simulation. The code is as follow:

```
%OptmG3 via Matlab %

%inclined loads
tetta=0:1:20;
h=sind(tetta);
v=cosd(tetta);

for int=1:length(v)

% calling OptumG3
OptumG3;
import OptumG3.NetRemoteClient.Remote.*
G3 = G3Client();
G3.Reset();

%add domain
s1 = G3.CreateBox(G3.Axis(-3, 1, 0, 0, 0, 1), 7, 3, 5);
s2 = G3.CreateBox(G3.Axis(-1.5, 0, 0, 0, 0, 1), 4, 1, 5);
s3 = G3.CreateBox(G3.Axis(2.5, 0, 0, 0, 0, 1), 1.5, 1, 5);
s4 = G3.CreateBox(G3.Axis(-3, 0, 0, 0, 0, 1), 1.5, 1, 5);
s5 = G3.CreateBox(G3.Axis(-3, -3, 0, 0, 0, 1), 7, 3, 5);
%partitioning
G3.Partition(G3.NewShapeCollection().Added(s1).Added(s2).Added(s3).Added(s4
    ).Added(s5));

%create material
%Shell material - rigid
shellmat = G3.CreateMaterial(MaterialCategory.Shells,'RigidShell');
%set properties
ps = G3.NewPropertyCollection()...
    .Added('Type', 'Shell')...
    .Added('ContinuumModel',ContinuumModel.Rigid)...
    .Added('Color', G3.Color(0, 0, 250));
G3.SetMaterialProperties(shellmat, ps)

%create material
%undrained clay
solidmat1 = G3.CreateMaterial(MaterialCategory.Solids,'Clay');
%set properties
ps = G3.NewPropertyCollection()...
    .Added('Type', 'Tresca')...
    .Added('cu', G3.MakeValueParameter(100))...
    .Added('Color', G3.Color(250, 100, 0));
G3.SetMaterialProperties(solidmat1, ps)


%adding material to the shell element
```

```
selection = G3.Selection(G3.BoundBox(0.5,0.5,4,0.1,0.1,2), ShapeKind.Face);
features = G3.NewFeatureCollection();

for i = 0:selection.Count()-1
    features.Add(G3.MakeShell(selection.At(i), shellmat));
end

G3.CreateFeatures(features);
%reset feature container

% adding material to the soil body
selection = G3.Selection(G3.BoundBox(-4,-4,0,8,8,5), ShapeKind.Solid);
features = G3.NewFeatureCollection();

%add material to feature container
for i=0:selection.Count-1
    features.Add(G3.MakeSolid(selection.At(i), solidmat1));
end

G3.CreateFeatures(features);
features = G3.NewFeatureCollection();


% creating the inclined load
selection = G3.Selection(G3.BoundBox(0.5,0.5,5,-0.1,-0.1,-1), ShapeKind.
    Face);
load = G3.MakeLoad(selection.At(0), LoadOption.Multiplier, 0, h(int), -v(
    int));
G3.CreateFeature(load);

% Stage settings
ps = G3.NewPropertyCollection()...
    .Added('AnalysisType', AnalysisType.LimitAnalysis)...
    .Added('FEType', FEType.Mixed)...
    .Added('Name', 'LA01')...
    .Added('TargetElements',25000)...
    .Added('StartElements',10000)...
    .Added('UseAdaptivity',YesNo.Yes)...
    .Added('AdaptivitySteps',3);
G3.SetStageProperties(ps);

% standard fixities
G3.CreateStandardFixities();

file = 'C:\Users\HR\Documents\optumG3\without-results.g3x';

% saving
G3.SaveProject(file);

% Run analysis
result = G3.RunAnalysis();
```

```
96
97  file = 'C:\Users\HR\Documents\personal\optmG3\with-results.g3x';
98
99  %saving
100 G3.SaveProject(file);
101
102
103 % Print result
104 for i=0:result.StageResults.Count-1
105     it = result.StageResults.At(i);
106     disp(['Stage: ', char(it.Stage.Name),', Status: ', char(it.
    AnalysisStatus)])
107     for j=0:it.CriticalValue.Count-1
108         it_j = it.CriticalValue.At(j);
109         disp([char(it_j.Name),': ',num2str(it_j.Value), ' ', char(it_j.
    Units)]);
110     end
111 end
112
113 it_j.Value
114 LA(int) =ans;
115
116  end
117
118 LA=LA';
```

# Bibliography


R. Aabøe, T.E. Frydenlund, F. Oset, and J. Vaslestad. *Geotechnics in road construction (in Norwegian: Geoteknikk i vegbygging)*. Statens vegvesen, Vegdirektoratet, 2018 edition edition, 2018.

Saad Ali Aiban and Dobroslav Znidarčić. Centrifugal modeling of bearing capacity of shallow foundations on sands. *Journal of Geotechnical Engineering*, 121(10):704–712, 1995. doi: doi:10.1061/(ASCE)0733-9410(1995)121:10(704). URL https://doi.org/10.1061/(ASCE)0733-9410(1995)121:10(704).

J. Ameratunga, N. Sivakugan, and B.M. Das. *Correlations of Soil and Rock Properties in Geotechnical Engineering*. Springer India, 2015. ISBN 9788132226291. URL https://books.google.no/books?id=DrYvCwAAQBAJ.

A. Cavallaro, Maugeri M., and Mazzarella R. Static and dynamic properties of leighton buzzard sand from laboratory tests. In *Proceedings of the 4th International Conference on Recent Advances in Geotechnical Earthquake Engineering and Soil Dynamics*, 2001.

D.P. Coduto. *Foundation Design: Principles and Practices*. Prentice Hall, 2001. ISBN 9780135897065. URL https://books.google.no/books?id=z91RAAAAMAAJ.

A. D. Cox, G. Eason, and H. G. Hopkins. Axially symmetric plastic deformations in soils. *Philosophical Transactions of the Royal Society of London. Series A, Mathematical and Physical Sciences*, 254(1036):1–45, 1961. doi: 10.1098/rsta.1961.0011. URL https://doi.org/10.1098/rsta.1961.0011.

B.M. Das. *Shallow Foundations: Bearing Capacity and Settlement, Third Edition*. CRC Press, 2017. ISBN 9781351672443. URL https://books.google.no/books?id=H9sNDgAAQBAJ.

E. H. Davis. *Theories of plasticity and the failure of soil masses*, page 341–380. Butterworths, Butterworth, London, 1968.

E. H. Davis and J. R. Booker. The effect of increasing strength with depth on the bearing capacity of clays. *Géotechnique*, 23(4):551–563, 1973. doi: 10.1680/geot.1973.

23.4.551. URL https://www.icevirtuallibrary.com/doi/abs/10.1680/geot.1973.23.4.551.

E.H. Davis and J.R. Booker. The bearing capacity of strip footings from the standpoint of plasticity theory. *Proceedings of the first Australian–New Zealand Conference on Geomechanics*, pages 275–282, 1971.

E. E. de Beer. Experimental determination of the shape factors and the bearing capacity factors of sand. *Géotechnique*, 20(4):387–411, 1970. doi: 10.1680/geot.1970.20.4.387. URL https://www.icevirtuallibrary.com/doi/abs/10.1680/geot.1970.20.4.387.

D. C. Drucker and W. Prager. Soil mechanics and plastic analysis or limit design. *Quarterly of Applied Mathematics*, 10(2):157–165, 1952. ISSN 0033569X, 15524485. URL http://www.jstor.org/stable/43633942.

S. Frydman and H.J. Burd. Numerical studies of bearing-capacity factor $N_\gamma$. *Journal of Geotechnical and Geoenvironmental Engineering*, 123(1):20–29, 1997. doi: doi:10.1061/(ASCE)1090-0241(1997)123:1(20).

Majid Ghayoomi, Ganna Suprunenko, and Morteza Mirshekari. Cyclic triaxial test to measure strain-dependent shear modulus of unsaturated sand. *International Journal of Geomechanics*, 17, 2017. doi: 10.1061/(ASCE)GM.1943-5622.0000917.

H. Q. Golder, W. Fellenius, F. Kogler, H. Meischeider, H. Krey, and L. Prandtl. The ultimate bearing pressure of rectangular footing. *Journal of the Institution of Civil Engineers*, 17(2):161–174, 1941. doi: 10.1680/ijoti.1941.13728. URL https://www.icevirtuallibrary.com/doi/abs/10.1680/ijoti.1941.13728.

S. Gourvenec and S. Barnett. Undrained failure envelope for skirted foundations under general loading. *Géotechnique*, 61(3):263–270, March 2011. URL https://eprints.soton.ac.uk/414646/.

S. Gourvenec and M. Randolph. Effect of strength non-homogeneity on the shape of failure envelopes for combined loading of strip and circular foundations on clay. *Géotechnique*, 53(6):575–586, 2003. doi: 10.1680/geot.2003.53.6.575. URL https://www.icevirtuallibrary.com/doi/abs/10.1680/geot.2003.53.6.575.

S. Gourvenec, M. Randolph, and O. Kingsnorth. Undrained bearing capacity of square and rectangular footings. *International Journal of Geomechanics*, 6(3):147–157, 2006. doi: doi:10.1061/(ASCE)1532-3641(2006)6:3(147).

L. Grande, A. Emdal, and S. Nordal. *Theoretical Soil Mechanics [Class Handout]*. Geotechnical Division of Norwegian University of Science and Technology, Trondheim, 2016.

A. M. Hanna and G. G. Meyerhof. Experimental evaluation of bearing capacity of footings subjected to inclined loads. *Canadian Geotechnical Journal*, 18(4):599–603, 1981. ISSN 0008-3674. doi: 10.1139/t81-072. URL https://doi.org/10.1139/t81-072.

J.B. Hansen. *A General Formula for Bearing Capacity*. Danish geotechnical Institute, 1961. URL https://books.google.no/books?id=0P3WHAAACAAJ.

J.B. Hansen. *A Revised and Extended Formula for Bearing Capacity*. Danish Geotechnical Institute, 1970. ISBN 9788774510284. URL https://books.google.no/books?id=_ejcswEACAAJ.

M. Hjiaj, A. V. Lyamin, and S. W. Sloan. Numerical limit analysis solutions for the bearing capacity factor $n_\gamma$. *International Journal of Solids and Structures*, 42(5):1681–1704, 2005. ISSN 0020-7683. doi: https://doi.org/10.1016/j.ijsolstr.2004.08.002. URL http://www.sciencedirect.com/science/article/pii/S0020768304004500.

A.B Huang and H.S. Yu. *Foundation Engineering Analysis and Design*. CRC Press, Boca Raton, 1st edition edition, 2017. ISBN 9781138720794. doi: https://doi.org/10.1201/9781351255400.

N. Janbu. *Behaviour of off-shore structures : proceedings of the first international conference : BOSS'76 : 2*, volume 2. Norwegian Institute of Technology, Trondheim, Norway, 1976.

K. Krabbenhøft. FASD: Friction angle stress state dependent model for sand. Webinar, 2020.

K. Krabbenhøft and L. Damkilde. A general non-linear optimization algorithm for lower bound limit analysis. *International Journal for Numerical Methods in Engineering*, 56(2):165–184, 2003. ISSN 0029-5981. doi: 10.1002/nme.551. URL https://onlinelibrary.wiley.com/doi/abs/10.1002/nme.551.

K. Krabbenhøft, A. V. Lymain, and J. Krabbenhøft. *OptumG2: Examples*. Optum Computational Engineering, Optum Computational Engineering 2016, 2016a.

K. Krabbenhøft, A. V. Lymain, and J. Krabbenhøft. *OptumG2: Features*. Optum Computational Engineering 2016, 2016b.

K. Krabbenhøft, A. V. Lymain, and J. Krabbenhøft. *OptumG2: Materials*. Optum Computational Engineering 2016, 2016c.

K. Krabbenhøft, A. V. Lymain, and J. Krabbenhøft. *OptumG2: Theory*. Optum Computational Engineering, 2016d.

F. H. Kulhawy and Paul Mayne. Manual on estimating soil properties for foundation design. 1990.

A. S. Kumbhojkar. Numerical evaluation of terzaghi's $n_\gamma$. *Journal of Geotechnical Engineering*, 119(3):598–607, 1993. doi: doi:10.1061/(ASCE)0733-9410(1993)119:3(598).

P. Lade and J. Duncan. Cubical triaxial tests on cohesionless soil. *ASCE J Soil Mech Found Div*, 99:793–781, 1973. doi: 10.1016/0148-9062(74)91579-4.

P. Lade and H. Musante. Three-dimensional behaviour of remolded clay. *ASCE J Geotech Eng Div*, 104:193–209, 1978.

P.V. Lade. *Triaxial Testing of Soils*. Wiley, 2016. ISBN 9781119106623. URL https://books.google.no/books?id=ru77rQEACAAJ.

D. Leshchinsky and G.F. Marcozzi. Bearing capacity of shallow foundations: Rigid versus flexible models. *Journal of Geotechnical Engineering*, 116(11):1750–1756, 1990. doi: doi: 10.1061/(ASCE)0733-9410(1990)116:11(1750). URL https://doi.org/10.1061/(ASCE)0733-9410(1990)116:11(1750).

D. Loukidis and R. Salgado. Bearing capacity of strip and circular footings in sand using finite elements. *Computers and Geotechnics*, 36(5):871–879, 2009. ISSN 0266-352X. doi: https://doi.org/10.1016/j.compgeo.2009.01.012. URL http://www.sciencedirect.com/science/article/pii/S0266352X09000135.

A. V. Lyamin and S. W. Sloan. Lower bound limit analysis using non-linear programming. *International Journal for Numerical Methods in Engineering*, 55(5):573–611, 2002a. ISSN 0029-5981. doi: 10.1002/nme.511. URL https://onlinelibrary.wiley.com/doi/abs/10.1002/nme.511.

A. V. Lyamin and S. W. Sloan. Upper bound limit analysis using linear finite elements and non-linear programming. *International Journal for Numerical and Analytical Methods in Geomechanics*, 26(2):181–216, 2002b. ISSN 0363-9061. doi: 10.1002/nag.198. URL https://onlinelibrary.wiley.com/doi/abs/10.1002/nag.198.

A.V. Lyamin, S. W. Sloan, K. Krabbenhøft, and M. Hjiaj. Lower bound limit analysis with adaptive remeshing. *International Journal for Numerical Methods in Engineering*, 63(14):1961–1974, 2005. ISSN 0029-5981. doi: 10.1002/nme.1352. URL https://onlinelibrary.wiley.com/doi/abs/10.1002/nme.1352.

N. Manoharan and S. P. Dasgupta. Bearing capacity of surface footings by finite elements. *Computers & Structures*, 54(4):563–586, 1995. ISSN 0045-7949. doi: https://doi.org/10.1016/0045-7949(94)00381-C. URL http://www.sciencedirect.com/science/article/pii/004579499400381C.

C.M. Martin. *User guide for ABC: Analysis of Bearing Capacity. Version 1.0*. Department of Engineering Science of University of Oxford, 2004.

C.M. Martin. Exact bearing capacity calculations using the method of characteristics. *Proc. 11th Int. Conf. of IACMAG Turin*, 4, 2005.

G. G. Meyerhof. The ultimate bearing capacity of foudations. *Géotechnique*, 2(4):301–332, 1951. doi: 10.1680/geot.1951.2.4.301. URL https://www.icevirtuallibrary.com/doi/abs/10.1680/geot.1951.2.4.301.

G.G. Meyerhof. Some recent research on the bearing capacity of foundations. *Canadian Geotechnical Journal*, 1(1):16–26, 1963. ISSN 0008-3674. doi: 10.1139/t63-003. URL https://doi.org/10.1139/t63-003.

R. Michalowski. An estimate of the influence of soil weight on bearing capacity using limit analysis. *SOILS AND FOUNDATIONS*, 37(4):57–64, 1997. doi: 10.3208/sandf.37.4_57.

S. Nordal. *Geotechnical Engieering, Advanced Course [Class Handout]*. Geotechnical division, NTNU, 2016.

Norsk Standard. *Eurocode 7: Geotechnical design - Part 1: General rules*. Norsk Standard, 2016. ISBN NS-EN 1997-1:2004+A1:2013+NA:2016.

L. Prandtl. Hauptaufsätze: Über die eindringungsfestigkeit (härte) plastischer baustoffe und die festigkeit von schneiden. *ZAMM - Journal of Applied Mathematics and Mechanics / Zeitschrift für Angewandte Mathematik und Mechanik*, 1(1):15–20, 1921. ISSN 0044-2267. doi: 10.1002/zamm.19210010102. URL https://onlinelibrary.wiley.com/doi/abs/10.1002/zamm.19210010102.

M. Randolph and S. Gourvenec. *Offshore Geotechnical Engineering*. Taylor & Francis, 2011. ISBN 9781134022168. URL https://books.google.no/books?id=yAlEff_zspUC.

N.S.V.K. Rao. *Foundation Design: Theory and Practice*. Wiley, 2010. ISBN 9780470828151. URL https://books.google.no/books?id=IraFwRN4dbYC.

H. Reissner. Zum erddruckproblem. In *First International Conference on Applied Mechanics Proceedings,*, pages 295–311, 1924.

K. Terzaghi, R.B. Peck, and G. Mesri. *Soil Mechanics in Engineering Practice*. Wiley, 1996. ISBN 9780471086581. URL https://books.google.no/books?id=bAwVvO71FXoC.

J. Ticof. *Surface Footings on Sand Under General Planar Loads*. Thesis, University of Southampton, 1978. URL https://ethos.bl.uk/OrderDetails.do?uin=uk.bl.ethos.475212.

A.S. Vesić. Analysis of ultimate loads of shallow foundations. *Journal of the Soil Mechanics and Foundations Division*, 99(1):45–73, 1973.

H. Yamaguchi, T. Kimura, and N. Fuji-I. On the influence of progressive failure on the bearing capacity of shallow foundations in dense sand. *Soils and Foundations*, 16(4):11–22, 1976. ISSN 0038-0806. doi: https://doi.org/10.3208/sandf1972.16.4_11. URL http://www.sciencedirect.com/science/article/pii/S0038080620325713.